PNNL-37622

Automated Particle Analysis of Hanford Tank Wastes 241-AN-106, 241-AN-101, and 241-AW-105

April 2025

Edgar C. Buck, Austin A Bachman,
Jasmine Eshun, Reid A. Peterson

U.S. DEPARTMENT OF ENERGY

Prepared for the U.S. Department of Energy
under Contract DE-AC05-76RL01830

PACIFIC NORTHWEST NATIONAL LABORATORY
operated by
BATTELLE
for the
UNITED STATES DEPARTMENT OF ENERGY
under Contract DE-AC05-76RL01830

Printed in the United States of America

Available to DOE and DOE contractors from
the Office of Scientific and Technical Information,
P.O. Box 62, Oak Ridge, TN 37831-0062
www.osti.gov
ph: (865) 576-8401
fax: (865) 576-5728
email: reports@osti.gov

Available to the public from the National Technical Information Service
5301 Shawnee Rd., Alexandria, VA 22312
ph: (800) 553-NTIS (6847)
or (703) 605-6000
email: info@ntis.gov
Online ordering: http://www.ntis.gov

PNNL-37622
ITSW-RPT-001

Automated Particle Analysis of Hanford Tank Wastes 241-AN-106, 241-AN-101, and 241-AW-105

April 2025

Edgar C. Buck, Austin A Bachman,
Jasmine Eshun, Reid A. Peterson

Prepared for
the U.S. Department of Energy
under Contract DE-AC05-76RL01830

Pacific Northwest National Laboratory
Richland, Washington 99354

Abstract

This effort is involved in developing particle size and density distribution (PSDD) for the major phases within Hanford tank waste sludge. The object of this work has been to use automated particle analysis (APA) methods on the Scanning Electron Microscope (SEM) to provide PSDDs. The PSDD can be used to quantify the proportion of gibbsite particles likely to settle quickly and enable blending of wastes that may be prone to pipeline plugging such as the uranium phase, clarkeite with other wastes. The Hanford tank waste solids were analyzed with SEM combined with x-ray Energy Dispersive Spectroscopy (EDS) using APA. This method can allow thousands of individual particles to be characterized and so may provide a more representative view of the samples and inform on PSDDs.

We characterized several as-received sludge samples and developed PSDD with APA. Sample preparation methods were found to impact the collected results, as it was more difficult to collect representative samples of the larger particles. Much of the material was also dried and cemented together and that further impacted results.

Summary

This report, ITSW-RPT-001, supports Task One of the *Enabling High-Level Waste Sludge Delivery Through In-tank Processing in the Southeast (SE) Quadrant of the Hanford Tank Farms* project supported by the Department of Energy—Environmental Management (DOE-EM). This work followed Task Plan In-Tank Treatment Task 1- SEM (FY24), ITSW-TP-002.

The primary goal of this work is to accelerate the overall mission schedule by enabling the delivery of feed directly from the high-level waste tanks to the treatment plant. This may be accomplished by remediating slurry properties of the wastes in the SE quadrant. At present, significant challenges exist relative to the preparation and delivery of feed of sludge directly from waste tanks. Eliminating these challenges could remove the need for a stand-alone pretreatment facility.

The following samples from Hanford tank 241-AN-106, AW-105, and AN-101 were examined with Scanning Electron Microscopy (SEM) - Automated Particle Analysis (APA). The table below reports the mean particle diameters for the major high Z phases plus gibbsite in the tank waste segments.

Tank / Facility	Segment Identification	Gibbsite	Clarkeite	Fe/Bi-Rich
241-AN-106	14	4.22 ± 4.89 µm	3.15 ± 2.05 µm	2.68 ± 1.60 µm
241-AN-106	16 LH	4.30 ± 3.49 µm	--	2.58 ± 1.60 µm
241-AN-106	19 LH	--	3.39 ± 2.68 µm	3.74 ± 3.59 µm
241-AN-106	19 UH	--	0.83 ± 0.59 µm	1.55 ± 0.76 µm
241-AN-106	21 UH	6.17 ± 4.95 µm	2.72 ± 1.54 µm	2.76 ± 1.33 µm
241-AN-106	22 UH	4.73 ± 5.04 µm	2.52 ± 1.65 µm	2.41 ± 1.34 µm
Tank / Facility	**Segment Identification**	**Gibbsite**	**Clarkeite**	**Fe/Zr-oxide**
241-AN-101	14UH	3.67 ± 3.24 µm	2.70 ± 1.79 µm	3.03 ± 1.86 µm
241-AN-101	18LH	3.80 ± 2.46 µm	--	1.86 ± 1.78 µm
241-AN-101	19LH	4.45 ± 3.51 µm	2.56 ± 1.86 µm	2.46 ± 1.03 µm

Tank / Facility	Segment Identification	Gibbsite	Clarkeite	Zr-oxide
241-AW-105	8LH	--	2.88 ± 2.24 µm	3.08 ± 2.24 µm
241-AW-105	8UH	--	2.56 ± 1.52 µm	3.87 ± 3.45 µm

Some of the results from the SEM characterization of 241-AW-105 were also reported in Allred et al. (2025), Report No. DFTP-RPT-045.

Obtaining PSDDs with APA on the SEM provides relevant information that can be used to guide waste processing. The general conclusion from this work is that the fundamental particles of the major less-soluble phases, such as gibbsite and clarkeite, are below 5 µm in diameter. There was little evidence from this study of large heavy particles in these wastes. The largest particles were phosphates that will be dissolved during washing.

Acknowledgments

The authors thank the Radiochemical Processing Laboratory (RPL) Management and Radiological Control and particularly Kayla Samcoff for supporting the microscopy work on the tank waste samples within the Radiomaterials Microscopy Q-Suite. We also thank the staff at Building 222-S as well as the Shielded Analytical Laboratory (SAL) for extracting the tank waste samples. We thank Dr. Ming Zhu (DOE-EM) for supporting this work. Pacific Northwest National Laboratory (PNNL) is operated by Battelle for the U.S. Department of Energy under the contract DE-AC05-76RL01830.

Acronyms and Abbreviations

APA	Automated Particle Analysis
EDS	X-ray Energy Dispersive Spectroscopy
csv	common separated values
dpm	disintegrations per minute
DST	Double-Shell Tank
FY	fiscal year
NA	not applicable
NIST	National Institute of Science and Technology
PLM	Polarized Light Microscopy
PNNL	Pacific Northwest National Laboratory
PSD	particle size distribution
PSDD	particle size and density distribution
SAL	Shielded Analytical Laboratory
SE	Southeast
SEM	Scanning Electron Microscopy
SDD	Silicon Drift Detector
SST	Single Shell Tank
STEM	Scanning Transmission Electron Microscopy
TEM	Transmission Electron Microscopy
WTP	Hanford Waste Treatment and Immobilization Plant

Units

keV	kilo electron volts
mm	millimeter
nm	nanometer
µm	micrometer
s	seconds
wt %	weight percent

Contents

Figures

Tables

1.0 Introduction

The Hanford Site in Eastern Washington State has approximately 56 million gallons of nuclear waste remaining from plutonium production contained in 177 underground storage tanks.(R.E. Gephart, 2003; Roy E Gephart, 2003; Peterson et al., 2018) Nine different plutonium production reactors operated between 1944 and 1987. These reactors used uranium metal fuel and converted a small fraction of the ^{238}U in the fuel into plutonium (primarily ^{239}Pu). The plutonium was extracted from the irradiated uranium fuel by chemical means, and four processing plants were built to accomplish this: T-Plant, B-Plant, REDOX (REDuction OXidation), and PUREX (Plutonium URanium EXtraction) plants. These processes enabled the separation of plutonium from the spent fuel and generated radioactive liquid waste, which was then stored in underground waste tanks. The Hanford tank wastes consist of a mixture of liquid supernatant, a precipitated salt cake and a sludge component (Colburn & Peterson, 2021; Peterson et al., 2018).

A major concern at the WTP is the potential for pipe plugging. Various tests have been performed to address the *deposition or critical velocity* of the wastes or waste simulants. The critical velocity is defined as the fluid transport velocity at which solid particles begin to deposit on the bottom of a straight horizontal transfer line during slurry transport (Poloski et al., 2009). Poloski and coworkers concluded that the settled particles would be predominately of high-density or possess large particle sizes (or only a small fraction would need to be oversized to have a deleterious effect). Wells et al. (Wells et al., 2007; Wells et al., 2011) used reported Hanford tank characterization data to develop PSDD although less than 20% of the Hanford sludge inventory has been currently characterized by PSDDs. Furthermore, much of specific phase characterization information was based on a limited number of Hanford waste sludge images obtained from SEM. The SEM is a powerful tool for analyzing materials; however, the collection and analysis of SEM data requires a human operator resulting in both low acquisition throughput and the introduction of bias. The objective of this study has been to resolve these issues by running the SEM autonomously over long time periods by utilizing APA software to control the microscope. This can enable thousands of individual analyses to be obtained that can enable PSD for specific phases enabling the density of each phase to be estimated and hence the PSDD within each tank waste segment (Allred et al., 2024). The PSDD can then be used to assess possible critical velocity concerns.

Of the twenty-eight double-shell tanks at Hanford, twenty-five are in the 200 East Area of the site. Figure 1.1A shows the sources of sludge in the SE quadrant along including the major tank sludges involved in this study (Westesen et al., 2023). The overall composition of AN-106 is shown in the pie diagram in

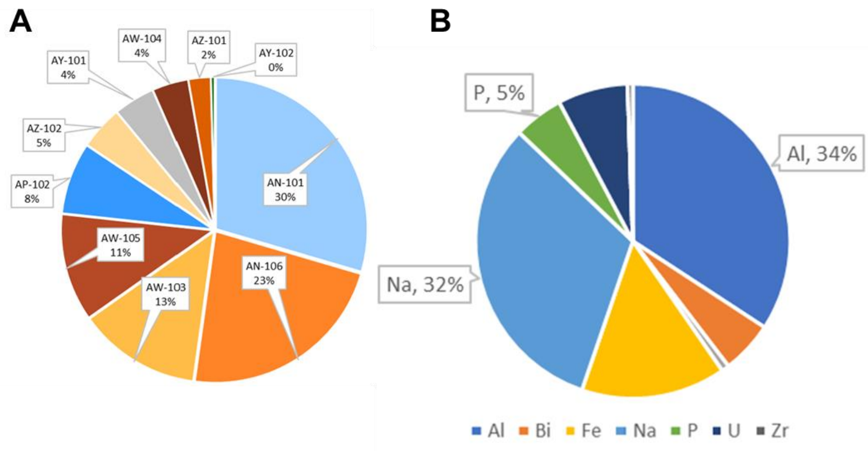

Figure 1.1B.

1.1 Tank 241-AN-106

Tank 241-AN-106, henceforth referred to as 'AN-106' is one of seven DSTs in the 200 East Area AN tank Farm (Douglas, 1996). The DST design improved structural integrity and accessibility for inspection compared to the initial single shell tanks (SSTs). The AN-106 tank went into service in 1981 and received water from tank 241-AN-101. In 1983, the tank received concentrated phosphate waste and noncomplexed waste from tank 241-AW-102. In 1984, the tank received a small volume of unknown waste. In 1993, waste was transferred from AN-106 to tank 241-AP-102. In September 1994, AN-106 received double-shell slurry feed waste from tank 241-AW-106. After May 31, 1995, no additional recordable transfers into or out of the tank were made until efforts started on the transfer of wastes from the SST in the C-tank farm that were initially constructed between 1943 and 1944. These transfers were made owing to the potential risk of SST leakage. Since 1997, more than three million gallons of wastes have been transferred to the DSTs, including AN-106 (Dodd, 2008). In 2003, sludge from tank 241-C-106 was removed and transferred to AN-106 using a 0.9 M oxalic acid solution in combination with hydraulic sluicing. This process dissolved and suspended much of the solids and enabled them to be pump into the DST. The goal was to lower the sludge volume from about 68,137 to 10,599 L (Cantrell et al., 2006; Deutsch et al., 2011).

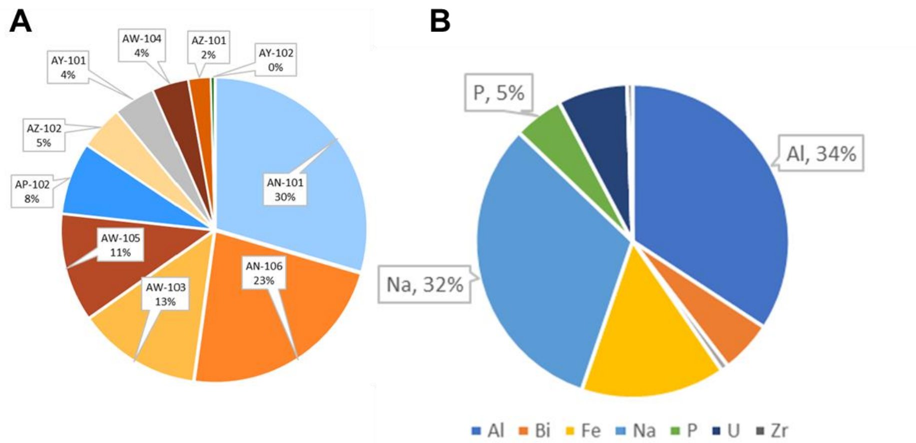

Figure 1.1 (A) Sources of Sludge in the SE Quadrant with major portions coming from AW-105, AN-101, and AN-106 investigated in this study, and (B) AN-106 Sludge composition

The most prevalent metals in the Hanford Tank wastes include sodium, aluminum, iron, and uranium. AN-106 is dominated by sodium and aluminum, with iron being another important component. Phosphorus, uranium, and bismuth are minor components. Not all sludge segments from the available samples of AN-106 were analyzed in this study. The ones shaded in yellow in Table 1.1 were the ones analyzed with SEM-APA methods. Given the major elements identified, the major phases expected would be gibbsite ($Al(OH)_3$) and hematite (Fe_2O_3) (Finch & Ewing, 1997). The plot in Figure 1.2 describes the major phases reported (based on chemistry) in AN-106. Gibbsite dominates in AN-106-14 and is lowest in segments 19LH and 20UH where clarkeite ($Na(UO_2)O(OH)_{0\text{-}1}$) dominates. Gibbsite increases again in segments 20LH to 22LH. One discrepancy between the chemical analyses reported in Figure 1.1B and the phases reported in Figure 1.2, are sodium-bearing phases. Given the quantity of sodium in the wastes, only two phases were assigned as sodium-bearing were natrophosphate ($Na_7F(PO_4)_2{\bullet}19H_2O$) (Bolling et al., 2019; Herting & Reynolds, 2016) and clarkeite. The occurrence of nitrate which is pervasive in the wastes was not noted or included in this study. The Hanford tank supernates are typically alkaline solutions made up of sodium salts, including $NaNO_3$, and $NaNO_2$. The saltcake layer is primarily precipitated $NaNO_3$. However, some nitrate-containing phases would be reported in the sludge such as nitrate-cancrinite ($Na_8(K,Cs)(AlSiO_4)_6(NO_3)_2{\bullet}nH_2O$) (Buck & McNamara, 2004).

Table 1.1 List of Hanford Tank Waste segments with identification numbers and laboratory notebook references

Tank / Facility	Jar Number	Core and Segment Identification	Laboratory ID Number	Reported Net Mass (g)

241-AN-106	20913	14	S20T016919	79.396
241-AN-106	21006	15 LH	S20T017241	33.256
241-AN-106	20918	15 UH	S20T017242	41.495
241-AN-106	21314	16 LH	S20T017587	46.735
241-AN-106	21315	16 UH	S20T017588	52.411
241-AN-106	21357	18 UH	S20T017662	39.586
241-AN-106	21360	19 LH	S20T017884	11.396
241-AN-106	21361	19 UH	S20T017885	23.167
241-AN-106	21362	20 UH	S20T018179	15.251
241-AN-106	21366	21 UH	S20T018217	18.428
241-AN-106	21367	22 UH	S20T018254	39.474
241-AN-101	21407	14UH	S21T021230	15.427
241-AN-101	21415	18LH	S21T021675	44.596
241-AN-101	21417	19LH	S21T021747	49.361
241-AW-105	20326	8LH	S06T000217	29.267
241-AW-105	19262	8UH	S06T000220	47.916

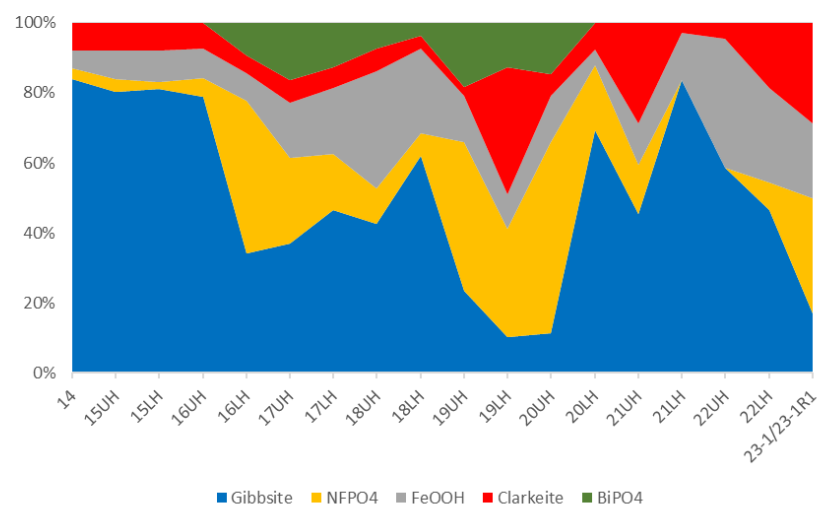

Figure 1.2 Sludge composition with segments in AN-106

1.2 Tank 241-AN-101

Tank 241-AN-101 (AN-101) was the receiver tank for retrieval of tanks 241-C-102 (C-102) and 241-C-111 AN-101-21415 (C-111) which received first-cycle decontamination waste from the bismuth phosphate process and PUREX cladding waste (RPP-RPT-57458, Derivation of Best-Basis Inventory for tank 241-C-102 as of January 1, 2016, and RPP-RPT-48459, Derivation of Best-Basis Inventory for tank 241-C-111 as of April 1, 2016) (see Figure 1.3). The primary constituents in the sludge of tank 241-C-111 were sodium, nitrate, phosphate, nitrite, uranium, carbonate, iron, and aluminum.

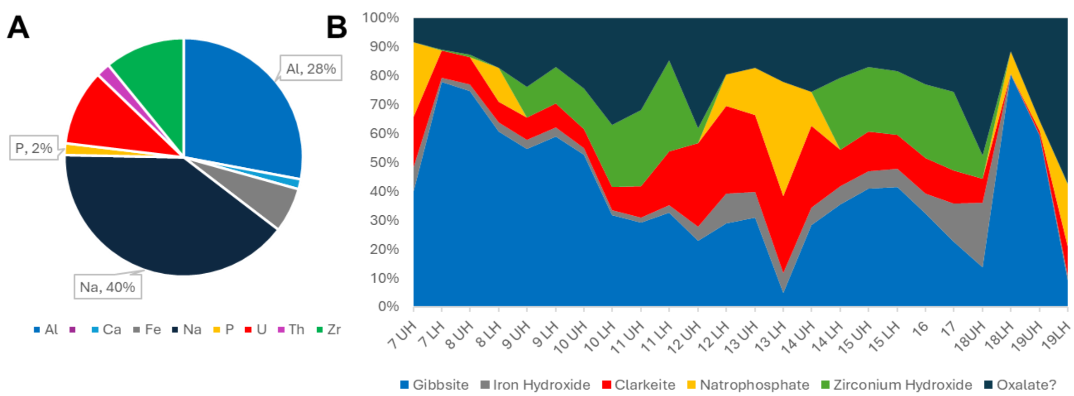

Figure 1.3 (A) Estimated composition of AN-101 from Best-Basis Data and (B) Plot showing the major phases present through AN-101

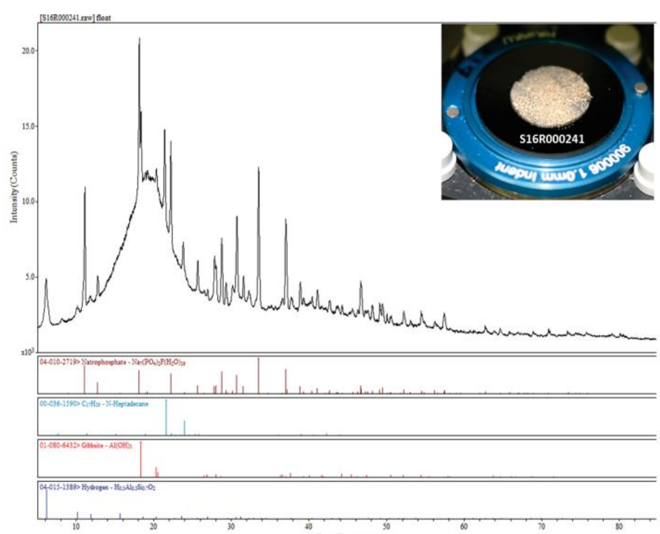

Figure 1.4 x-ray diffraction (XRD) from AN-101 (taken from (Kraft & Meznarich, 2017) showing natrophosphate and gibbsite as major phases.

Natrophosphate was identified as the only major phase (see Figure 1.4). Gibbsite and iron carbonate hydroxide were identified as a minor phase contribution to the pattern while the aluminum/silicon oxide phase was identified as a barely detectable phase.

1.3 Tank 241-AW-105

Double-Shell Tank, 241-AW-105, henceforth referred to as AW-105, is a 23-meter diameter cylindrical tank with a capacity of 3.8 million Liter. It contains 1,643,000 L of waste from the processing of fuel at the PUREX facility. Much of the waste was derived from the de-cladding of Zircaloy-clad metallic uranium fuel that was treated using the 'Zirflex' process. The Zirflex process involved dissolution of the cladding materials in ammonium fluoride (Lumetta, 1994). As a result, AW-105 wastes are dominated by Zr- and F-bearing solids and these have been characterized by XRD and SEM by Reynolds and coworkers revealing the occurrence of the fluoride mineral, villiaumite (NaF) and undefined Zr-oxide (see **Error! Reference source not found.**) (Reynolds et al., 2014). Tank AW-105 also contains sludge from K-Basin. K-Basin sludge is different from other wastes currently stored at the tank farms. Plutonium generated when the uranium was irradiated in the reactor was not removed, thereby resulting in a higher plutonium/uranium ratio than in most tank waste. The predominant waste constituents in the solids have been determined to include sodium (1.05×10^5 µg/g), zirconium (69,200 µg/g), potassium (8,080 µg/g), aluminum (2,280 µg/g), iron (1,450 µg/g), silicon (3,820 µg/g), fluoride (56,000 µg/g), nitrate (28,100 µg/g), nitrite (7,770 µg/g), and carbonate (7,430 µg/g). The most prevalent soluble analytes include aluminum (1,040 µg/g), sodium (19,400 µg/g), hydroxide (6,550 µg/g), carbonate (1,990 µg/g), fluoride (3,200 µg/g), nitrate (159 µg/g), and nitrite (149 µg/g) (DiCenso et al., 1994; Sasaki, 1997).

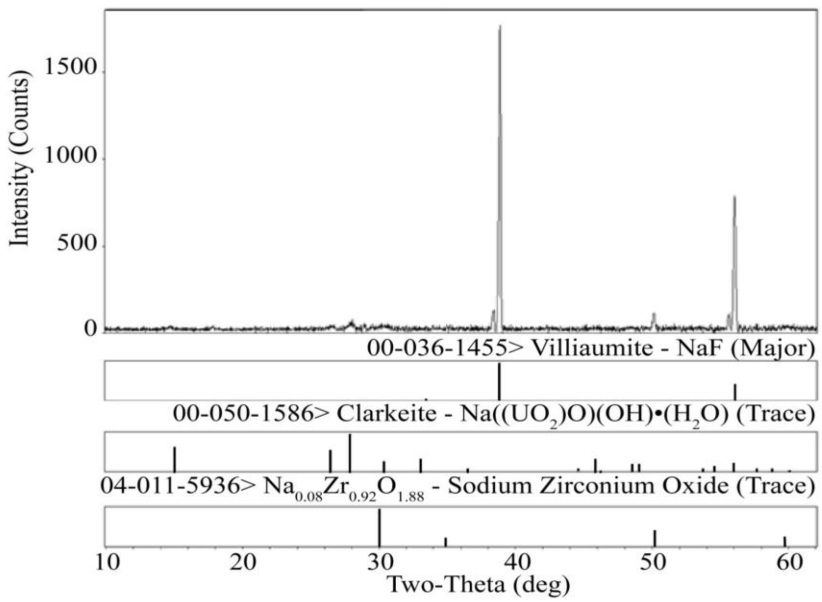

Figure 1.5 XRD of washed AW-105 reported by Reynolds and coworkers (Reynolds et al., 2014) showing NaF (Villiaumite) as the major phase present.

The results reported by Reynolds et al. (Reynolds et al., 2014) are useful for interpreting the data obtained in this study. The major phase observed was NaF (Villiaumite) that was positively identified with XRD (see **Error! Reference source not found.**). Uranium-bearing phases were also tentatively identified as clarkeite.

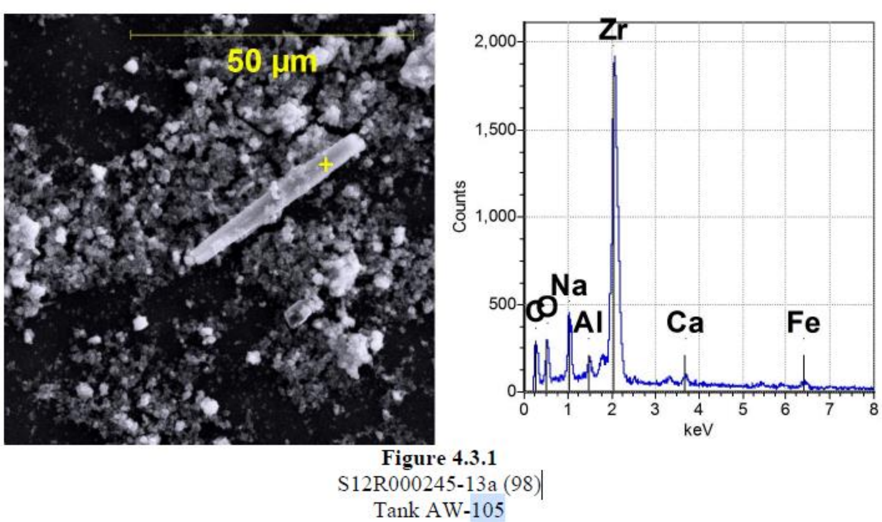

Figure 1.6 An example taken from the work of Herting and coworkers showing common particles from the solids characterization of AW-105 identified as an (A) SEM image of and elongated particle that was identified as (B) Zr-bearing phase with EDS (Herting et al., 2015).

Herting and coworkers have also confirmed the occurrence of NaF in AW-105 sludge with polarized light microscopy (Herting et al., 2015). In **Error! Reference source not found.**, a Polarized light microscopy (PLM) image of NaF particles is shown.

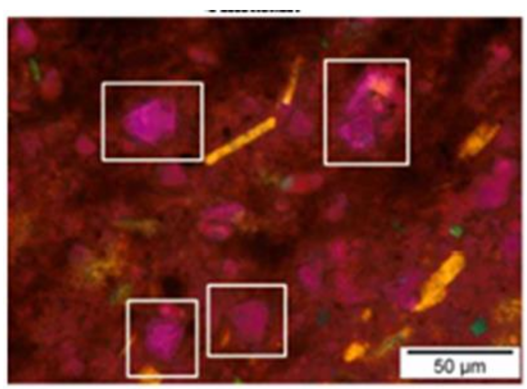

Figure 2.9.3
S12R000245z3 (98)
Tank AW-105

Figure 1.7 NaF in-Tank waste sludge AW-105 identified with PLM, taken from Herting and coworkers (Herting et al., 2015).

Results and discussion of AN-101 and AW-105 wastes are described later in this report. Additional results on AW-105 wastes are also reported elsewhere (Allred et al. 2025).

In this study, standard SEM analysis combined with APA was used to characterize prepared sub-samples of the dried Tank waste. For each tank waste (AN-106, AN-101, and AW-105), several segments along a vertical core of the tank waste were obtained. It was not possible to analyze every segment received; however, for AN-106, multiple segments were characterized. For AW-105 and AN-101, two and three segments, respectively were characterized. The total mass of each segment received into the SAL hot cells was between 10 and 60 grams. For SEM sample preparation, a sub-sample was extracted from SAL which weighed between 50 and 100 milligrams. For the SEM stub preparation, the total amount of material was a fraction of this quantity. Nevertheless, the total activity on the SEM stubs was between 50,000 displacements per minute (dpm) and 400,000 dpm. The total activity of the SEM stubs limited the amount of material that could be examined in the microscope. Higher amounts presented both a contamination risk and could lead to damage to the EDS detector. For each segment sub-sample elemental maps and images were collected to provide an overview of the material. The APA data was collected from as many particles as possible.

2.0 Experimental Procedure

2.1 Scanning Electron Microscopy with x-ray Dispersion Spectrometry (SEM-EDS) of Hanford Tank wastes

The SEM for APA work was operated with an accelerating voltage of 20 keV and a spot size of 5.5 using the backscattered electron (BSE) detector and under low-vacuum mode (using ~100 Pa N_2 gas). This gave count rates on the order of 40,000 to 80,000 counts/second). The SEM magnification scale was checked against a NIST traceable standard, MRS-4. Magnification was within 1% of the expected value. The energy scale was checked by looking at high and low energy x-rays from known materials. Examination was carried out using a FEI (Thermo-Fisher, Hillsboro, OR) Quanta™250 Field Emission Gun equipped with a BSE detector and EDAX™ (Ametek, Inc., Mahwah, NJ) x-ray EDS system running Genesis™ software.

2.2 APA of Hanford Tank wastes

APA methodology uses gray-level contrast from the BSE image for particle image segmentation. Each field of view was divided into two or more contrast regions based on BSE contrast selected by the operator. These regions were examined separately, so that small high atomic number (Z) particles attached to larger low Z particles could be both independently analyzed for composition and morphology (see Figure 2.1). Owing to the beam penetration, the composition of the heavy particles may be mixed partly with the lighter phases. In most instances, the phase classification was established prior to the initiation of the analysis and was saved as a library file. This library file could also be applied to different samples to make the analyses consistent between specimens. If a phase remained unidentified (or termed 'unclassified'), the operator can re-categorize the phase in the SEM software, or this could be performed during the analysis of the data-frames in the Juypter Notebooks. The data reported from APA included, the position of each particle, an image of the particle, the EDS spectrum, the particle diameter, perimeter, area, axial ratio, goodness of fit to computer predicted phase, and composition. The data was exported as a comma separated values (csv) files. The csv files needed a small number of edits to make them readable. These files were combined into a single dataframe that was then analyzed with Jupyter Notebook scripts (see Appendix) to develop plots and figures. All data (including complete spectra and images) was saved, archived for future retrieval, and can be re-analyzed with new criteria, if needed.

The plots and data developed for each segment included ternary diagrams for major elements, log-normal plot of the major phase contrast particle types, bubble plot of Al-bearing compounds, histograms for the size distributions for the major phases identified, elemental maps, and images and spectra of selected particles.

However, these particles are heterogeneous and the high Z particles are held tenaciously to the larger low Z particles. It is important to select the correct histogram width to show PSDD (Alxneit, 2020).

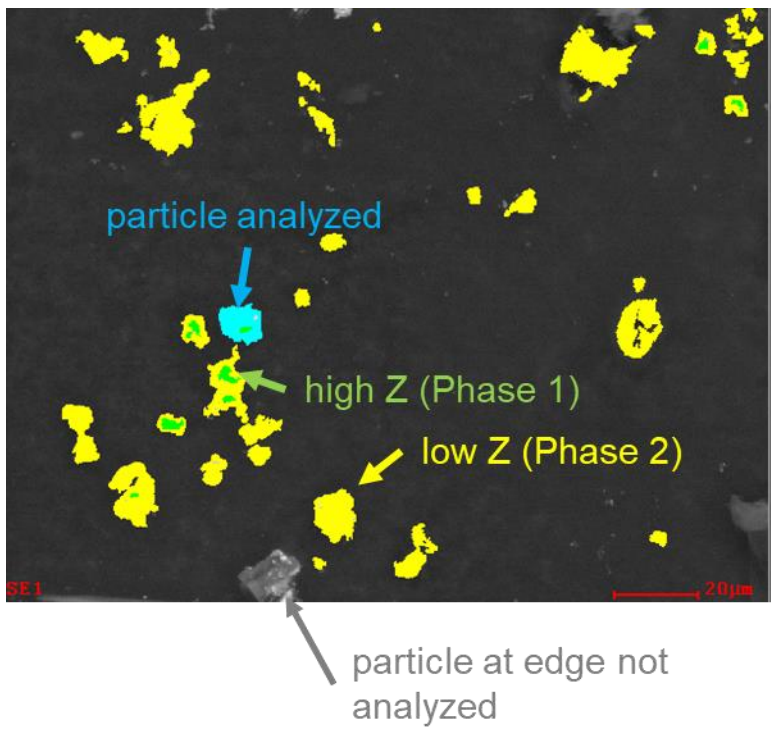

Figure 2.1 SEM image showing the operation of the APA on two different gray-level regions.

In general, the SEM-APA analysis was conducted on between ~15K to ~40K individual particles per SEM stub. Particles were classified according to 'EDS composition-selected' possible phases. An effort was made to keep this consistent between segments, but this was not always accomplished. Phases that were did not match the entered database were labeled as 'unclassified,' however, these could be re-analyzed and re-assigned a specific phase, if needed. The separation of the particles into high Z and low Z regions or 'phases' provides a density distribution on the wastes.

2.3 Categorizing phases

Phases were categorized by the user based on the EDS semi-quantitative analysis of different particle. This enabled a library of compositions to be developed. The software then determined the goodness of fit for any unknown phase compared to the different phases listed in the library. The user had the ability to select any name for a specific composition; however, for Hanford tank waste, phases that were mainly aluminum containing were referred to as 'gibbsite,' iron phases as 'hematite,' and uranium-rich compositions as 'clarkeite.' The phase was chosen based on EDS composition and the likely phase based on knowledge of the specific Hanford tank waste. The objective of this work has been to extract particle size distributions. For example, we acknowledge that Krupka and coworkers showed that a major uranium-bearing phase observed in residual C-tank wastes (the source term for much of the wastes in AN-106) was cejkaite [$Na_4(UO_2)(CO_3)_3$] not clarkeite (Krupka et al., 2006). The important point in these PSDD estimations will be to capture the approximate density rather than to get the precise description of the crystallography. These categories were then used in all further morphological analyses of the particles. The names of some phases were changed during the data analysis if they were considered inaccurate (see Appendix). For instance, in some cases, Zr-bearing phases were initially defined as 'Zircaloy.' This was changed to Zr-hydroxide. The default name for an unknown spectrum was 'none,' and this was changed to ' unclassified.'

2.4 Morphological analysis and particle size distributions

The National Institutes of Standards and Technology (NIST) -1984 standard is a mixed Co-tungsten carbide powder that has been used in nuclear forensics morphological studies with SEM to determine the efficiency of sample preparation (McDonald et al., 2024; Olsen et al., 2017; Schwerdt et al., 2018) and to evaluate the ability to determine particle size distributions (see Figure 2.2). By matching the NIST-1984 reported results with the results from APA in this study, we showed that the technique can provide reliable results on particle sizes. In this instance, the APA can be considered a 'black box' operation for comparing against the NIST reported results. There is an indication of bias towards the smaller-sized particles as the 50% value was slightly below the reported NIST value. There was good agreement between the cumulative size distribution in this study and the results reported by NIST. However, a significant fraction of particles below 3 µm were identified during the APA. Nuclear forensics studies have also shown preferential settling of larger particles which is why it was important to survey the entire SEM stub during the APA process. The ability to examine thousands of radioactive particles gives for the first time, data that could be useful for engineering scale operations.

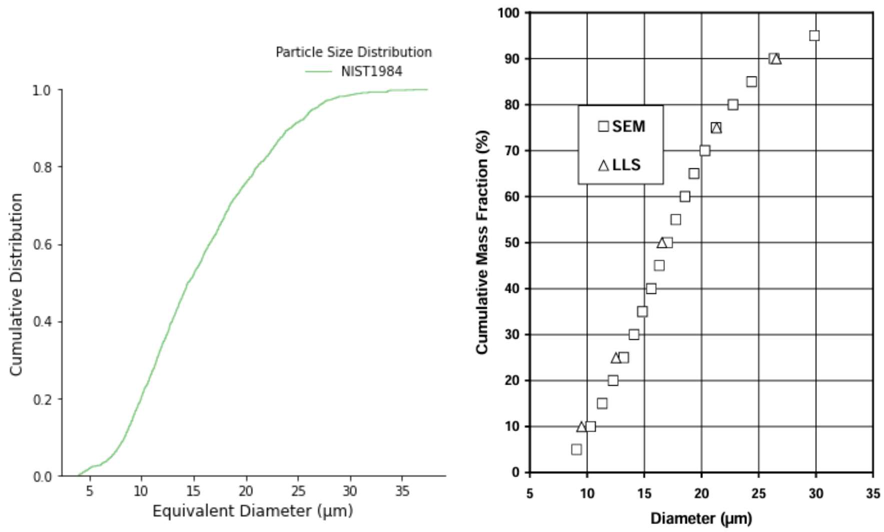

Figure 2.2 Cumulative distribution plots using (A) APA of 1496 individual Co-W- bearing particles from this study and (B) results reported for the NIST-1984 standard.

The NIST standard was also used to test out some of the plotting and compositional functions used in this study. In Figure 2.3, a ternary plot showing the mixed Co-C-W phase is shown together with a plot showing the particle size with tungsten content.

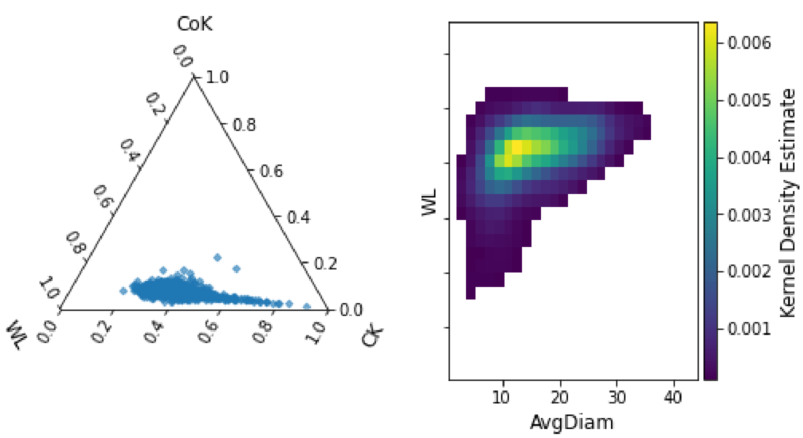

Figure 2.3 Ternary plot showing the compositional range in NIST-1984 and the tungsten content with average diameter

This shows that there is some variation in the signal depending on the orientation of the particles even with a nominally identical phase. This was mainly due to the carbon content which is notoriously difficult to quantify. In this study, both oxygen and carbon were left out of the analysis as these add too many errors to the phase identifications and led to unreliable results.

3.0 AN-106 Solids

3.1 AN-106-14 (20913)

AN-106-14 was the upper section extracted from the core. The segment was dominated by gibbsite based on bulk chemical analysis (see Figure 3.1A); however, the analysis based on SEM analysis, suggested that an aluminate phase was also important (see Figure 3.1B). The bulk chemical analysis did indicate a significant concentration of sodium; however, the listed phases did not include phases that would account for sodium observed. The bulk analysis reported phases, but these were based only on chemistry as there was no physical confirmation of the occurrence of a specific phase. It is possible that the phase identified in the SEM-EDS APA was gibbsite, but the analysis indicated that sodium was found in association with this phase. Nevertheless, both the bulk analysis and the APA suggested a large number of aluminum-based phases. Both the bulk chemistry and the SEM-APA showed the occurrence of the uranium-bearing phase, clarkeite. Again, the term clarkeite is being used for convenience as the best-guess for a uranium phase. In the SEM-APA, we used the total area measured from this phase, and in the bulk chemistry pie chart, the quantity of uranium is being used as the measurement. That these two charts look similar, indicates that the SEM-APA method is approaching the representativeness of the bulk chemistry results. Throughout this work, the quantification of phosphates was imprecise owning to the size and morphology of the phosphates. In some instances, optical microscopy was used but this was not possible for all specimens.

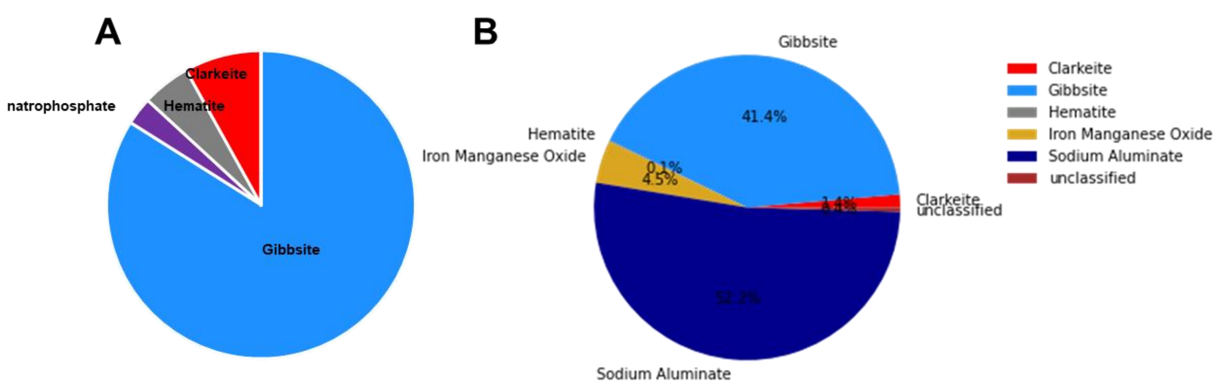

Figure 3.1 (A) Estimated composition of segment AN-106-14 where gibbsite dominates (B) Composition of segment AN-106-14 based on total area of the different phases (not accounting density differences) measured with SEM-APA.

An example of an elemental map from AN-106-14 is shown in Figure 3.2 and Figure 3.3. These maps show the dominance of Al-rich phases in this specimen and supports the bulk analysis.

However, an unidentified silicon-rich phase was also common. In other segments this was identified as cancrinite but in this case, this assignment was not made. Silicon was not reported in any of the chemical analyzes however it was commonly observed in several of the AN-106 segments. In Figure 3.4, two ternary plots are shown. The first ternary plot shows the dominance of aluminum-rich phases, most likely gibbsite. The third plot shows the average particle size correlated with aluminum concentration, demonstrating that the aluminum-rich particles were around 2 µm in diameter.

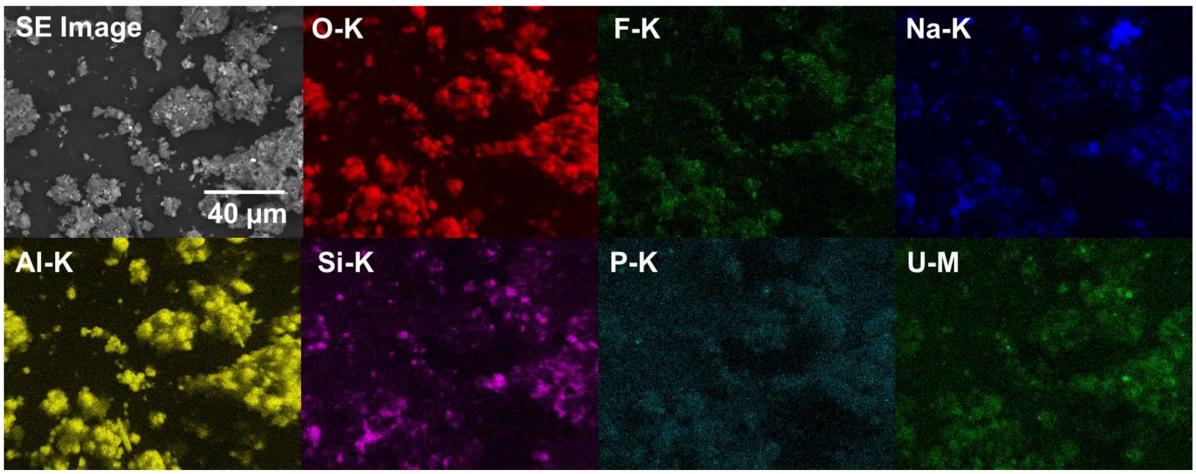

Figure 3.2 SEM-EDS Elemental map of AN-106-14 showing the dominance of Al-rich phases

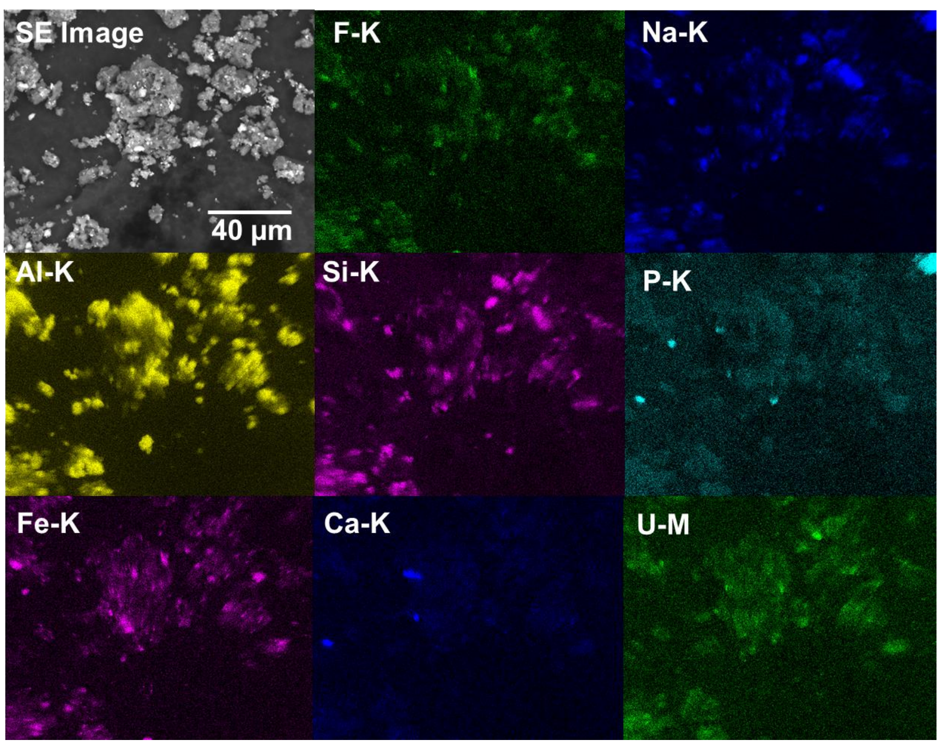

Figure 3.3 SEM-EDS Elemental map of AN-106-14 showing the dominance of Al-rich phases

There was little direct evidence for a bismuth phosphate phase but from the elemental map in Figure 3.3, there was evidence based on the co-incidence of Ca and P of a calcium phosphate (apatite) particles. Uranium particles were also scattered throughout the sample.

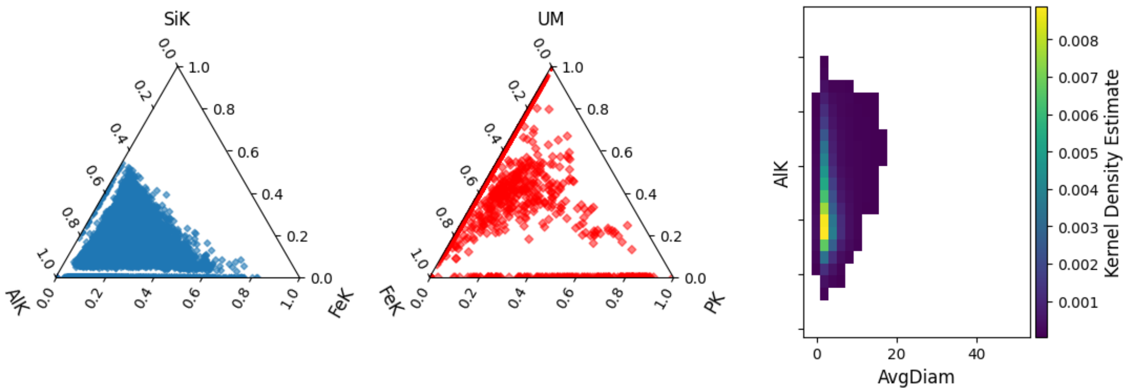

Figure 3.4 Ternary plots for Si-Al-Fe, and U-P-Fe, and a third plot showing Al concentration with particle size.

We can also plot the distributions of particles based on BSE contrast, regardless of the actual phase. The plot in Figure 3.5A, describes two log-normal distributions that reflect the size distributions of the light and heavy fractions in AN-106-14. These two fractions represent the gray-level contrast in the BSE images obtained from the APA. The heavy fraction is bright in BSE imaging and the 'lighter' fraction, is light gray contrast. As brightness under BSE imaging reflects the density or the particle, this is a useful indicator of the low density and high-density factions within the Hanford waste sludge sample. The heavy (high-density fraction) is noticeably smaller in particle diameter than the lighter fraction.

The bubble plot in Figure 3.5B, shows the distribution of aluminum and sodium with phase type (color) and particle size (bubble size). The presence of gibbsite as the high aluminum phase with large particle sizes can be seen. The bubble plot enables four variables to be viewed simultaneously. The x- and y- axes represent the measured amount of aluminum and sodium, respectively. The bubble size is an indication of the particle size, and the colors refer to the different phases. An effort was made to keep consistency in the colors for specific phases in this report. For instance, gibbsite is listed as blue and resides in the lower right of the plot. The sodium aluminate (cyan) had medium levels of the two measured elements and extends in the middle of the plot. As there was nothing in the upper left of the plot, there were no phases that were primarily sodium-bearing, such as oxalate or $NaNO_3$ in this specific sample.

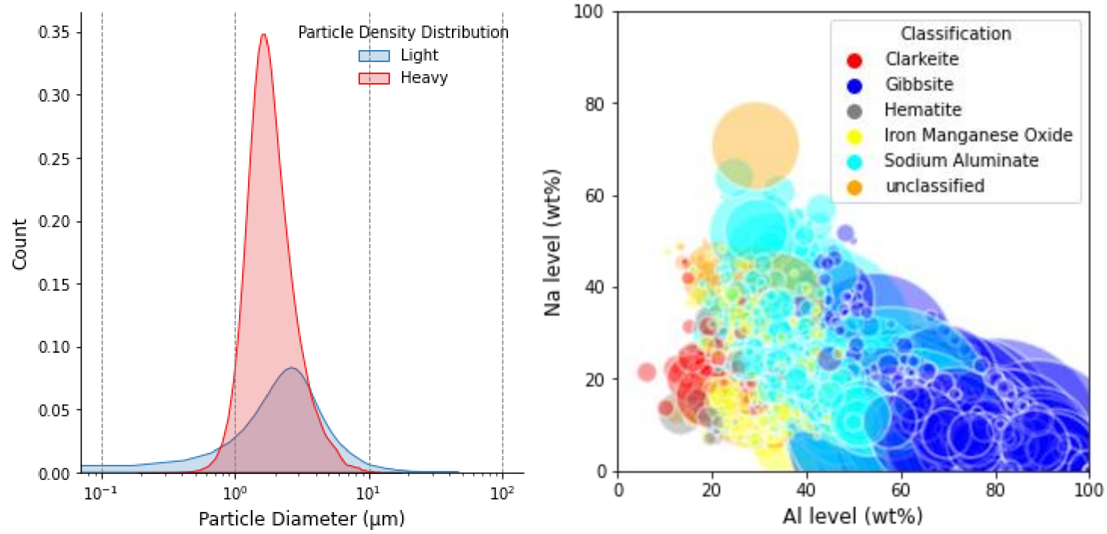

Figure 3.5 (A) Log-normal plot of the two major gray-level regions providing density distributions for AN-106-14. (B) Bubble plot of Na vs. Al content with particle size (bubble diameter), and different colors representing the different phases.

The distributions of individual phases identified in AN-106-14 are shown in Figure 3.6. The major phases all possessed log-normal distributions (although the plots are non-log). A small fraction of the clarkeite and gibbsite particles approach 10 µm in diameter. However, most particles possess an average diameter of 3 to 4 µm. The major phases are tabulated in the conclusion section for AN-106.

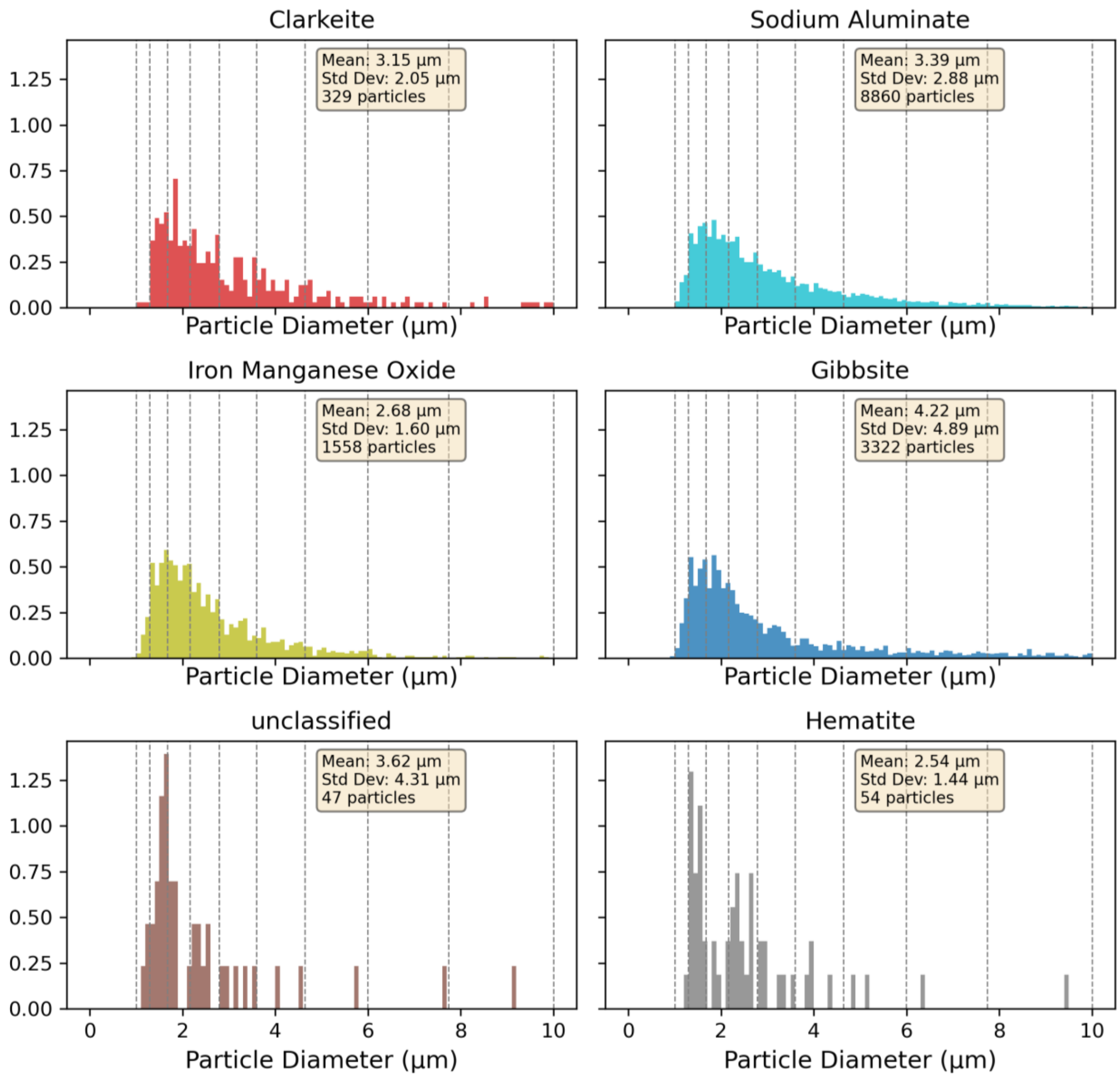

Figure 3.6 Histograms of the major phases found in AN-106-14 with Al-rich phases dominating the sludge sample.

3.2 AN-106-16LH (21314)

In sludge section AN106-16LH, the dominant phases were natrophosphate and gibbsite as defined in Figure 3.7A as 'NFPO4' and 'Gibbsite,' respectively. The SEM-APA based analysis, based on the area of each phase, identified a cancrinite phase as dominant as well as a sodium aluminate (see Figure 3.7B). Gibbsite, hematite, and phosphate phases were identified; however, during the SEM analysis, a U-Fe-Bi composition was also detected. The match between the bulk chemical analysis and the APA is poor. The U phase identified contained both iron and bismuth and no phase that could be linked to clarkeite was identified. Both gibbsite and sodium aluminate phases were found in the APA whereas the bulk chemical analysis only reported gibbsite. The silicon-bearing phase, cancrinite was also routinely identified with SEM-APA, but was not identified with the bulk chemical analysis. Indeed, the bulk chemical analysis failed to report any phase that contained silicon.

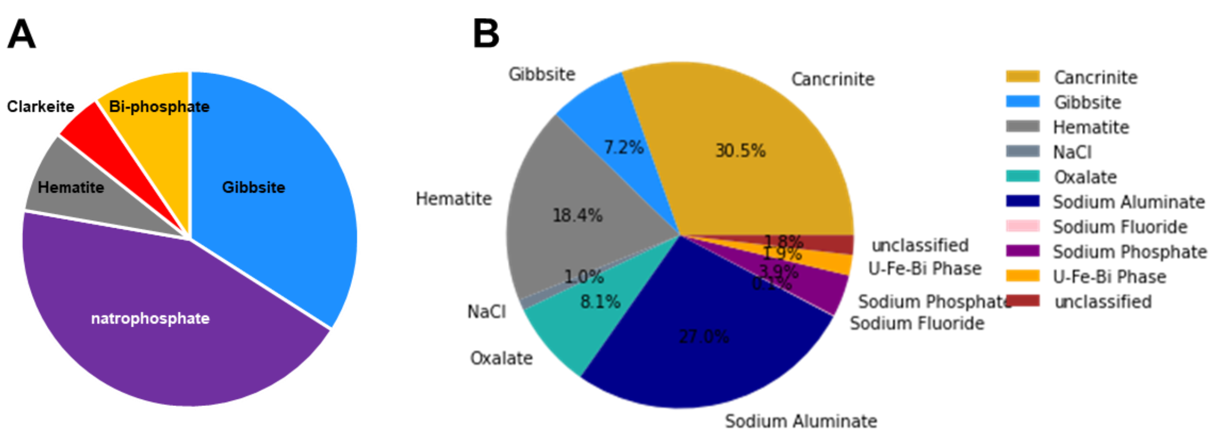

Figure 3.7 (A) Estimated composition of segment AN-106-16LH (top) and (B) Sludge composition based on the SEM data.

The elemental maps from this AN-106 segment are shown in Figure 3.8 and Figure 3.9. There is a strong correlation between uranium, iron, and phosphorus in the elemental maps. Elemental maps of bismuth were not included; however, silicon was ubiquitous in these samples. This is mapped out in the ternary diagrams shown in Figure 3.10. From the elemental maps, some of the aluminum phases, presumably gibbsite, exceed 20 µm in length. The BSE contrast was separated into three components that are shown in Figure 3.11A and the bubble plot shows the gibbsite dominating as the high aluminum, low sodium phase, as expected (see Figure 3.11B). The heaviest fractions (i.e., the U-Fe-Bi phases) were also the smallest and typically attached to other phases. The lightest phase was identified as an oxalate. Note that the identifications made in the

SEM are based on compositions and expected phases, not direct structural determinations. The distributions of all the observed phases are shown in Figure 3.12.

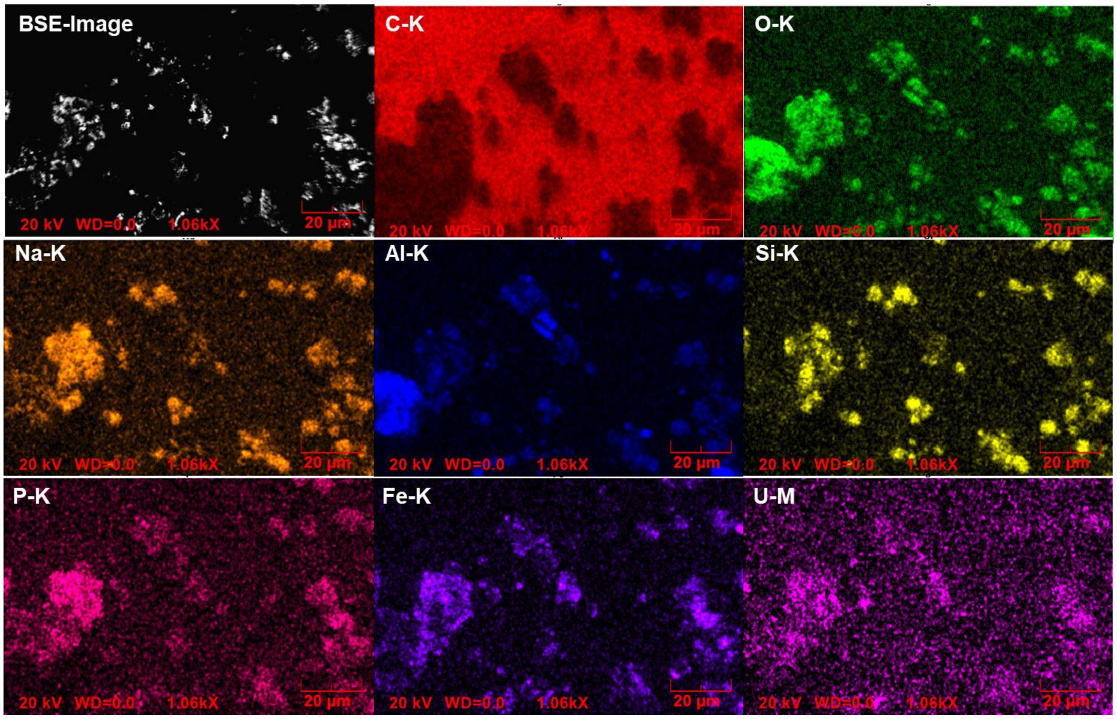

Figure 3.8 SEM-EDS Elemental map of AN-106-16LH showing the dominance of sodium phosphate phases

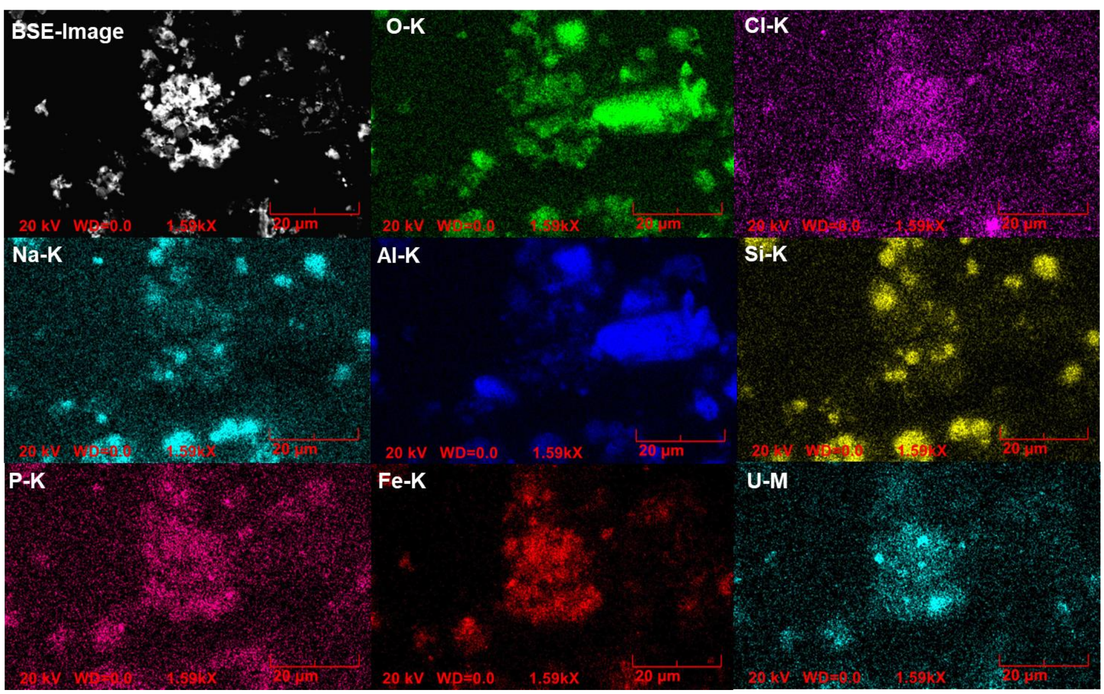

Figure 3.9 SEM-EDS Elemental map of AN-106-16LH showing the dominance of Al-rich phases and particles containing U.

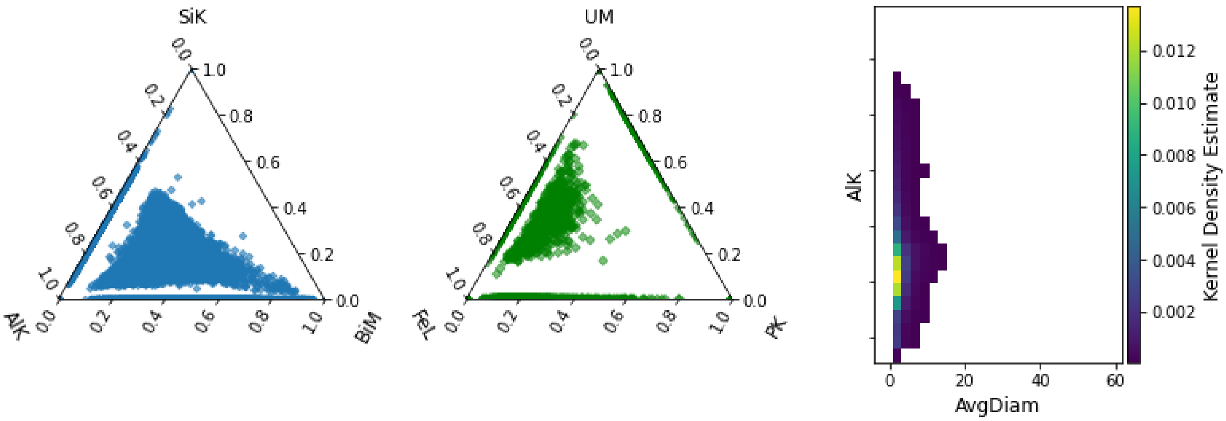

Figure 3.10 Ternary plots for Si-Al-Fe, and U-P-Fe, and a third plot showing Al concentration with particle size.

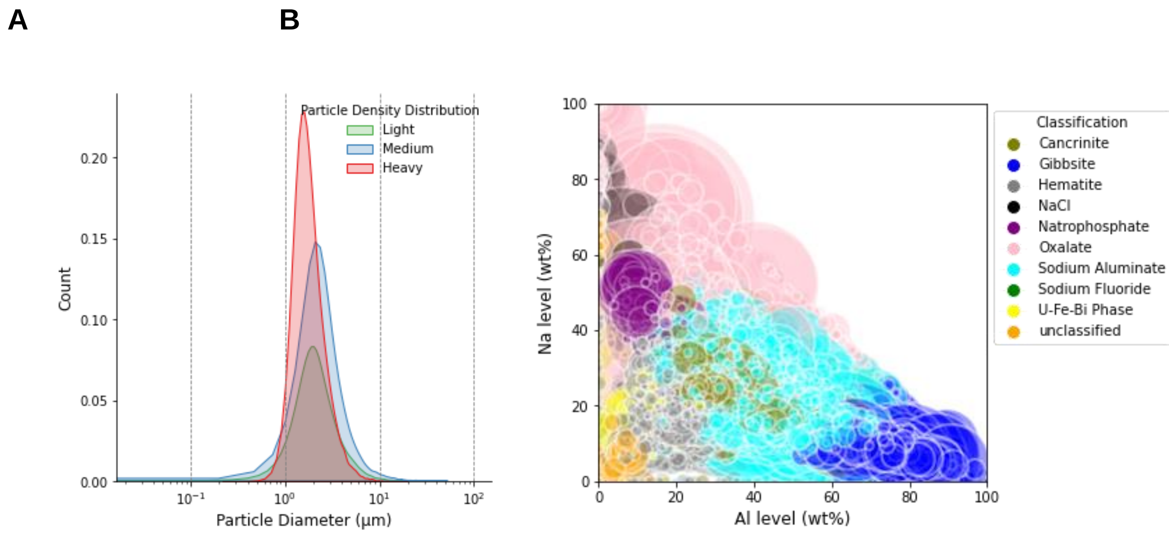

Figure 3.11 (A) Log-Normal Plot of the two major gray-level regions. Region 1 consists of the high Z material and region 2 of lower Z materials which had on average a large particle size. (B) Bubble plot of Na vs. Al content with particle size (bubble diameter), and different colors representing the different phases.

Phases that are marked as ‘unclassified’ were not specifically identified prior to the APA routine. In some instances, it was possible to assign these to a specific phase; however, these often represent a group of minor phases or analyses that could not be assigned to any specific type or phase reliably.

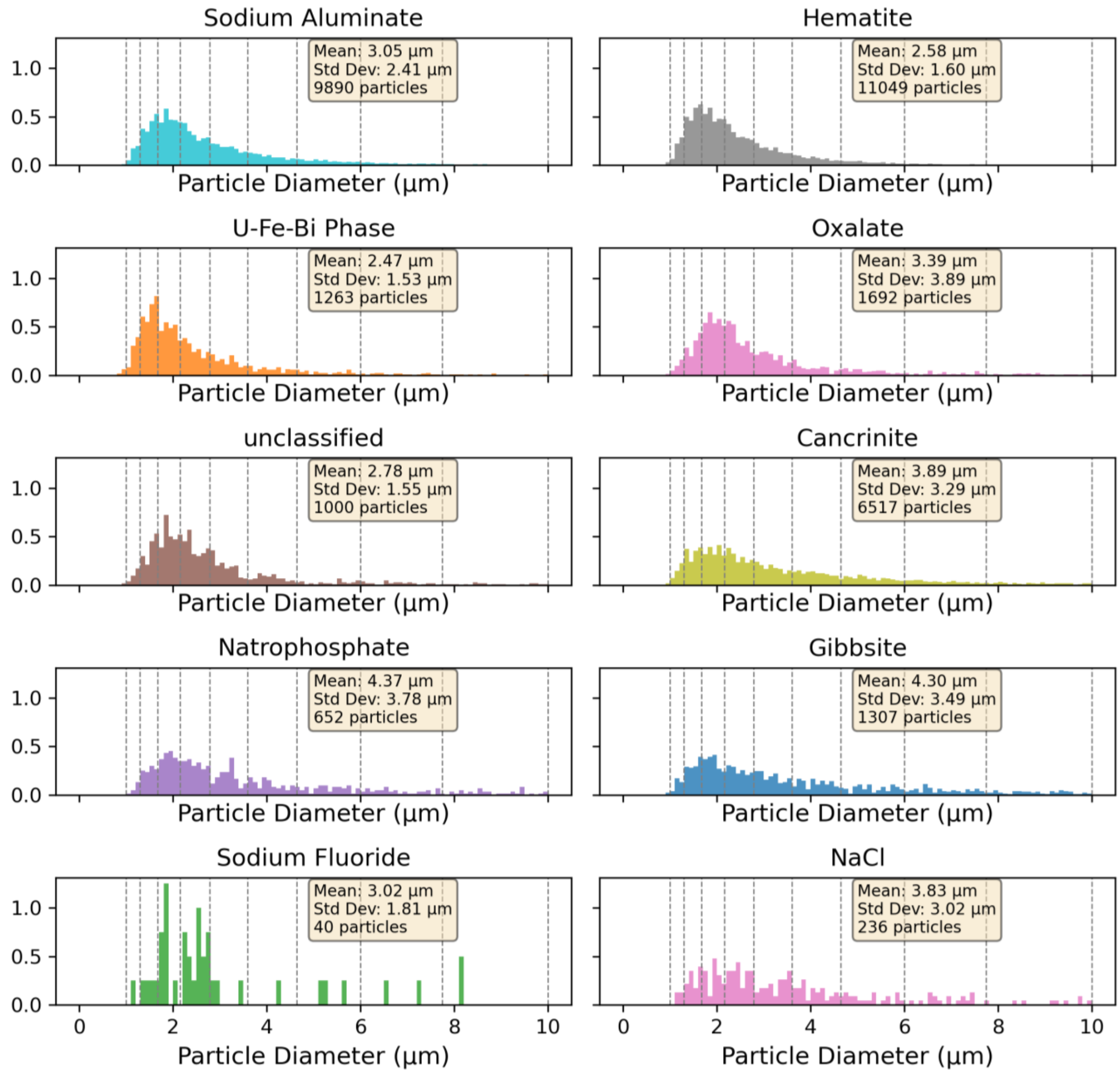

Figure 3.12 Histograms of the major phases found in AN-106-16LH with Al-rich phases dominating the sludge sample.

A total of 33,000 particle analyses were performed on this segment (AN-106-16LH).

3.3 AN-106-19LH (21360)

The breakdown on compositions based on the bulk chemical analysis show in Figure 3.13A indicates that natrophosphate was the dominant phase. This was supported by the SEM analyses (see Figure 3.13B) that also found (based on particle area) that sodium phosphate (possibly natrophosphate) was the dominant phase. A bismuth bearing phase was also identified however the SEM analysis indicated that this was associated with iron rather than phosphate.

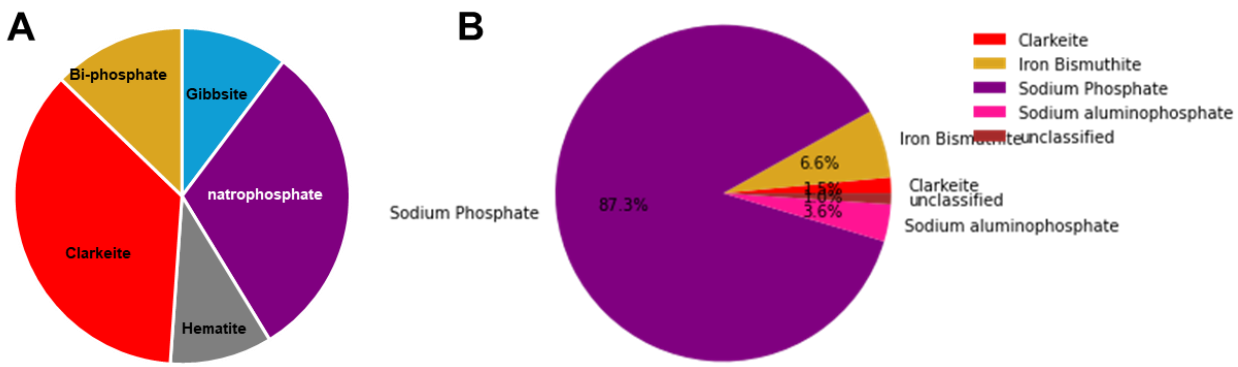

Figure 3.13 (A) Estimated composition of segment AN-106-19LH and (B) sludge composition based on the SEM data.

SEM elemental maps provide a snapshot of the specimen but do not always reveal the trends in the entire sample (see Figure 3.14). The elemental maps indicate the presence of a mixed U-Fe-Bi phase.

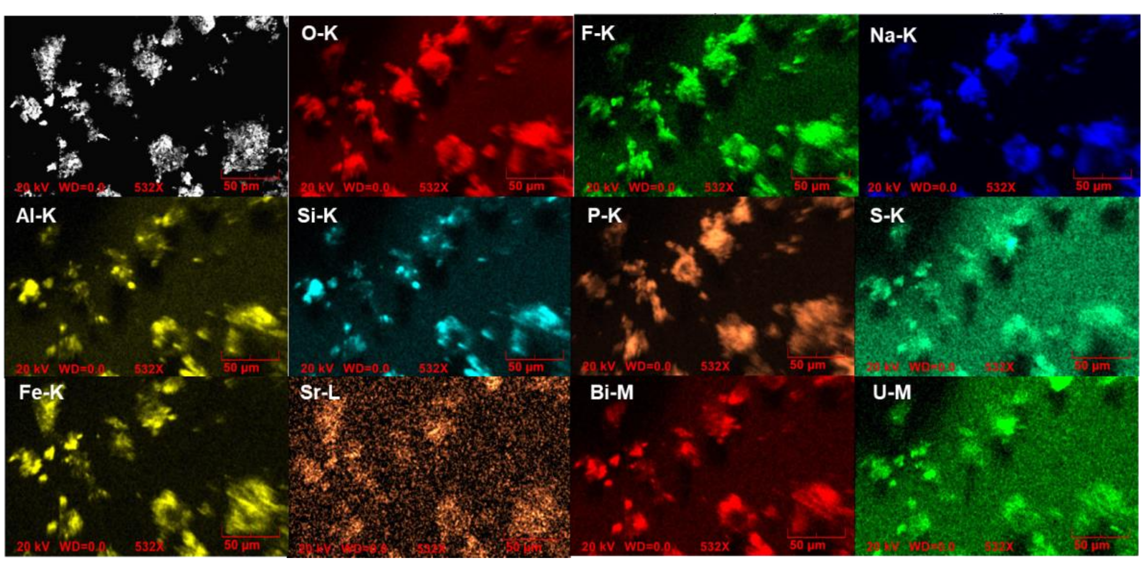

Figure 3.14 SEM-EDS Elemental map of AN-106-16LH showing the dominance of Al-rich phases and particles containing U.

Further evidence for the U-Fe-Bi phase can be seen in the ternary diagrams in Figure 3.15. This also shows that this segment was depleted in gibbsite relative to other segments. There was no clear evidence for an iron oxyhydroxide (FeOOH) phase (i.e., hematite) as iron seemed to be associated with the uranium and phosphorous and with the bismuth in separate phases.

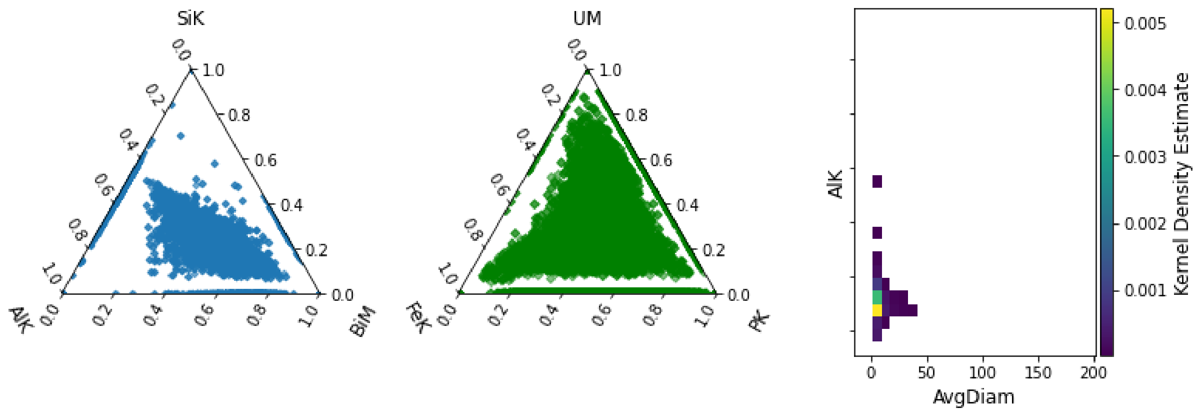

Figure 3.15 Ternary plots for Si-Al-Fe, and U-P-Fe, and a third plot showing Al concentration with particle size.

Figure 3.16A shows the BSE contrast of the particles on a log-normal plot and the bubble chart is dominated by the large phosphate phases (see Figure 3.16B).

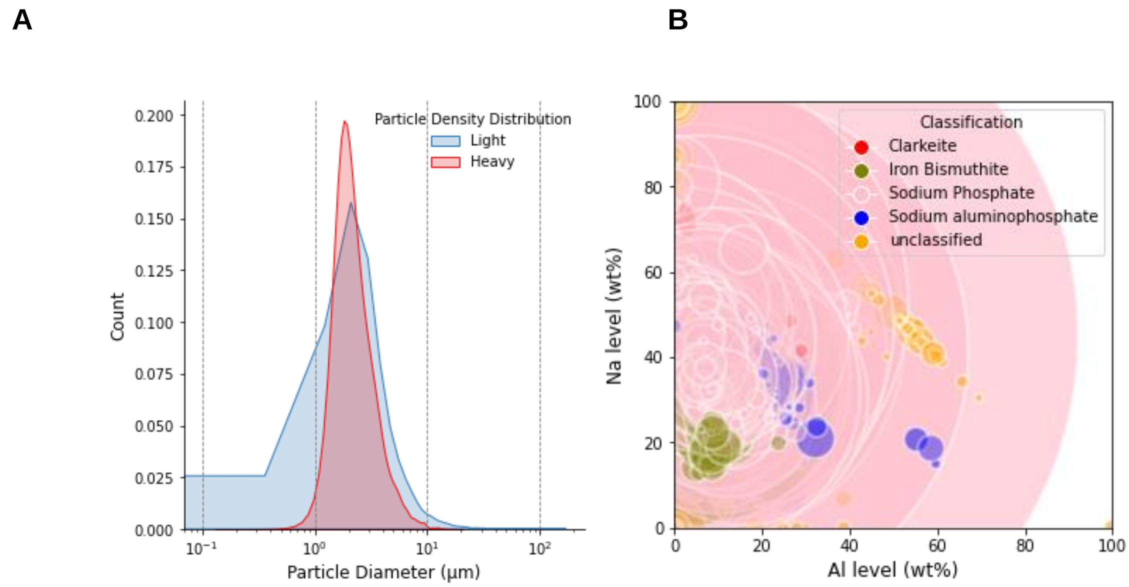

Figure 3.16 (A) Log-normal plot of the two major gray-level regions. Region 1 consists of the high Z material and region 2 of lower Z materials which had on average a large particle size. (B) Bubble plot of Na vs. Al content with particle size (bubble diameter), and different colors representing the different phases.

The particle size distributions for each phase are shown in Figure 3.17 showing a bismuth- phase, both a sodium phosphate and an alumino-phosphate, and clarkeite, as the major phases. The sodium phosphates were larger than the natrophosphates.

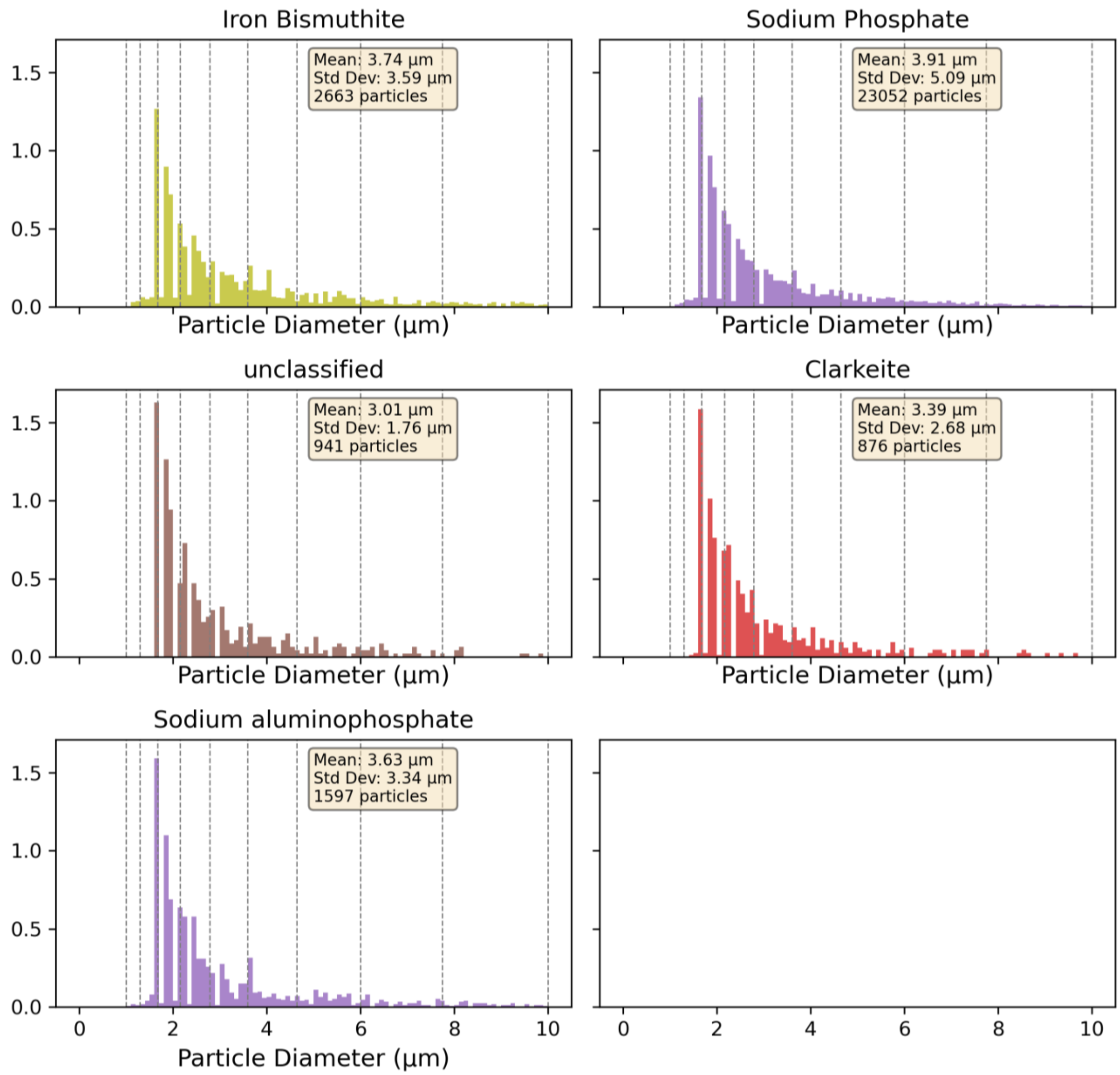

Figure 3.17 Histograms of the major phases found in AN-106-19LH with phosphate phases dominating the sludge sample.

A total of 29,000 particles were analyzed in this segment.

3.4 AN-106-19UH (21361)

The match between the bulk chemical analysis breakdown and the analysis based on SEM particle area was reasonable for segment AN-106-19UH where natrophosphate was identified as the major phase (see Figure 3.18A). However, gibbsite was not reported in the SEM analysis (see Figure 3.18B). This can be seen in the SEM elemental maps that do not show aluminum isolated from other elements but always associated with sodium and phosphorus (see Figure 3.19).

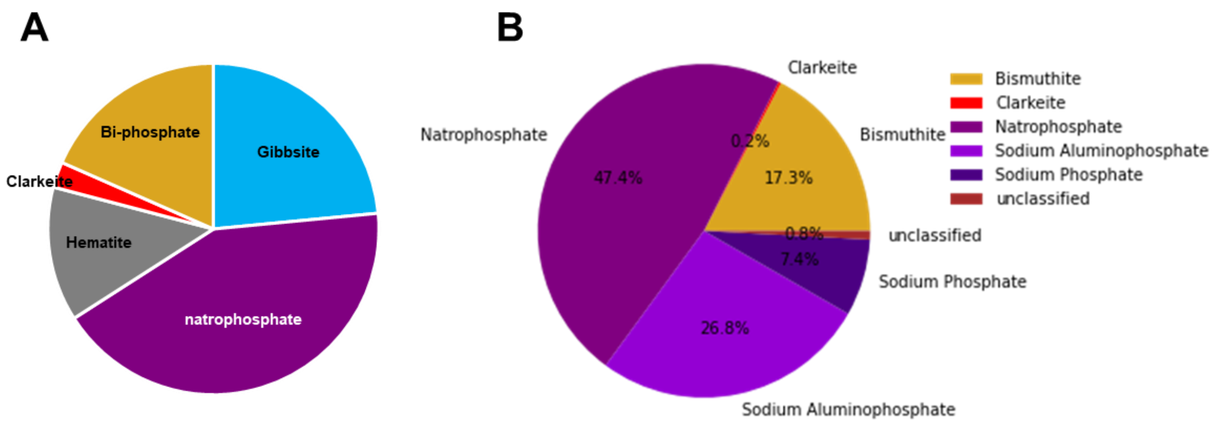

Figure 3.18 (A) Estimated composition of segment AN-106-19UH and (B) sludge composition based on the SEM data.

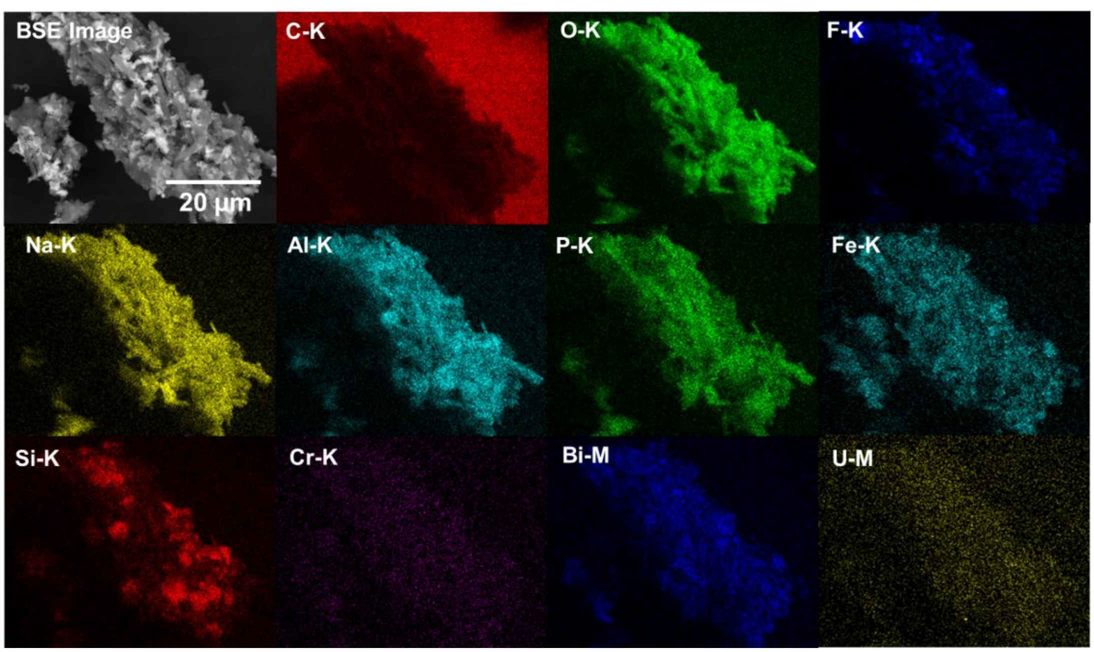

Figure 3.19 SEM-EDS Elemental map of AN-106-19UH showing the dominance of sodium phosphate phases

A lower magnification elemental map is shown in Figure 3.20. The resolution of these elemental mas does not easily enable the determination of specific phases. Note that the intensity in the individual elemental maps reflects the observed signal rather than a quantitative value.

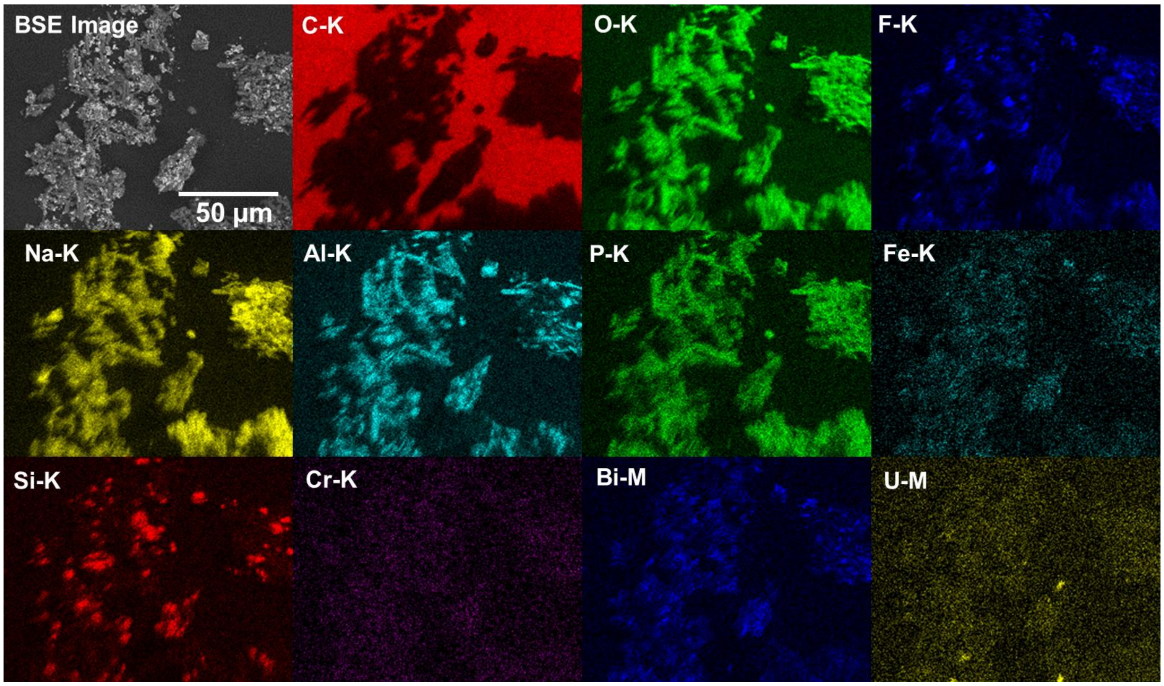

Figure 3.20 SEM-EDS Elemental map of AN-106-19UH showing the dominance of sodium phosphate phases

The ternary diagrams in show the presence of a Bi-rich phase that is not directly associated with the phosphate phases (see Figure 3.21).

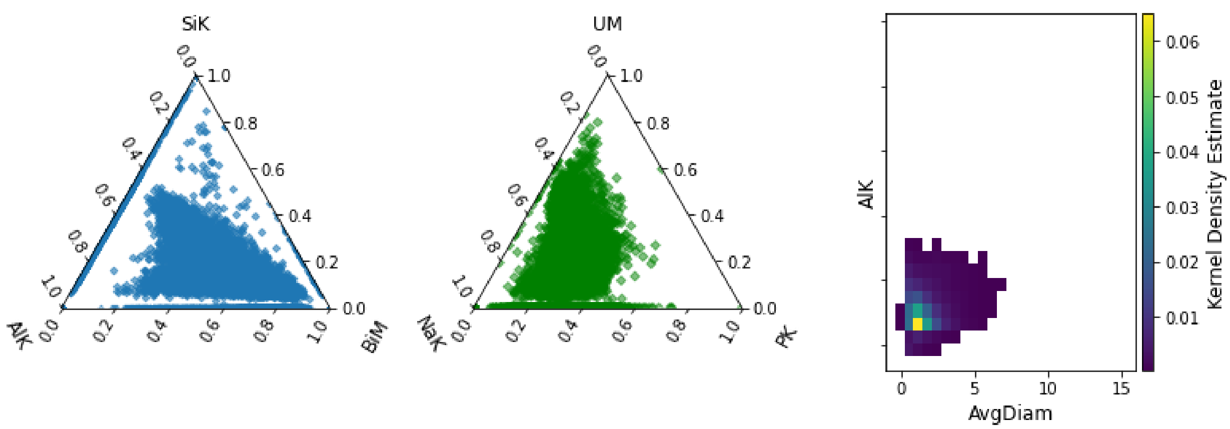

Figure 3.21 Ternary plots for Si-Al-Fe, and U-P-Fe, and a third plot showing Al concentration with particle size.

The log-normal distribution plot in Figure 3.22A shows a bimodal distribution for the lighter phase where some appear to have small particle diameters. The bubble plot Figure 3.22B, again shows that lack of aluminum-bearing phases in this segment.

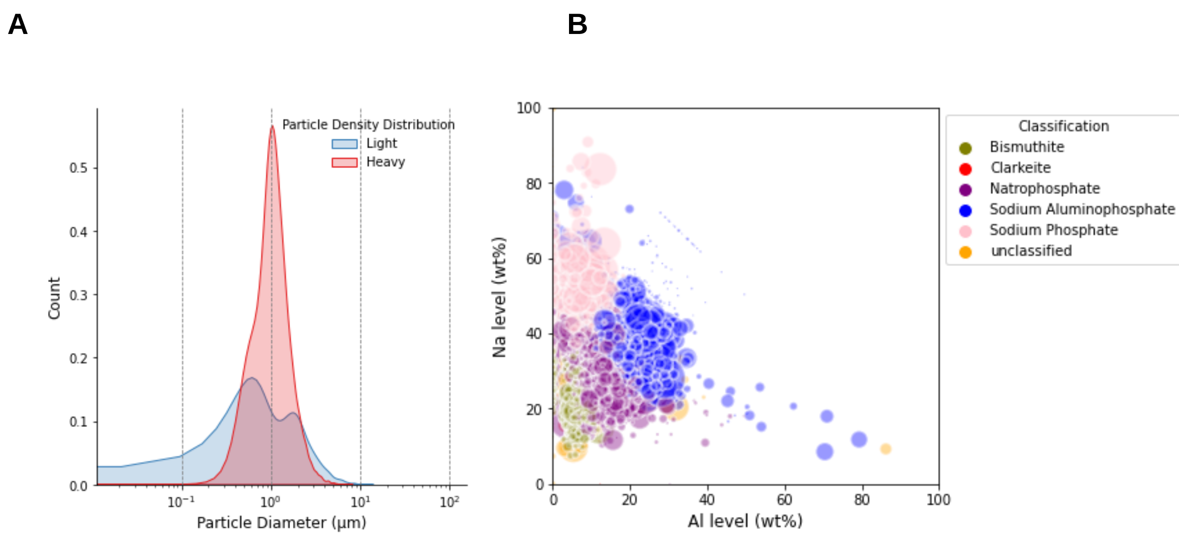

Figure 3.22 (A) Log-Normal plot of the two major gray-level regions. Region 1 consists of the high Z material and region 2 of lower Z materials which had on average a large particle size. (B) Bubble plot of Na vs. Al content with particle size (bubble diameter), and different colors representing the different phases

The particle size distributions of the individual phases are shown in Figure 3.23. The heavy or dense phases such as clarkeite have mean diameters that were less than a micrometer. In some instances, these particles were well isolated enabling a more detailed view of the individual phases. In Figure 3.24, SEM images and spectra of cancrinite, clarkeite, and natrophosphate are shown. Furthermore, a strontium phosphate phase was also found with a tetrahedron morphology similar to that observed by Reynolds and coworkers in AN-106 (Reynolds et al., 2020). It is unclear how common this phase was, but it also seemed to be associated with calcium and iron. The phase defined as clarkeite did not appear to contain sodium, and may be an oxide, possibly U_3O_8. However, for the purposes of this PSDD study, the phase was defined as 'clarkeite.' Gibbsite was not observed in this segment, and this is reflected in the bubble plot in Figure 3.22B where there were few phases with no high aluminum and low sodium, and in the PSD plots shown in Figure 3.23.

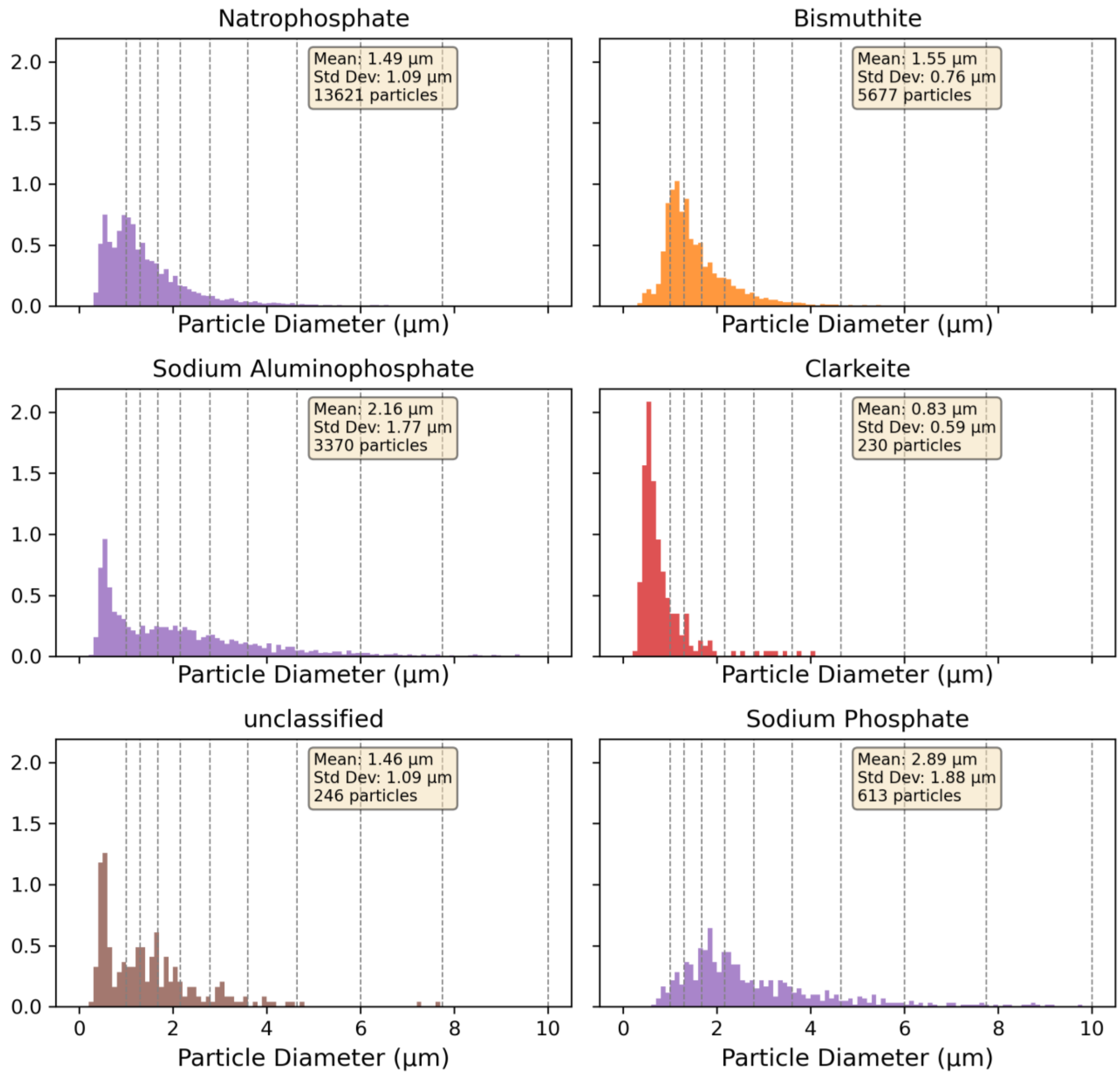

Figure 3.23 Histograms of the major phases found in AN-106-19UH with phosphate phases dominating the sludge sample. All phosphate particles have been colored purple to show their dominance in this sub-sample.

Close to 24,000 particles analyzed in this segment (AN-106-19UH).

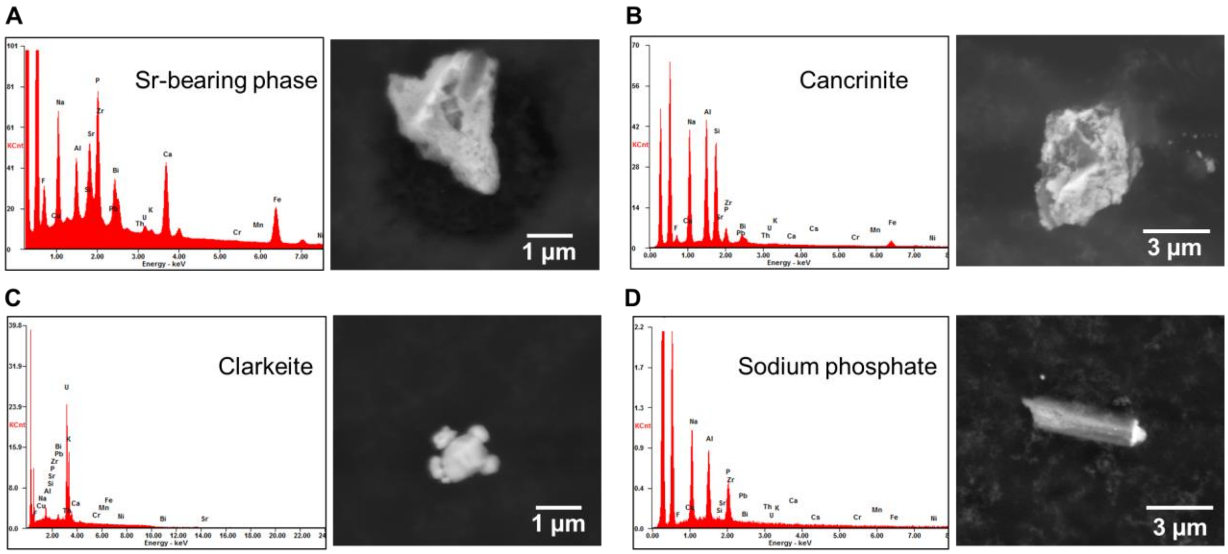

Figure 3.24 Major phases observed in AN-106-19UH including (A) a phase that contained Sr-P. Other phases included (B) Cancrinite, (C) Clarkeite, and (D) Sodium Phosphate.

The identification of the different sodium phosphate phases in Tank wastes is difficult to determine with electron microscopy. However, the differences can be readily seen with PLM with natrophosphate exhibiting low birefringence and sodium phosphate showing high birefringence (Herting et al., 2015; Herting & Reynolds, 2016). With SEM-EDS, the major difference is the presence of fluorine in natrophosphate. The fluorine F-K x-ray line is weak and strongly absorbed by oxygen which makes its detection difficult.

3.5 AN-106-21UH (21366)

The match between the bulk chemical analysis breakdown and the analysis based on SEM particle area was poor for segment AN-106-21UH where gibbsite was identified as the major phase (see Figure 3.25A). Although gibbsite was reported in the SEM analysis, a sodium aluminate was also found (see Figure 3.25B). 'BiPO4' and 'FeOOH' were reported based on the bulk chemical analysis; whereas from the SEM work, there is a mixed U-Fe-P phase (see Figure 3.26 and Figure 3.27).

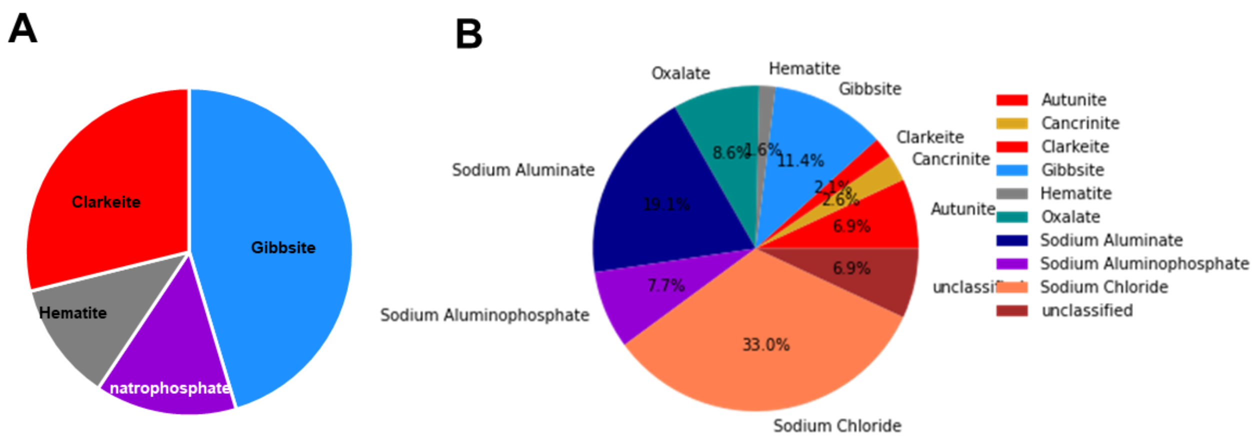

Figure 3.25 Estimated solids composition from AN-106-21UH from (A) bulk chemical analysis and (B) SEM-APA data.

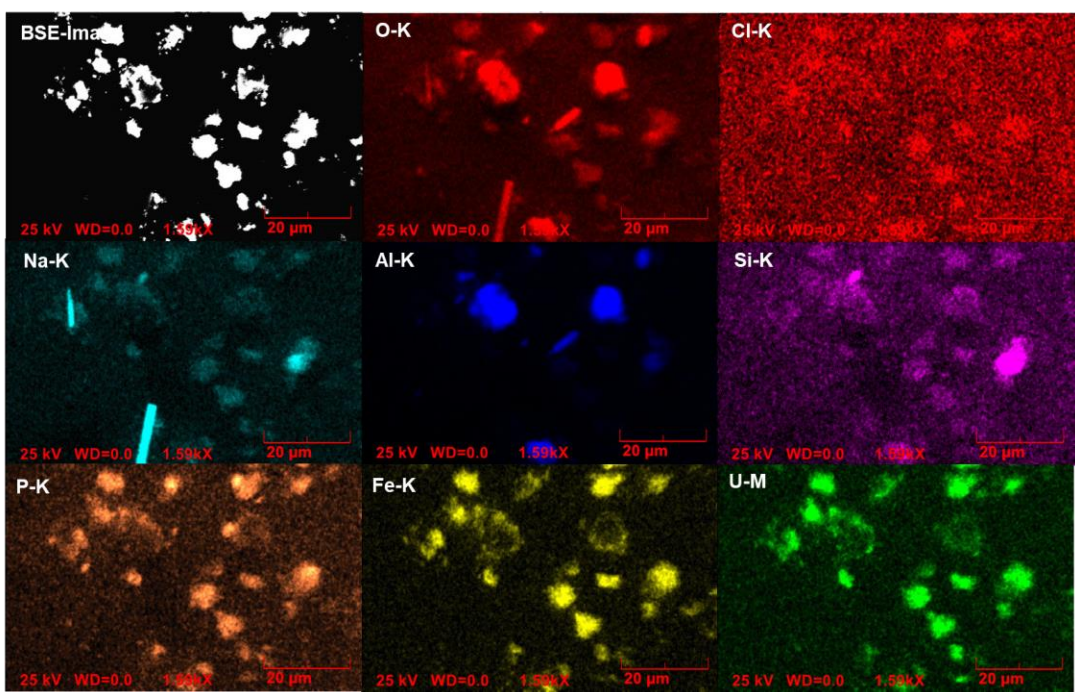

Figure 3.26 SEM-EDS Elemental map of AN-106-21UH showing the dominance of Al-rich phases and particles containing U, Fe, and P.

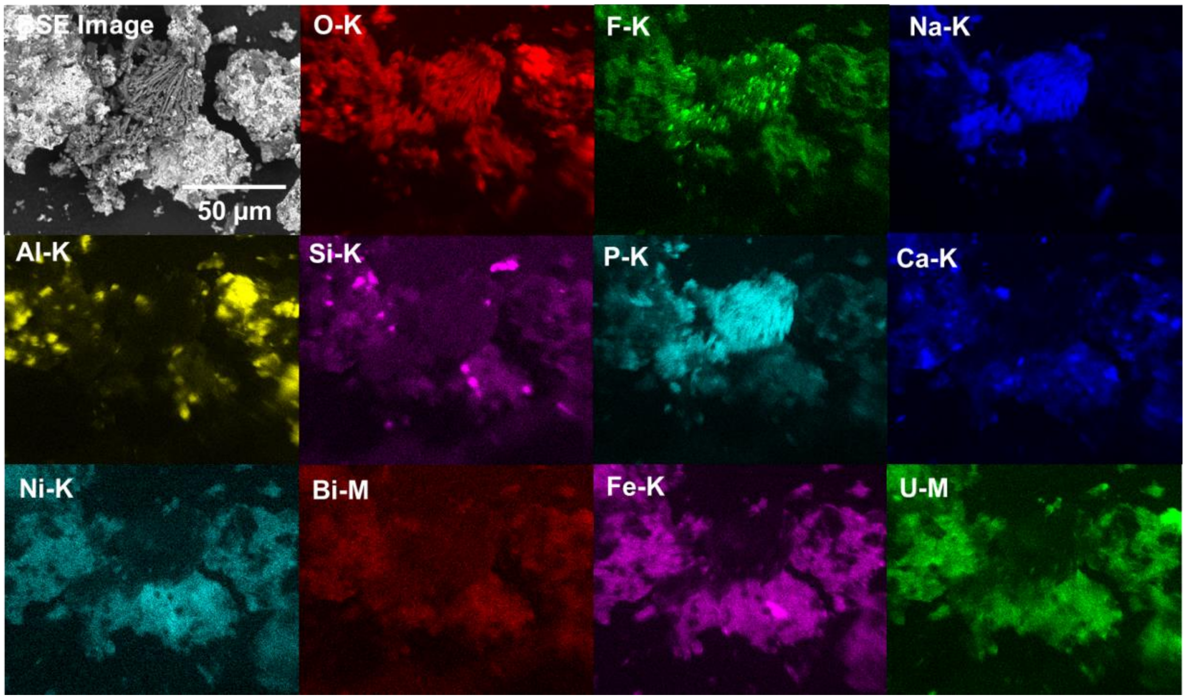

Figure 3.27 SEM-EDS Elemental map of AN-106-21UH showing a phosphate agglomerate surrounded by several other types of phases.

The ternary diagrams in Figure 3.28, show the presence of an aluminum-rich phase, and shows the distribution of uranium, iron, and phosphorus, indicating a strong cluster of particles with similar compositions. In Figure 3.29A, the log-normal plot shows the distribution of heavy and light phases, and the bubble plot (see Figure 3.29B) shows the distribution of aluminum and sodium.

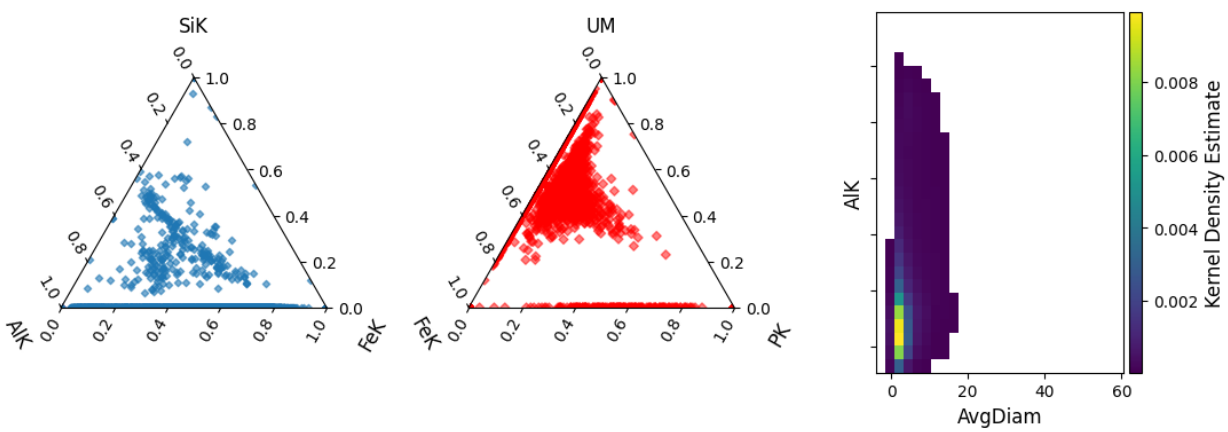

Figure 3.28 Ternary plots for Si-Al-Fe, and U-P-Fe, and a third plot showing Al concentration with particle size.

There was also a suggestion from the SEM analysis that two types of uranium phases were present. One contained sodium and was defined as clarkeite, and the other appeared to contain phosphorus, and was defined as autunite. The particle size distributions for each of the phases is shown in Figure 3.30. Both uranium-bearing phases, clarkeite and autunite, have been colored red.

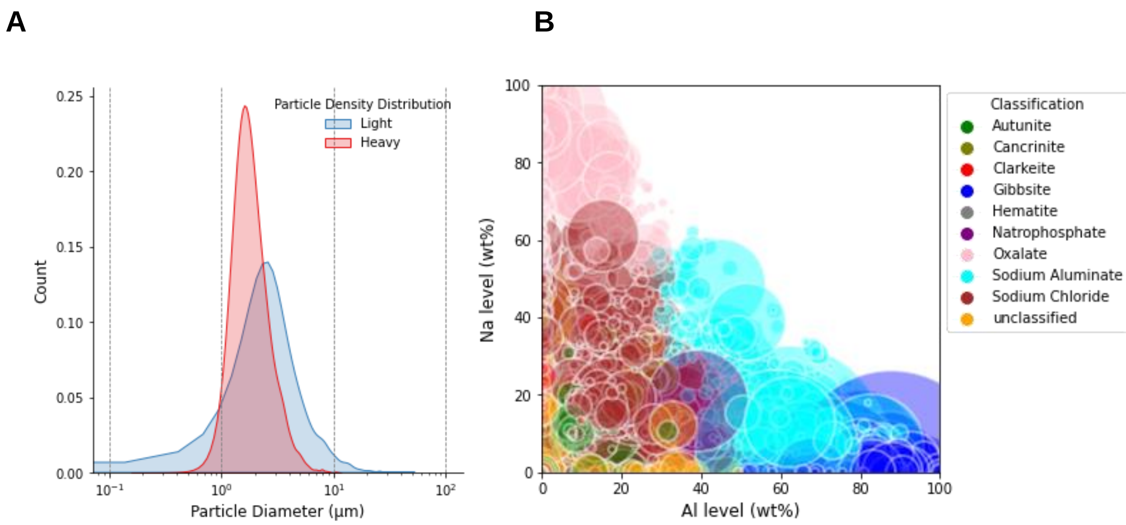

Figure 3.29 (A) Log-Normal plot of the two major gray-level regions. Region 1 consists of the high Z material and region 2 of lower Z materials which had on average a large particle size. (B) Bubble plot of Na vs. Al content with particle size (bubble diameter), and different colors representing the different phases.

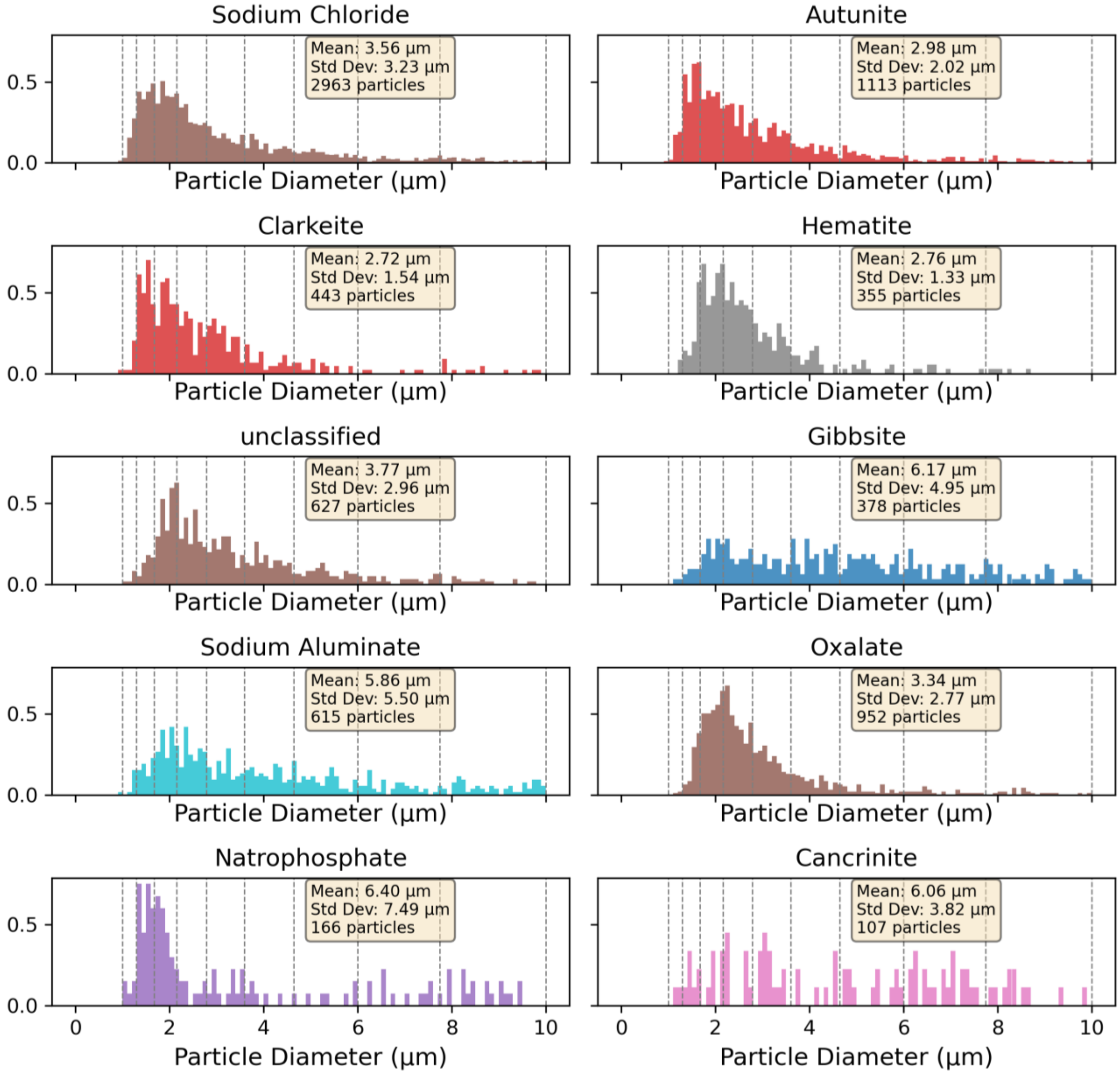

Figure 3.30 Histograms of the major phases found in AN-106-21UH with phosphate phases dominating the sludge sample.

3.6 AN-106-22UH (21367)

The match between the bulk chemical analysis breakdown and the analysis based on SEM particle area was also poor for segment AN-106-22UH where gibbsite like in AN-106 21UH was identified as the major phase (see Figure 3.31A). Small amounts of gibbsite were reported in the SEM analysis, the major phase reported as defined as 'oxalate' which was essentially a sodium phase (see Figure 3.31B). To aid in the identification of compositions, both carbon and oxygen, common to every particle, were ignored. This enabled more accurate quantification. Both 'NFPO4' and a significant amount of 'FeOOH' were reported based on the bulk chemical analysis. From the SEM work, there was a hematite phase and clarkeite, in agreement with the bulk chemistry analyses (see Figure 3.32).

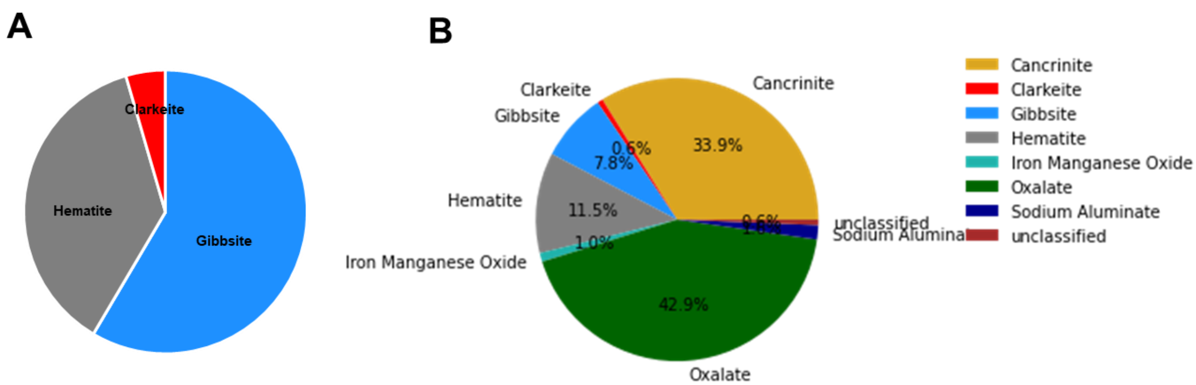

Figure 3.31 (A) Estimated composition of segment AN-106-22UH with expected increase in gibbsite but significant iron oxide present and (B) sludge composition based on the SEM data.

The elemental maps clearly show the occurrence of phosphate phases however, these are more difficult to track during the SEM analysis owing to their large particle sizes and morphologies.

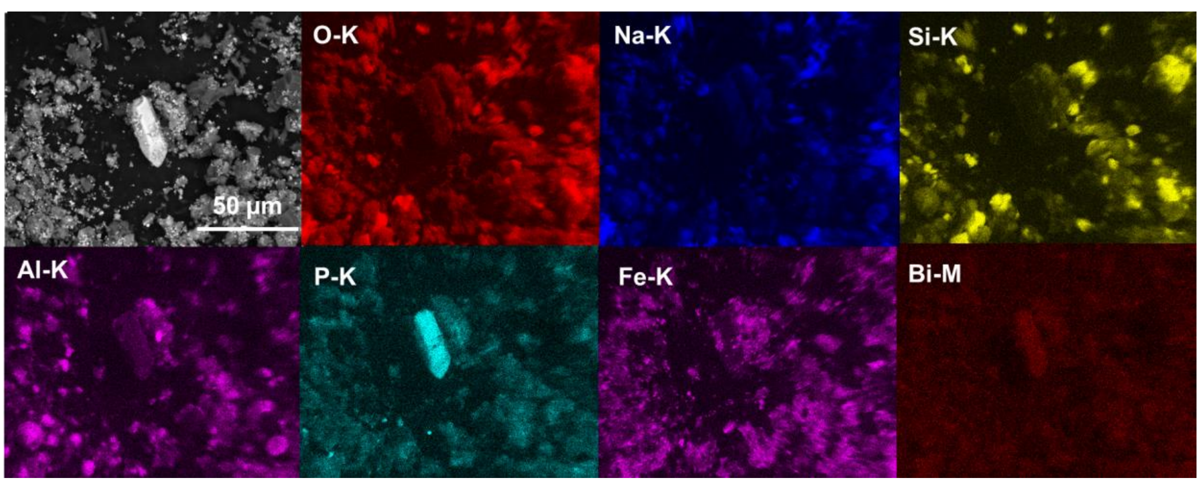

Figure 3.32 SEM-EDS Elemental map of AN-106-22UH showing the dominance of Al-rich phases and Fe-bearing phases.

The ternary diagrams in Figure 3.33, show little Al-bearing phases, but the hematite is clearly present. In Figure 3.34A, the log-normal plot shows the distribution of heavy and light phases, and the bubble plot (see Figure 3.34B) shows the distribution of aluminum and sodium. Gibbsite is the major aluminum-rich phase. The particle size distribution of all individual phases is shown in Figure 3.35.

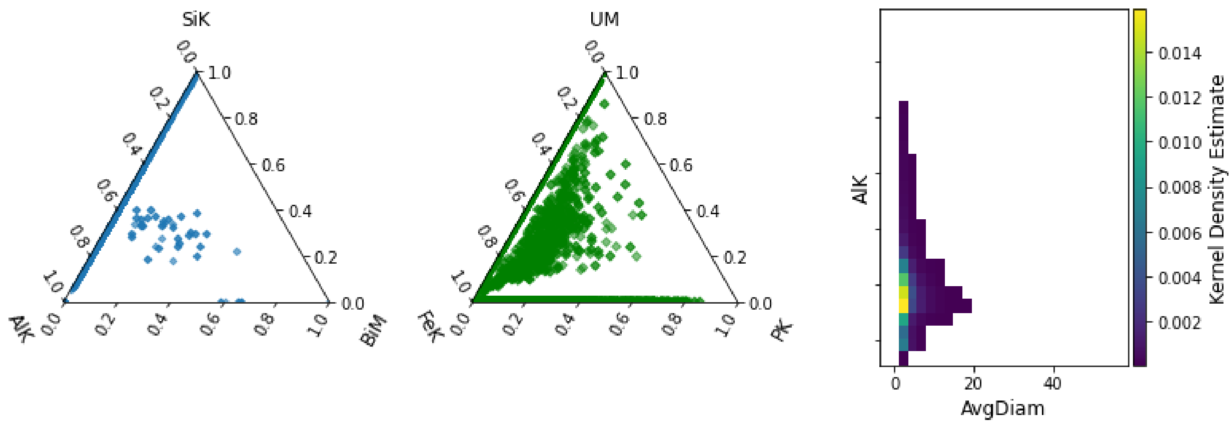

Figure 3.33 Ternary plots for Si-Al-Fe, and U-P-Fe, and a third plot showing Al concentration with particle size.

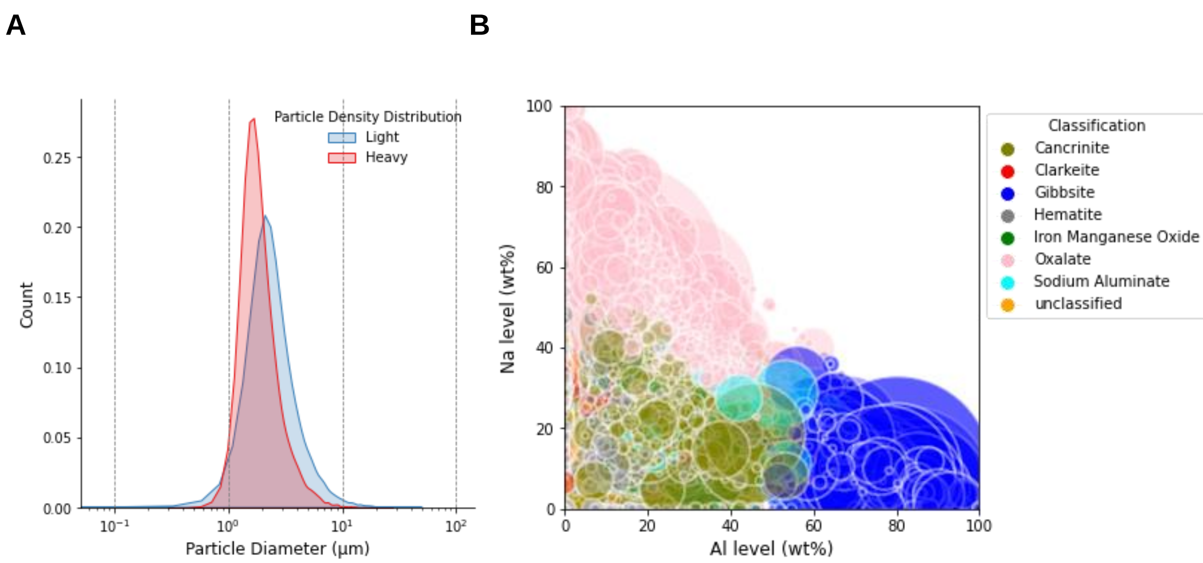

Figure 3.34 (A) Log-Normal plot of the two major gray-level regions. Region 1 consists of the high Z material and region 2 of lower Z materials which had on average a large particle size. (B) Bubble plot of Na vs. Al content with particle size (bubble diameter), and different colors representing the different phases.

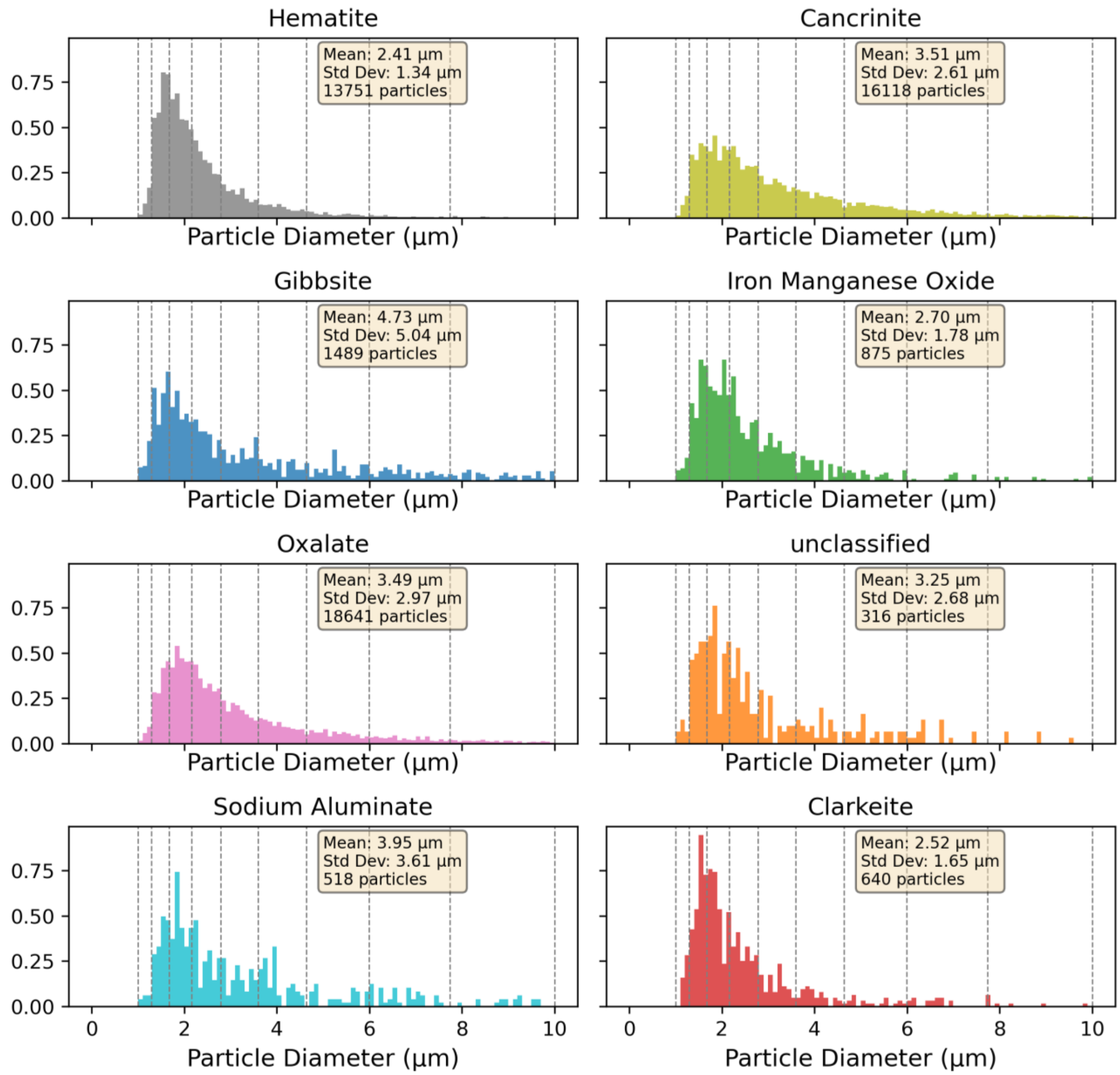

Figure 3.35 Histograms of the major phases found in AN-106-22UH with phosphate phases dominating the sludge sample.

3.7 Conclusion to AN-106 APA

The heavy or high Z containing phases in the AN-106 series were <3 µm in diameter. The lighter phases were slightly large. It was likely that the phosphate particle sizes were underestimated. A summary of the results in shown in Table 3.1.

Table 3.1 List of AN-106 segments with major particles including average diameter and number of particles analyzed

Segment Identification	Major Phases	Gibbsite	Clarkeite	Fe-Rich	Bi-bearing
		Average particle diameter (equivalent) and the total number of particles reported in brackets.			
14	aluminate, clarkeite,	4.22 ± 4.89 µm (3322)	3.15 ± 2.05 µm (329)	2.68 ± 1.60 µm (1558)	--
16 LH	aluminate (gibbsite), hematite, U-Fe-Bi, cancrinite, phosphate	4.30 ± 3.49 µm (1307)	--	2.58 ± 1.60 µm (11049)	2.47 ± 1.53 µm (1263)
19 LH	Fe-Bi, phosphate	--	3.39 ± 2.68 µm (876)	--	3.74 ± 3.59 µm (2663)
19 UH	bismuthite, phosphate	--	0.83 ± 0.59 µm (230)	--	1.55 ± 0.76 µm (5677)
21 UH	clarkeite, hematite, phosphate	6.17 ± 4.95 µm (378)	2.72 ± 1.54 µm (443)	2.76 ± 1.33 µm (355)	--
22 UH	cancrinite, hematite, gibbsite	4.73 ± 5.04 µm (1489)	2.52 ± 1.65 µm (640)	2.41 ± 1.34 µm (13751)	--

4.0 AN-101 Solids

AN-101 was the receiver tank for retrieval of several C-Farms waste tanks, including Tanks 241-C-102 and 241-C-111 (Kraft & Meznarich, 2017).

4.1 AN-101 21415 (18LH)

AN-101- segment 21415 (18LH) was almost entirely gibbsite. The pie diagram in Figure 4.1 shows that nearly 97% of the particles were gibbsite. Phosphate was identified from bulk chemical analysis; however, no phosphate phases were observed during the SEM-APA. Elemental maps confirmed the dominance of gibbsite with only aluminum and oxygen being observed (see Figure 4.2). However, an unusual thorium oxide was observed. This is an example of operator bias, as this specific phase had an interesting morphology, but it does not represent that types of phases that were observed in the sample (see Figure 4.2). There were very few other thorium-bearing particles observed in this sample. The thorium particles appeared angular and were most likely from thoria processing wastes that were known to have been introduced into the AN-101 tanks. The thorium particle in Figure 4.2 was approximately 40 µm × 40 µm and 10 µm thick.

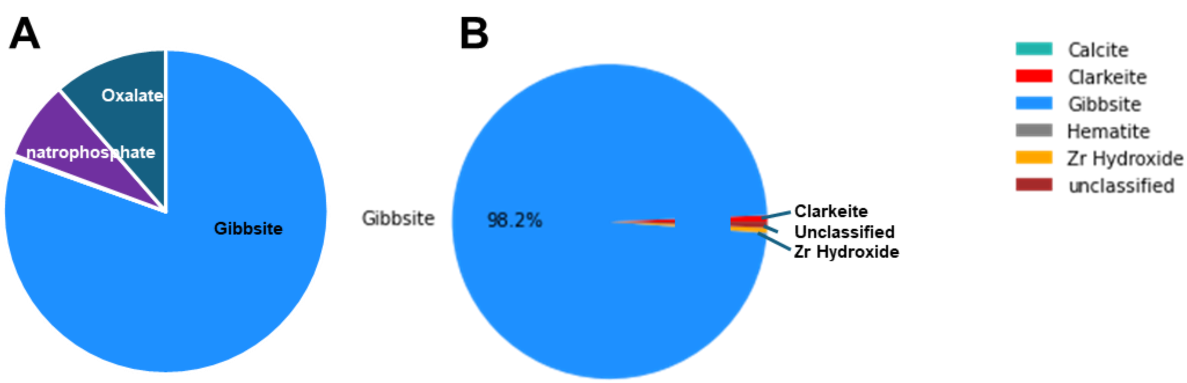

Figure 4.1 Estimated composition of segment AN-101-21415 with expected increase in gibbsite but significant iron oxide present.

The ternary diagrams in Figure 4.3 show very few other elements besides aluminum. The particles containing aluminum had particle diameters extending out to 20 µm, although most particles were far smaller at <4 µm. This BSE contrast plot showed two major contrast regions (see Figure 4.4A). The bubble plot that shows the relative size of particles, the major phases, and the aluminum and sodium content, shows the dominance of gibbsite in this specimen (see Figure 4.4B).

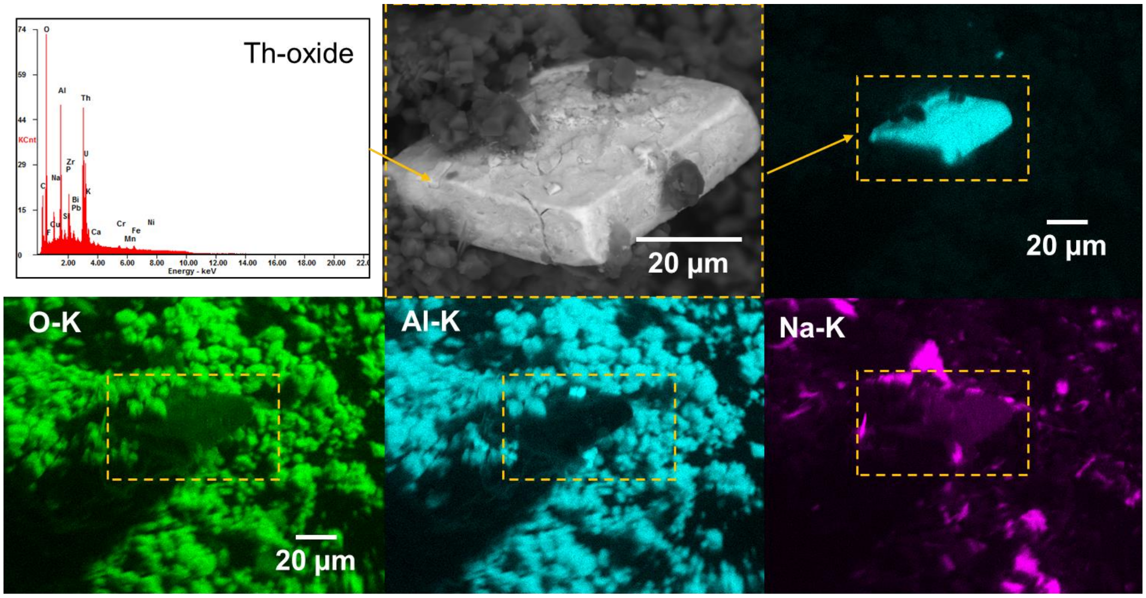

Figure 4.2 SEM-EDS Elemental map of AN-101-21415 showing the dominance of Al-rich phases surrounding a thorium oxide plate.

In Figure 4.5, we can see several gibbsite particles that exceed 10 µm. This may point to problems with image segmentation that can underestimate particles; however, this effect is caused by particle deposition during sample preparation. Large particles deposit on the carbon substrate quickly and result in pile-up that does not provide good regions for automated particle segmentation and analysis. Therefore, the APA analyses can only be obtained in regions with well-dispersed particles, and these may be biased by the smaller particles. The particle size distributions for the different phases based on the SEM-APA found in AN-101-21415 are shown in Figure 4.6. The majority (~98%) of particles were gibbsite with an average particle diameter of 3.8 µm obtained by the segmentation routines. Given that the gibbsite distribution is log-normal, this would imply that only 0.1% of the gibbsite particles would be over 10 µm. This is most likely an underestimate owning to issues with preparing the samples for SEM analysis. Improvements in sample preparation are needed to obtain better particle size distributions and more representative data.

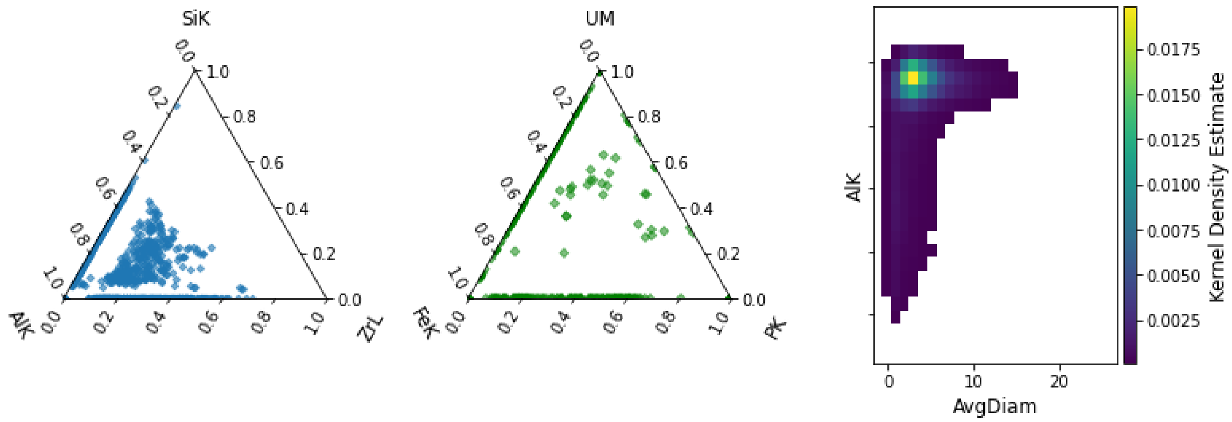

Figure 4.3 Ternary plots for Si-Al-Fe, and U-P-Fe, and a third plot showing Al concentration with particle size.

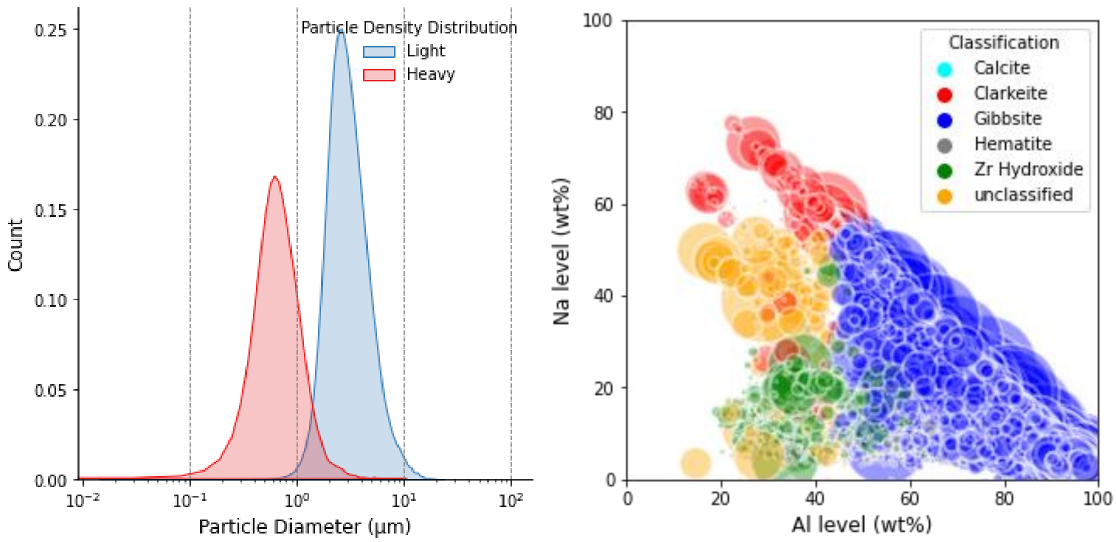

Figure 4.4 (A) Log-normal plot of the two major gray-level regions. Region 1 consists of the high Z material, region 2 consists of the show lighter Z fraction which had on average a large particle size and (B) Bubble plot of Na vs. Al content with particle size (bubble diameter), and different colors representing the different phases.

Over 28,000 particles were analyzed in these SEM mounts.

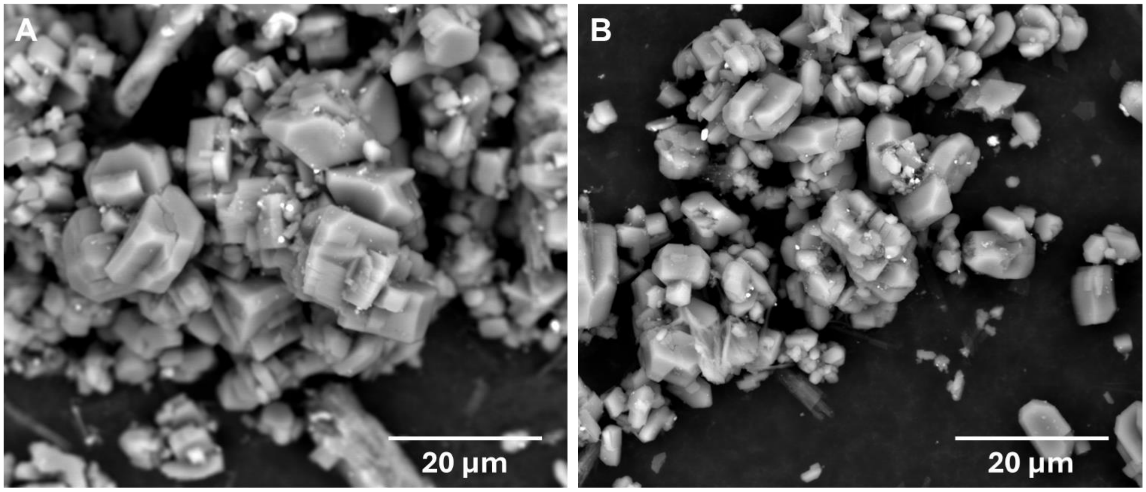

Figure 4.5 SEM images of gibbsite from AN-101-21415 showing particles more than 10 µm in diameter

Another example of a large gibbsite particle is shown in Figure 4.7A. The particle has cracks running perpendicular to the longest axis that may be due to drying under vacuum. Below this image in Figure 4.7B, an unusual structure with a fan-like morphology is shown. The aggregate consists of sodium aluminate ‘blades’ with interspersed Zr-rich particles. Similar ‘fan’ like aggregates have been observed by Herting and coworkers in the DST 241-AP-101 (see Figure 2.12.5 - S08R000138c (107), pg.52) in the Particle Atlas report (Herting et al., 2015). These were not common within the samples analyzed.

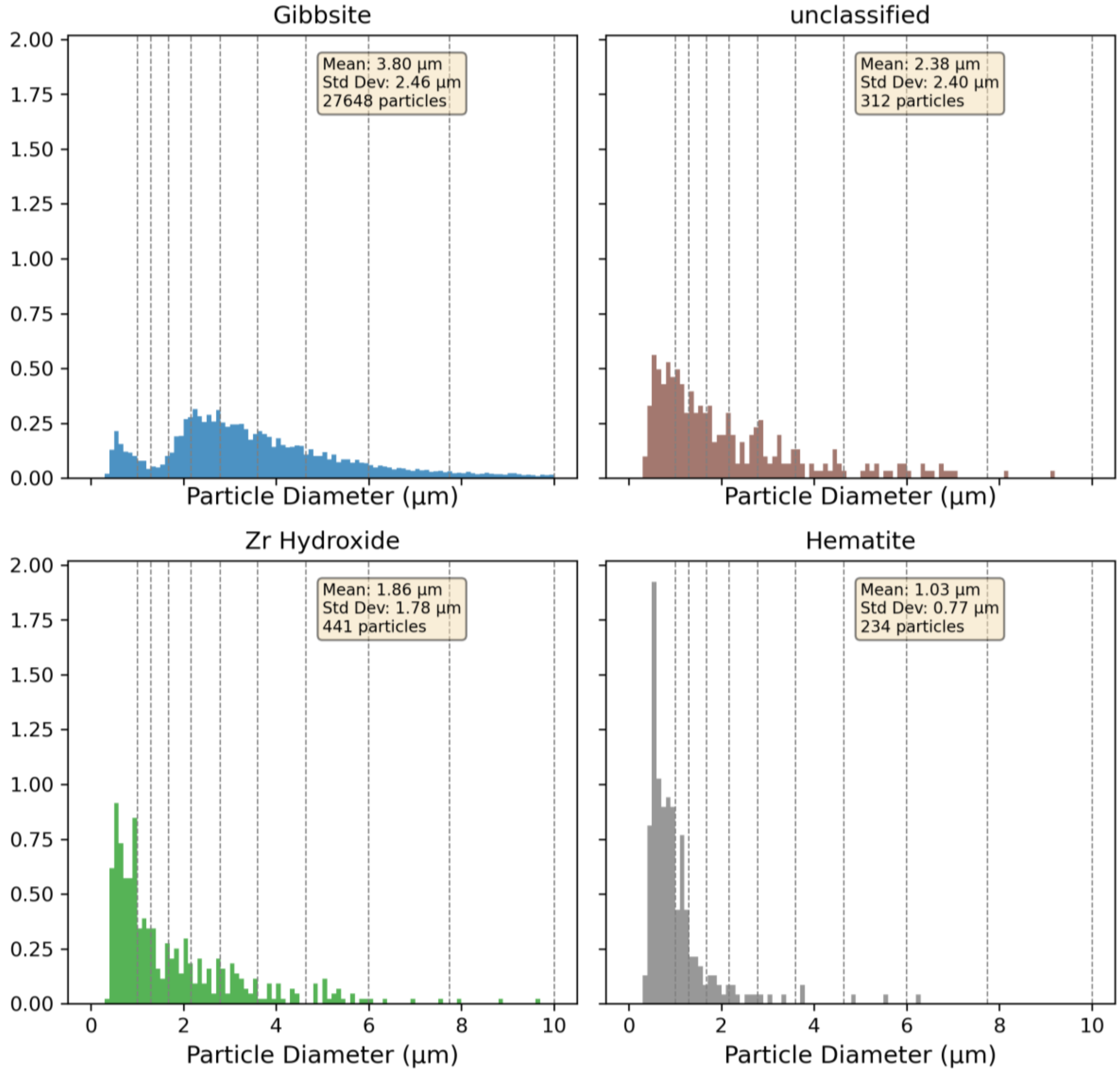

Figure 4.6 Normalized distribution of particle sizes for the major phase categories including mean and standard deviation values in 18LH.

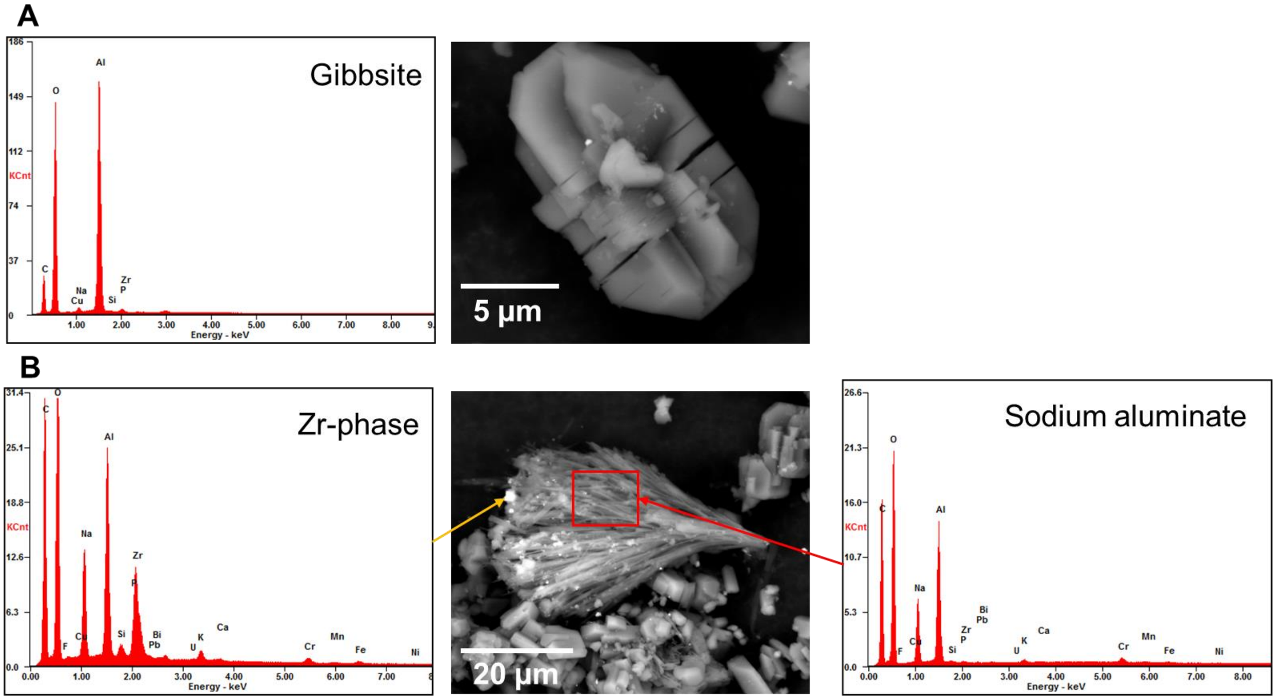

Figure 4.7 SEM-EDS analysis of individual particles within the AN-101 sludge. (A) Gibbsite, and (B) a fibrous sodium aluminate phase with attached Zr-bearing particles.

4.2 AN-101-21407 (14UH)

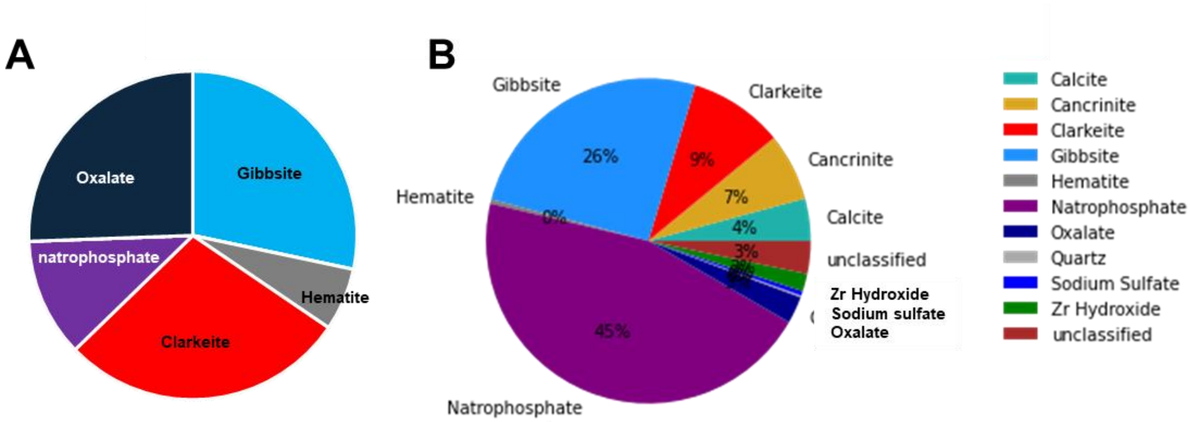

Figure 4.8 Estimated composition of segment AN-101-21417 with expected increase in gibbsite but significant iron oxide present.

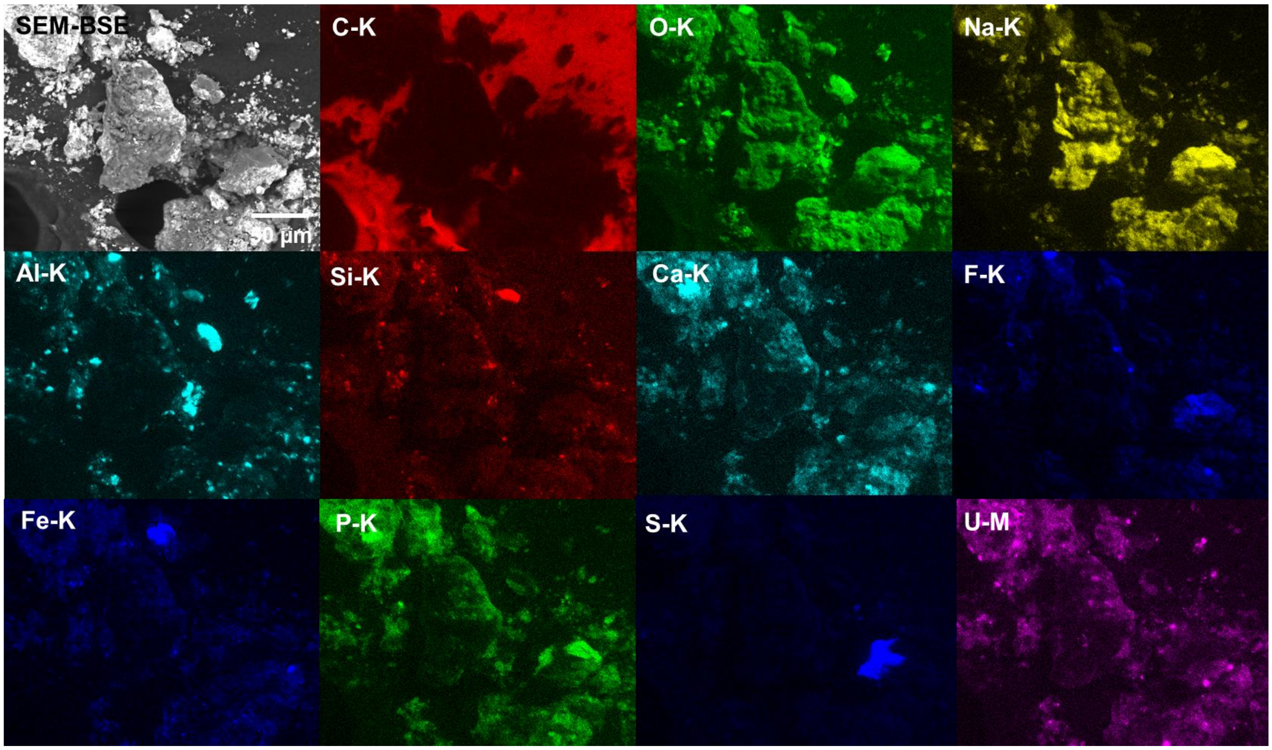

Figure 4.9 SEM-EDS Elemental map of AN-101-21417 showing the dominance of Al-rich phases and Fe-bearing phases.

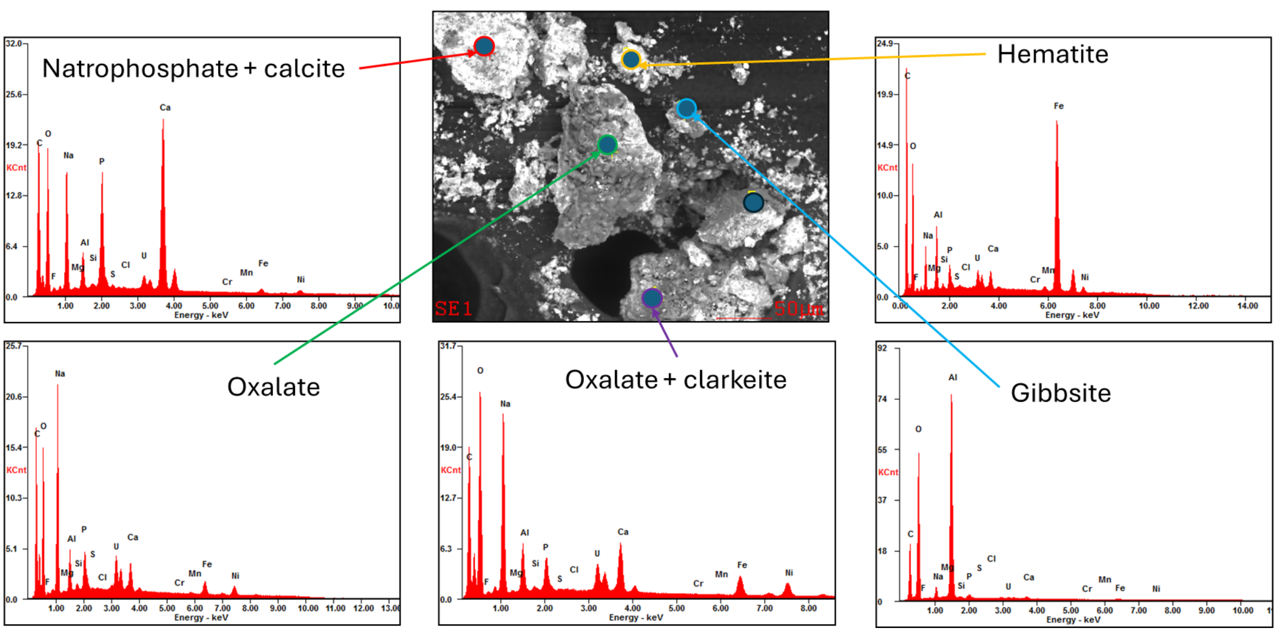

Figure 4.10 SEM-EDS analysis of individual particles within the AN-101 showing the heterogeneous nature of the large particles.

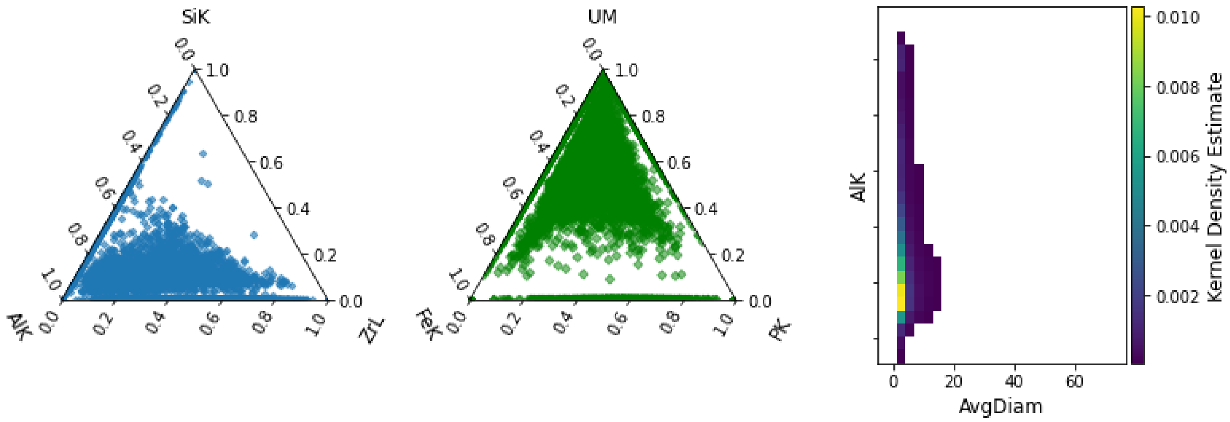

Figure 4.11 Ternary plots for Si-Al-Fe, and U-P-Fe, and a third plot showing Al concentration with particle size.

The plots below show some of the ways that APA data can be displayed. Because heavy (or high Z) particles are brighter, we can separate out particle sizes based on contrast. The high Z particles tend to be smaller and often attached to the larger lower Z particles. The plot has a log-normal distribution for all the particle types. The second plot which is a bubble plot shows the distribution of two elements with particle size and assigned phase. It shows that most of the aluminum is associated with gibbsite, as might be expected. This type of plot enables us to visualize four variables on a single plot (sodium and aluminum content, particle size, and phase).

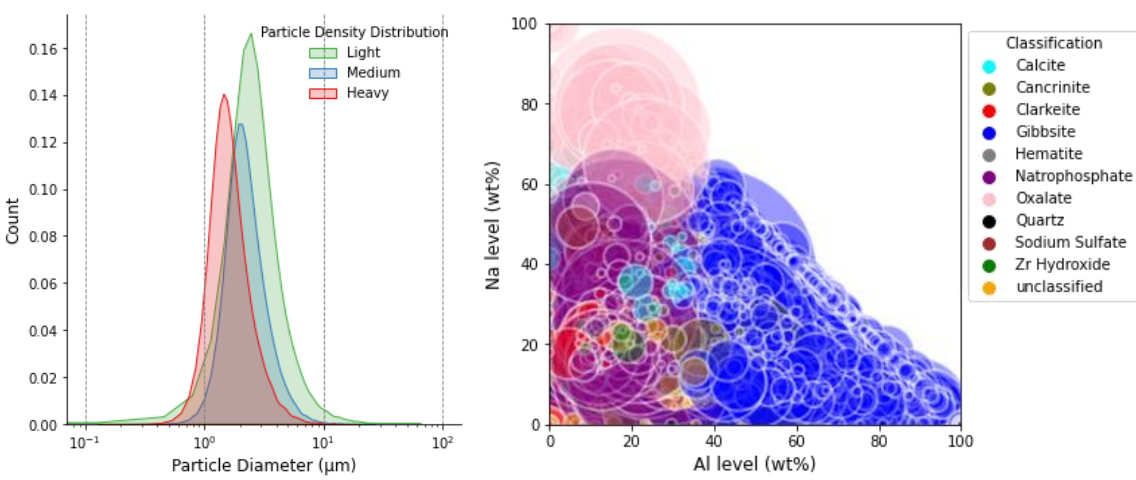

Figure 4.12 (A) Log-normal plot of the three major gray-level regions. Region 1 consists of the high Z material, region 2 consists of the medium fraction, and region 3 of lighter Z fraction which had on average a large particle size and (B) Bubble plot of Na vs. Al content with particle size (bubble diameter), and different colors representing the different phases.

Plots showing the application of APA methods to examine the nature of an AN-101 segment. In this case, over 45,000 particles were analyzed with the SEM-EDS providing composition and morphology for each particle. However, there were regions of the sample that contained large agglomerates (see Figure 4.13). It is unclear if these large particles are the true particles of concern. To perform APA, we needed to break down these types of fragments or agglomerates. The fragments were made up of multiple phases, hence, they represent dozens of phases and particle types.

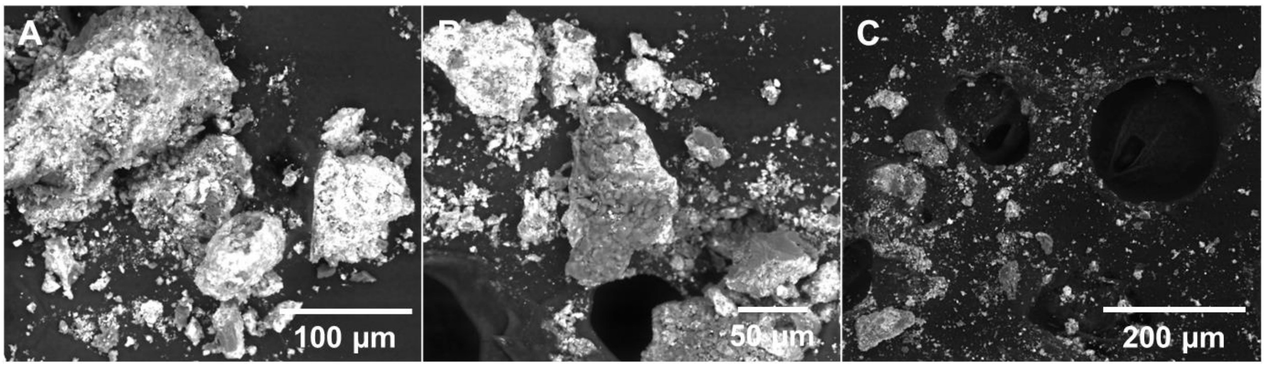

Figure 4.13 SEM images of large agglomerates in AN-101-21407 that could not be analyzed with APA

PLM has been used extensively by Herting and coworkers (Herting et al., 2015). Indeed, this reference is an excellent resource for identifying phases in the Hanford wastes. In Figure 4.14, PLM images obtained with cross-polars and with an ¼ waveplate to highlight high birefringent particles. In Figure 4.14A and B, show large agglomerates that are greater than 100 µm in diameter. The bright specs in the image are individual crystallites and are significantly smaller. Likewise, in Figure 4.14C and D, the interference plate enables the individual crystals to be seen clearly and most of these are <10 µm in size.

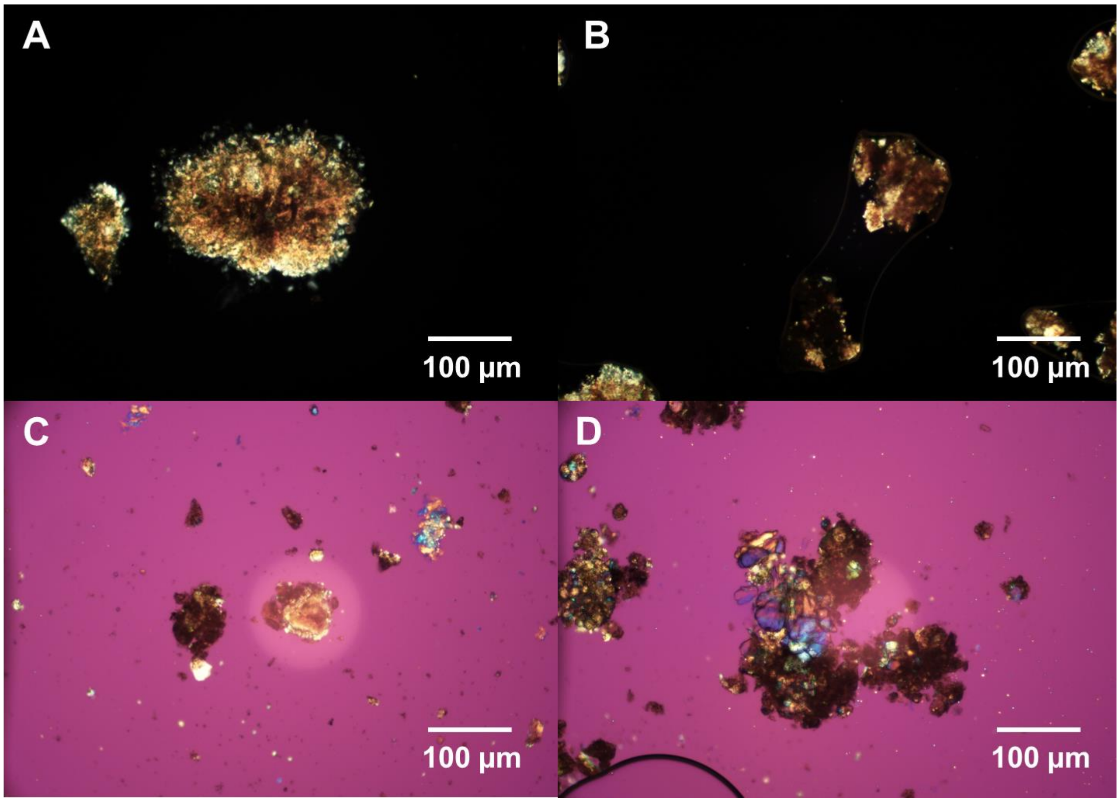

Figure 4.14 PLM images of AN-101-21407 showing large agglomerates (A and B) Cross-Polar images, and (C and D) Cross-polar with ¼ waveplate.

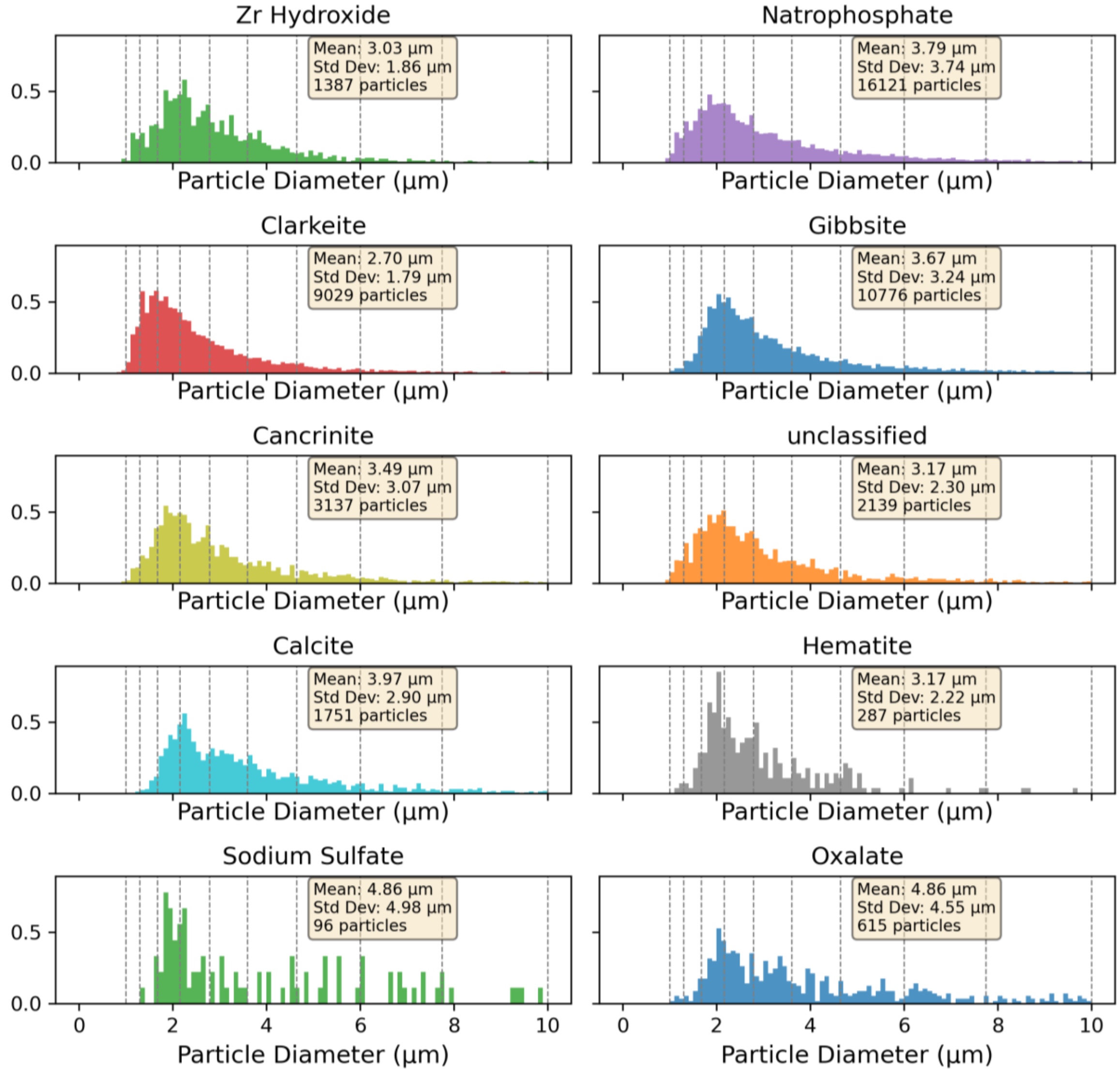

Figure 4.15 Normalized distribution of particle sizes for specific phase categories including mean and standard deviation values from 14UH

4.3 AN-101-21417 (19LH)

AN-101-21417 (19LH) had large phosphate particles that were not easily identified with APA. The SEM analysis of the sample did indicate that a sodium sulfur-bearing phase was common in the sample. The pie diagram shown in Figure 4.16 shows oxalate, natrophosphate and clarkeite as common phases, but also sodium sulfate. A major sodium sulfate phase identified in 241-AP-107 wastes was determined to be kogarkoite [Na_3SO4F] (Bolling et al., 2019). Inspection of the elemental maps confirms the occurrence of a sodium sulfate phase (see Figure 4.17) and that this phase was commonly observed in the sample. As well as sulfate, there were large silica particles in the sample (see Figure 4.18).

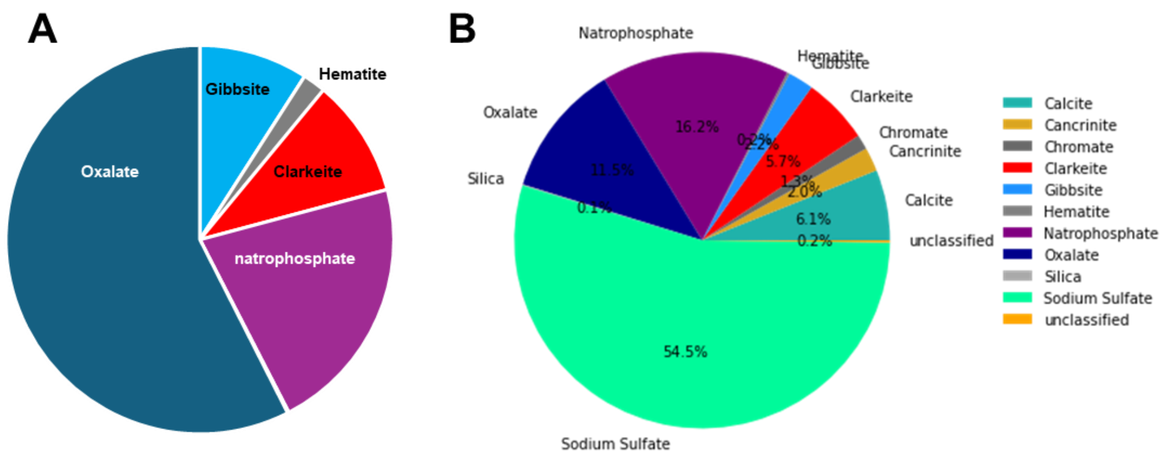

Figure 4.16 Estimated composition of segment AN-101-21417 with expected increase in gibbsite but significant iron oxide present.

The ternary diagrams in Figure 4.19 using the same elements that were applied to other samples groups, did not indicate significant aluminum-phases in the sample.

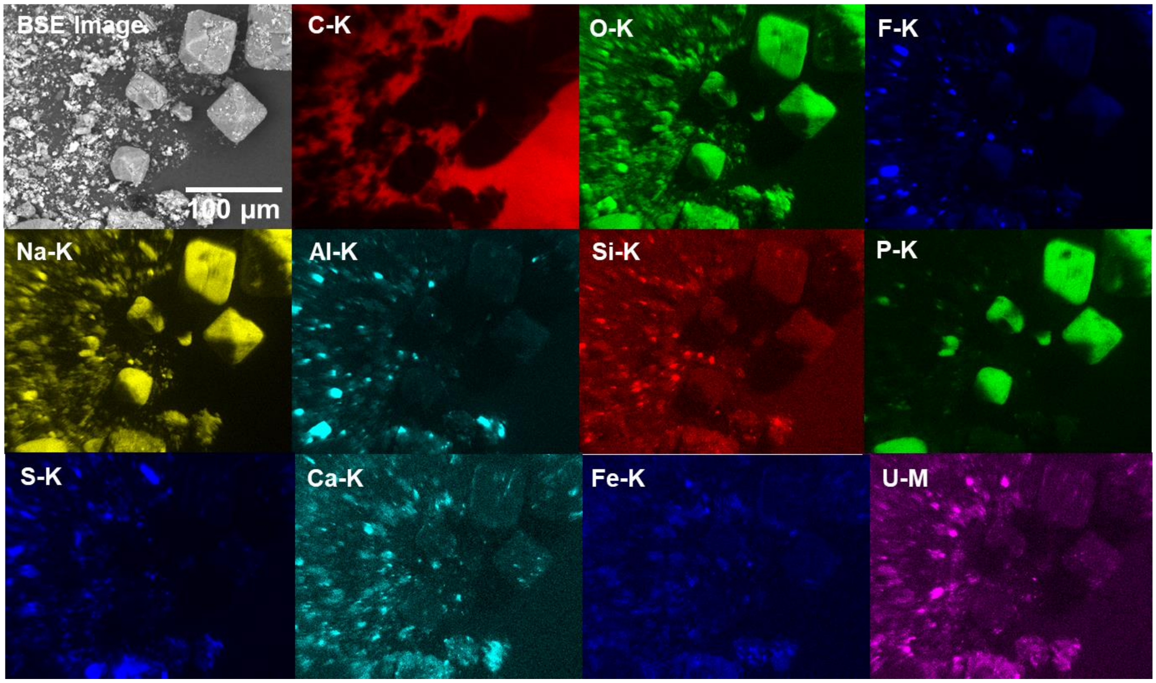

Figure 4.17 SEM-EDS Elemental map of AN-101-21417 showing the dominance of large phosphate particles. Sodium sulfate particles were also common.

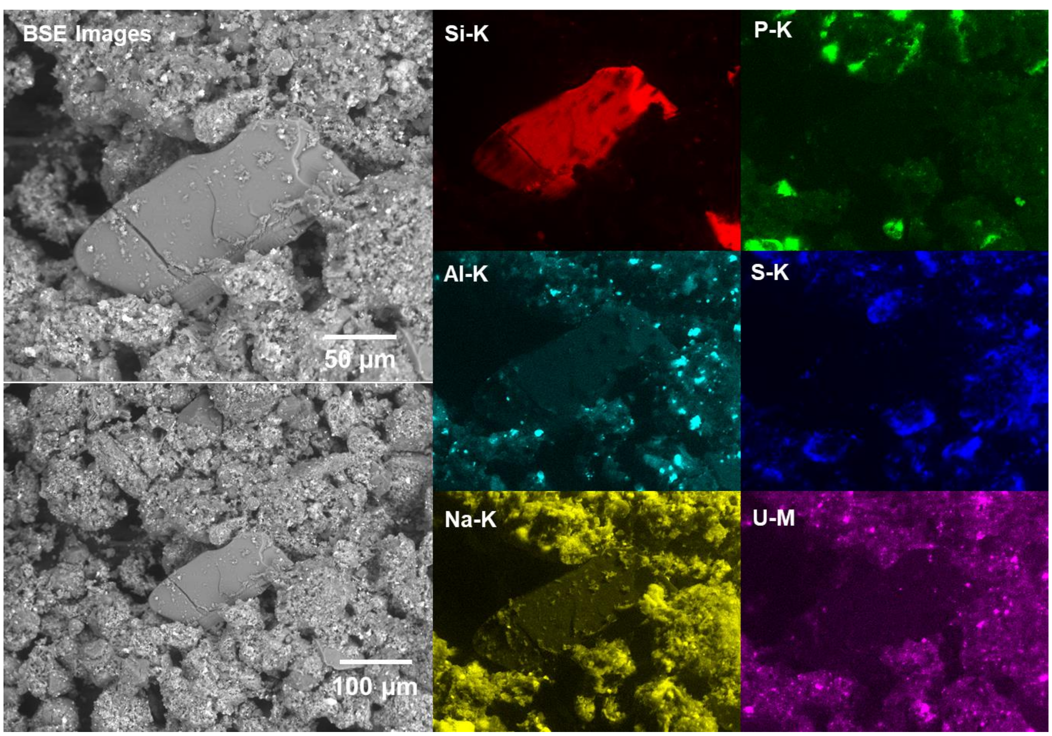

Figure 4.18 SEM-EDS Elemental map of AN-101-21417 showing a large silica particle surrounded by sulfate and a few Al- and P- particles.

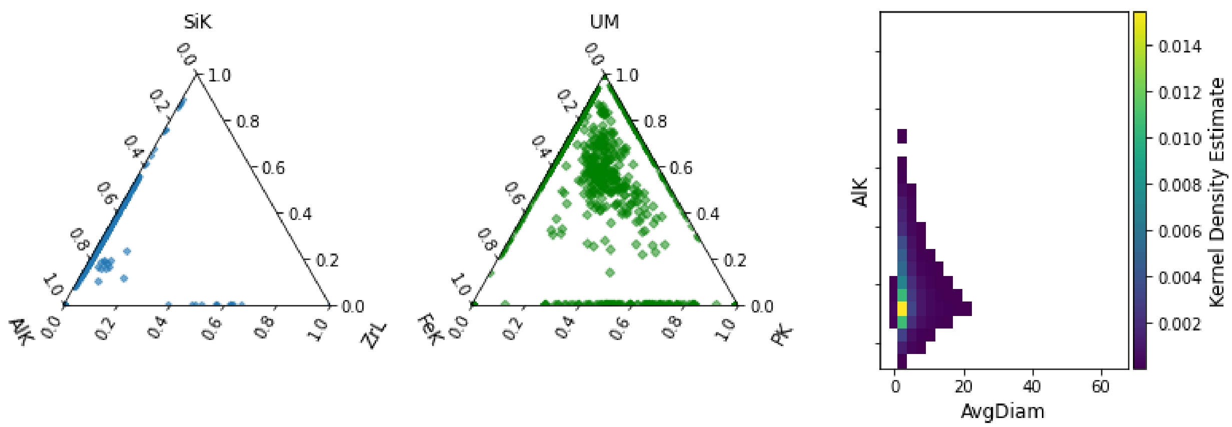

Figure 4.19 Ternary plots for Si-Al-Fe, and U-P-Fe, and a third plot showing Al concentration with particle size.

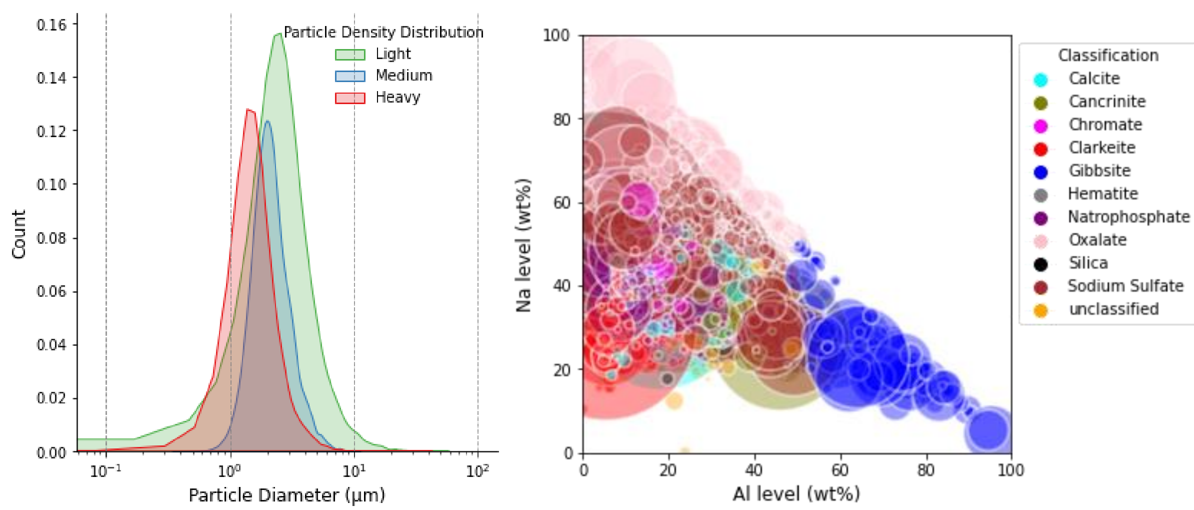

Figure 4.20 (A) Log-normal plot of the three major gray-level regions. Region 1 consists of the high Z material, region 2 consists of the medium fraction, and region 3 of lighter Z fraction which had on average a large particle size and (B) Bubble plot of Na vs. Al content with particle size (bubble diameter), and different colors representing the different phases.

Figure 4.21 shows a series of SEM images of large bipyramid particles. Based on SEM-EDS elemental mapping (see Figure 4.17), these are sodium phosphate particles. Similar bipyramidal particles of phosphate were identified by Bolling and coworkers in Hanford tank 241-AP-107 which they identified as natrophosphate (Bolling et al., 2019). With the natrophosphate they also identified a needle-like particle, kogarkoite, a sodium sulfate phase. There were also particles of higher Z material (bright specs under BSE imaging) on the surface of these particles. The large bipyramid particles were found concentrated at one point on the SEM stub suggesting that they had fallen out of solution together. Furthermore, APA analysis was unable to image these particles as they were too large compared to the rest of the sample. The particles clearly exceeded 50 µm in diameter. The problem of uneven dispersion of particles during the preparation of the SEM mounts was resolved by endeavoring to analyzing the entire mount instead of limiting the analysis to a smaller region. In Figure 4.22, PLM images of the AN-101 19LH sample are shown.

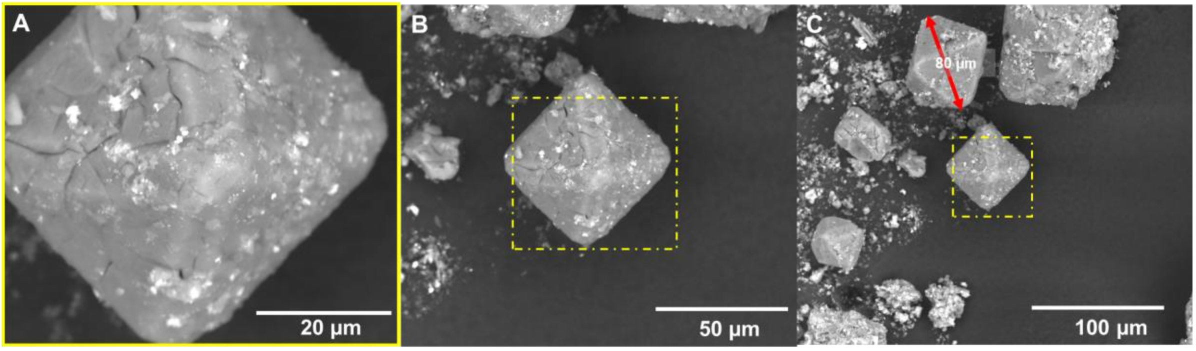

Figure 4.21 SEM images of phosphate particles in AN-101-21417 that exceed 50 µm in diameter

There was no clear evidence of needle-like sulfate phases however, the elemental maps did support the occurrence of a mixed Na-S-F phase.

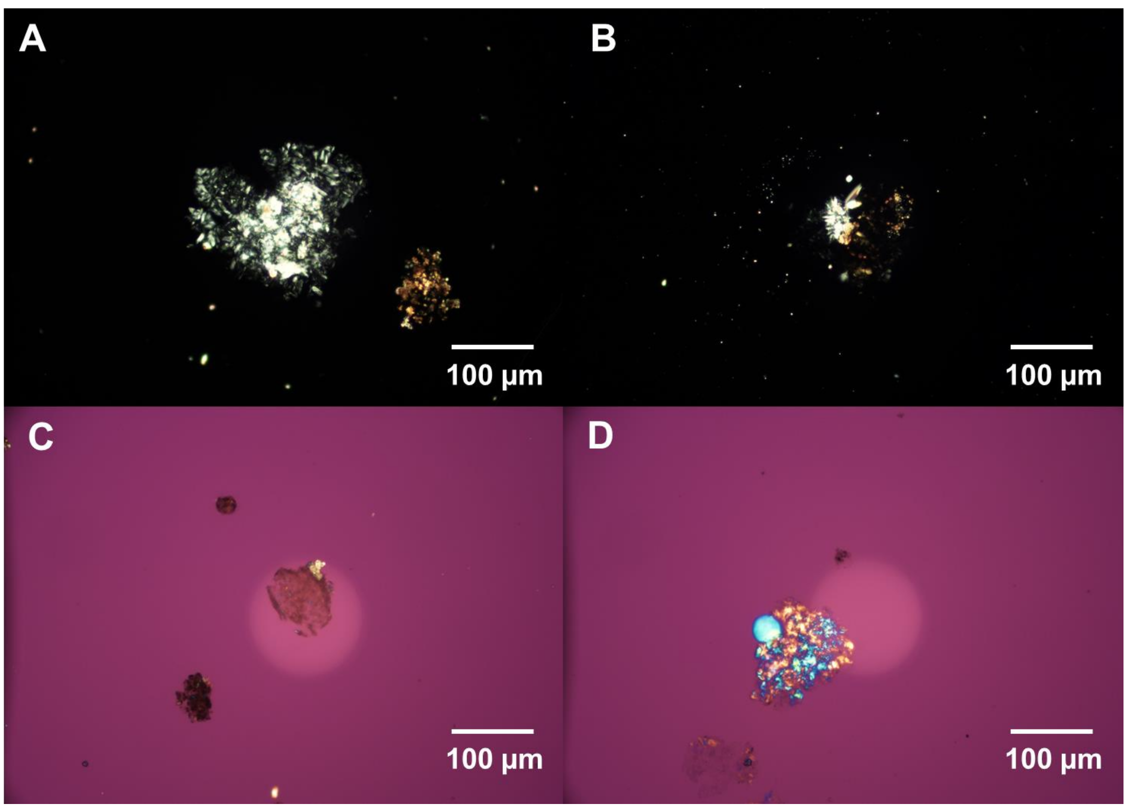

Figure 4.22 PLM images of AN-101-21417 showing minuscule crystal agglomerates (A and B) Cross-Polar images, and (C and D) Cross-polar with ¼ waveplate showing (C) low and (D) high in the particles.

The contrast variation in the ¼ waveplate image was caused by lighting issues that were not removed. Under cross-polars, high contrast can be seen and under the ¼ wavelength compensator, the characteristic low birefringence of natrophosphate in the large particle in Figure 4.22C. can be seen. The particle size distributions for the major phases are shown in Figure 4.23

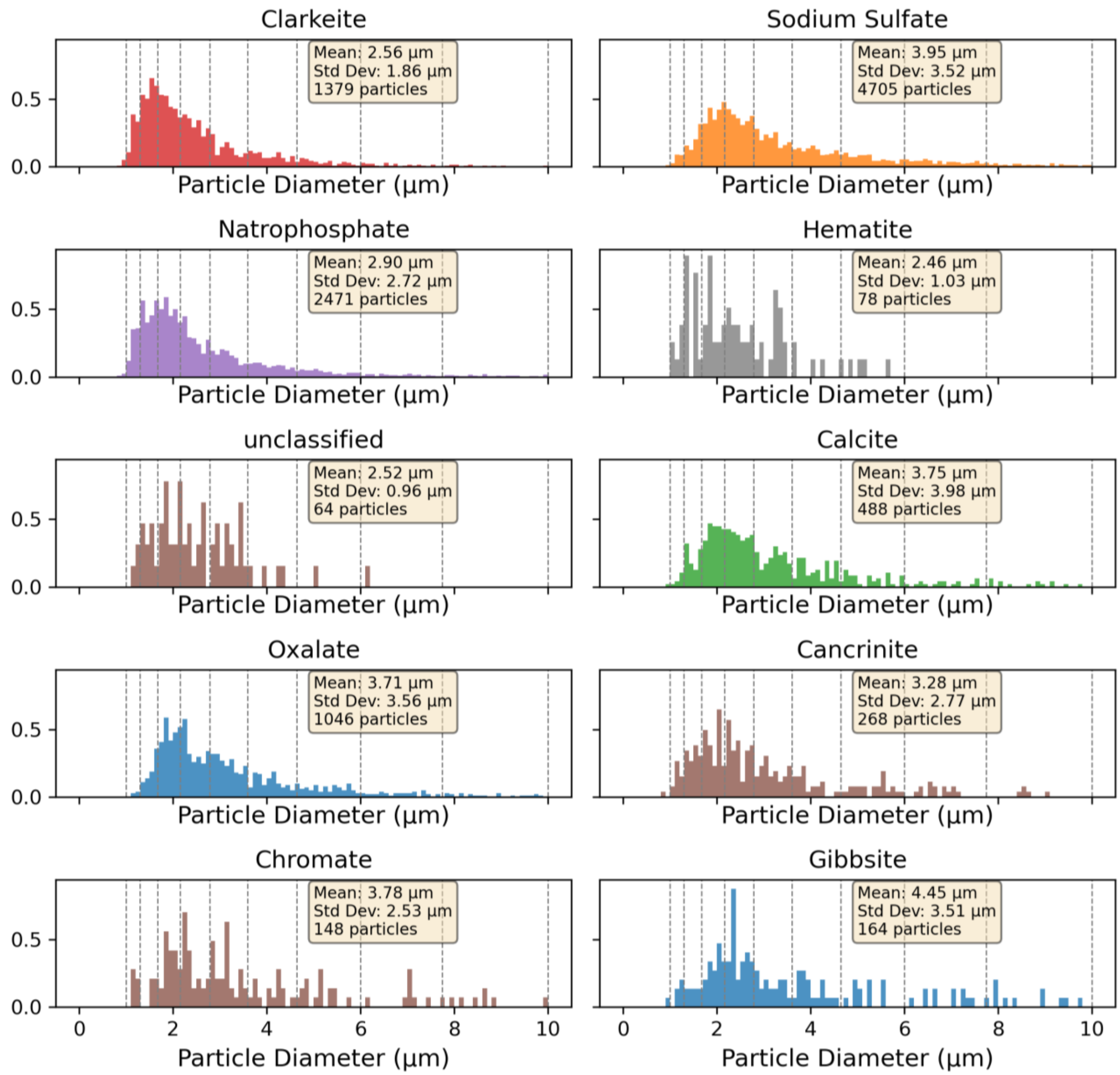

Figure 4.23 Normalized distribution of particle sizes for specific phase categories including mean and standard deviation values for AN-101-19LH.

4.4 Conclusion to AN-101 APA

The APA method is effective at analyzing thousands of particles and reporting compositions and morphologies. However, some particles are not easily analyzed and may be under-reported. This results from problems with sample preparation that can bias the sample collection. Large particles can crash out of the SEM preparation and become difficult to count or segment. The phases observed in AN-101 included phosphates (natrophosphates), sulfates (possibly kogarkoite), and gibbsite.

Table 4.1 List of AN-101 segments with major particles including average diameter and number of particles analyzed in brackets.

Segment Identification	Gibbsite	Clarkeite	Fe/Zr-oxide
	Equivalent circular diameter (µm) and the total number of particles counted		
14UH	3.67 ± 3.24 µm (10776)	2.70 ± 1.79 µm (9029)	3.03 ± 1.86 µm (1347)
18LH	3.80 ± 2.46 µm (27648)	--	1.86 ± 1.78 µm (441)
19LH*	4.45 ± 3.51 µm (164)	2.56 ± 1.86 µm (1379)	2.46 ± 1.03 µm (78)

*This sample contained an unusual amount of a sodium sulfate phase.

5.0 AW-105 Solids

5.1 AW-105-20326 (8LH) and 19262 (8UH)

SEM stub prepared from the AW-105 Solids sample was dominated by zirconium phases and NaF, possibly villiaumite. The NaF particles were tenaciously attached to the larger Zr-particles. There were also a few uranium particles in these specimens. Figure 5.1 shows a series of images at increasing magnification showing highly heterogeneous particle agglomerates. Under BSE imaging, the high Z particles show up clearly and these were identified as Zr- (see Figure 5.3), iron-bearing, and U- particles (see Figure 5.4) mainly. However, one of the most common phases in AW-105, NaF (villiaumite) could not be distinguished with BSE contrast and was only observed in the elemental maps (see Figure 5.5). This meant that APA using BSE contrast could not pick up this specific phase. Reynolds and coworkers have previous identified both villiaumite (NaF) and Zr-oxides in 241AW-105 wastes (Reynolds et al., 2014).

The particles from the AW-105 that were mainly Zr-bearing, were large, well over 100 µm in diameter, and might not be expected to be present in a supernatant.

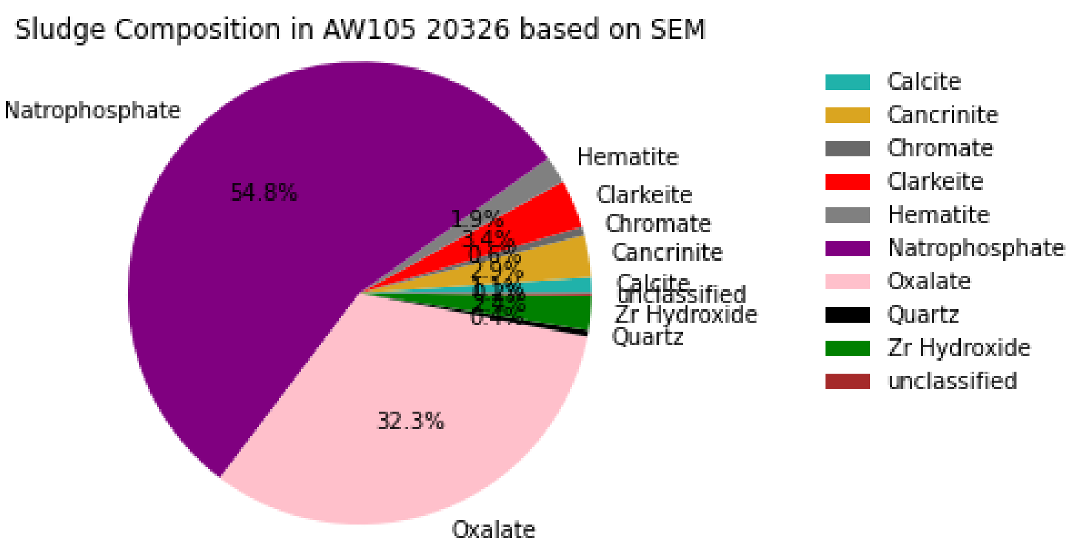

Figure 5.1 Phase distribution of AW-105-20326 solids sample.

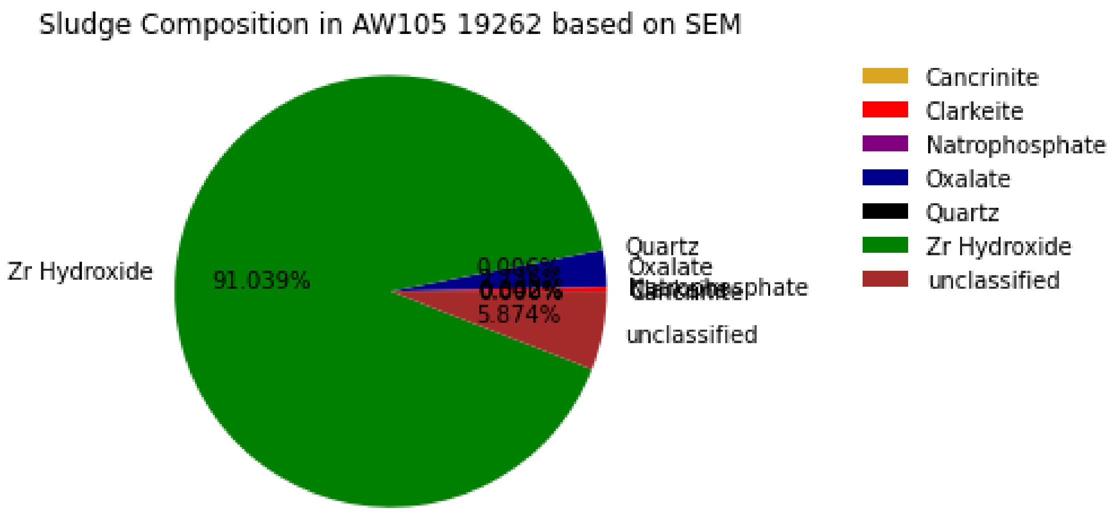

Figure 5.2 Phase distribution of AW-105-19262 solids sample.

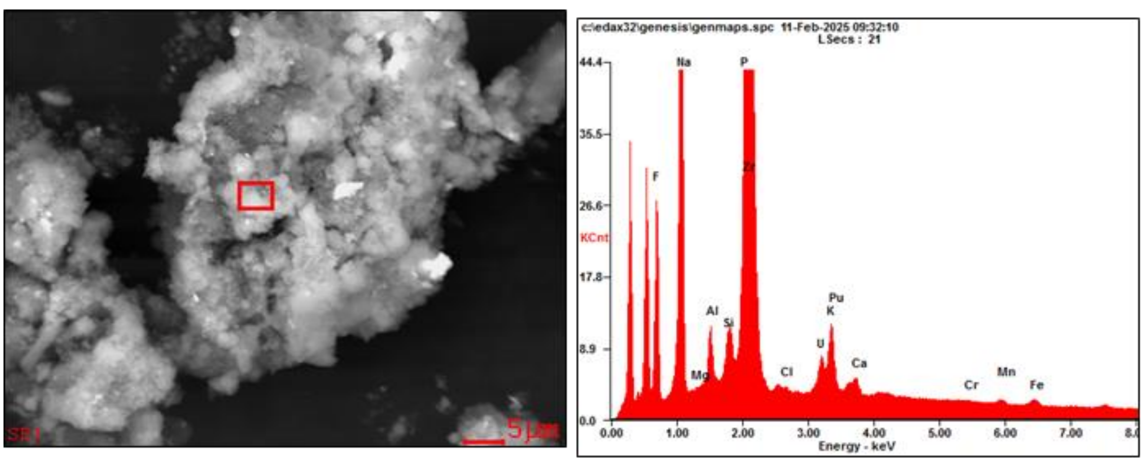

Figure 5.3 SEM image and EDS of Zr-bearing phase with a composition similar to that observed by Reynolds and coworkers

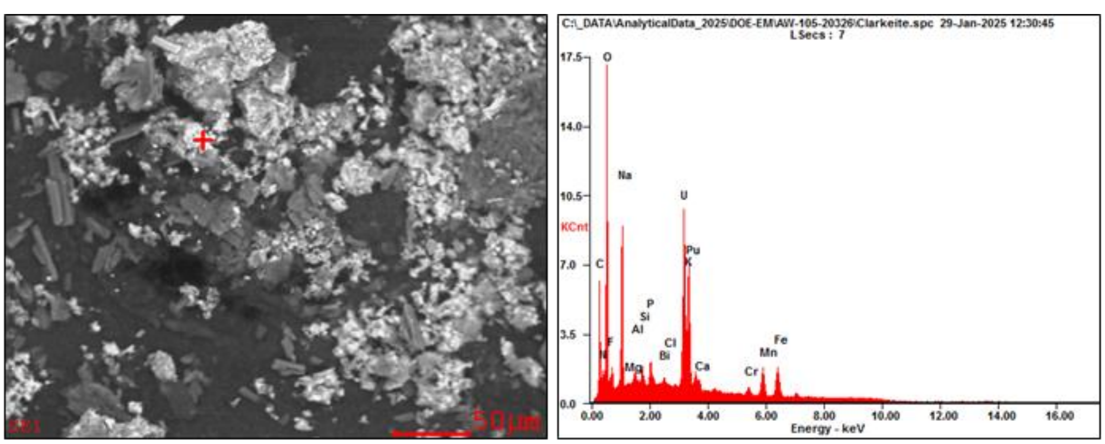

Figure 5.4 SEM images of various particles and an identified uranium-bearing phase consistent with clarkeite in the AW-105-20326 Solids sample.

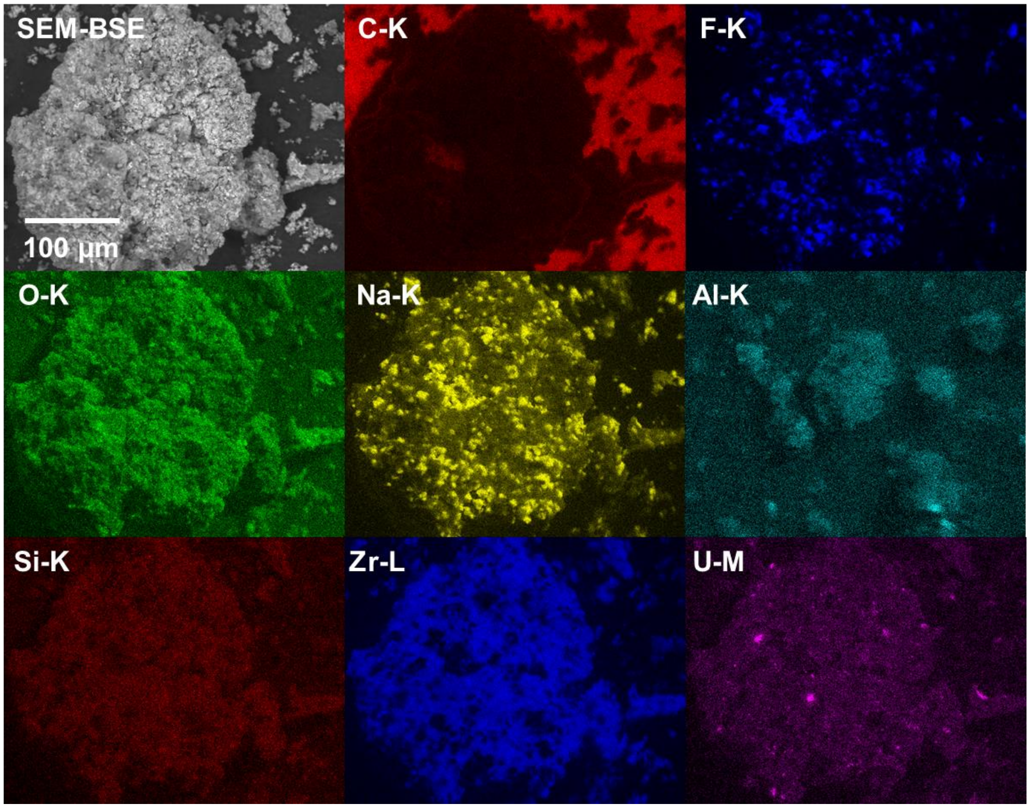

Figure 5.5 SEM Image and EDS maps of particle agglomerates found in the AW-105-19262 solids sample showing NaF (villiaumite) particles and zirconium phases.

The distribution elements shown in Figure 5.5 was commonly found throughout the sample. Another elemental map example shown in Figure 5.6, shows the similar occurrence of Zr- and U-bearing particles, and NaF in the AW-105 sludge sample (Note F is not show in the map in this case). Another common phase was found to consist mainly of Mn and Fe. Carbon was present in the support film making it difficult to locate C-bearing phases. The relationships between the compositions and phases were also examined with APA. In the ternary diagram (see Figure 5.7A), by plotting both Na and F, a Na-F composition was shown to be present. The ternary plot in Figure 5.7B also shows that U- and Zr- phases predominate in the specimen. APA was also used to describe the major phases in the sludge. The Zr-rich phase remains unidentified but was, for the purposes of describing the particle densities, defined as Zr-hydroxide. This phase was the largest single contributor to this AW-105 segment (see Figure 5.8).

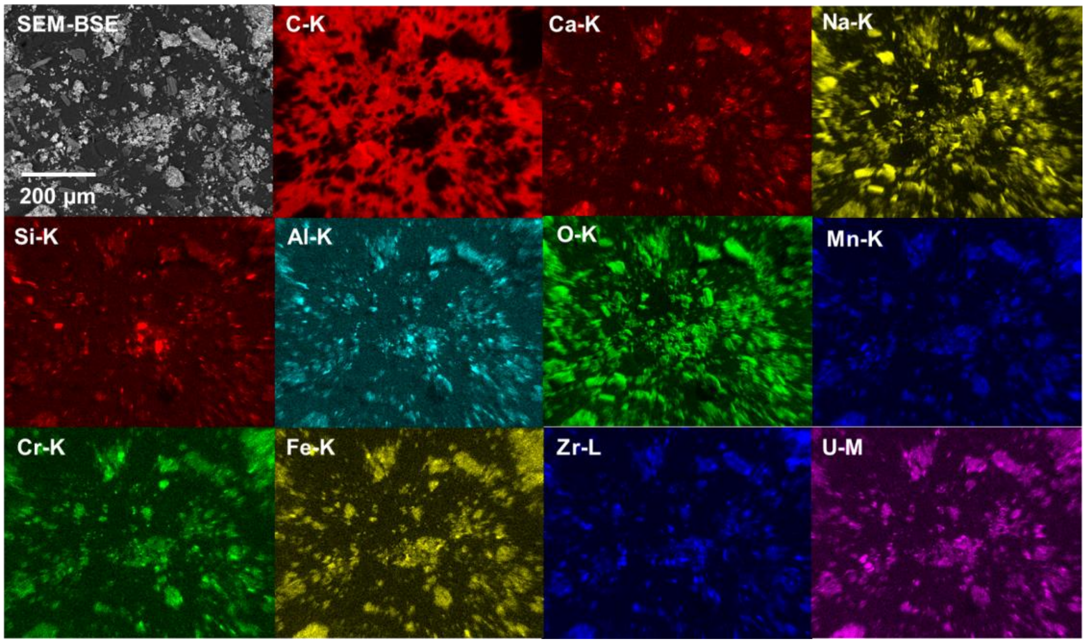

Figure 5.6 SEM image and EDS elemental maps from solids sample AW-105-20326 showing the occurrence of Mn-Fe particles, Fe-Cr, and U-bearing phases.

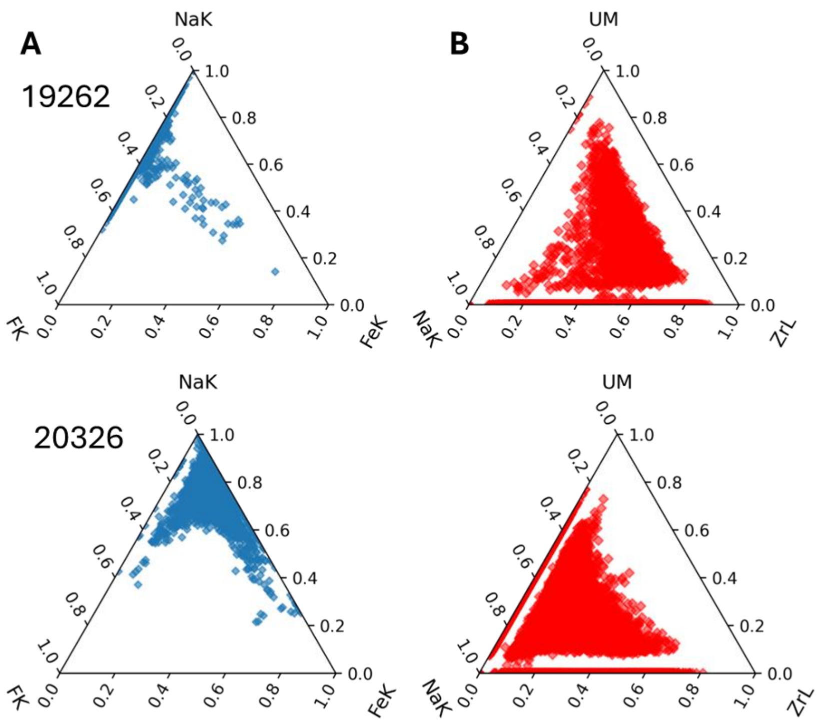

Figure 5.7 The ternary plots suggest the occurrence of a (A) NaF phase and (B) significant amount of Zr- and U-phases. (Top row AW-105 19262 and bottom row AW-105-20326)

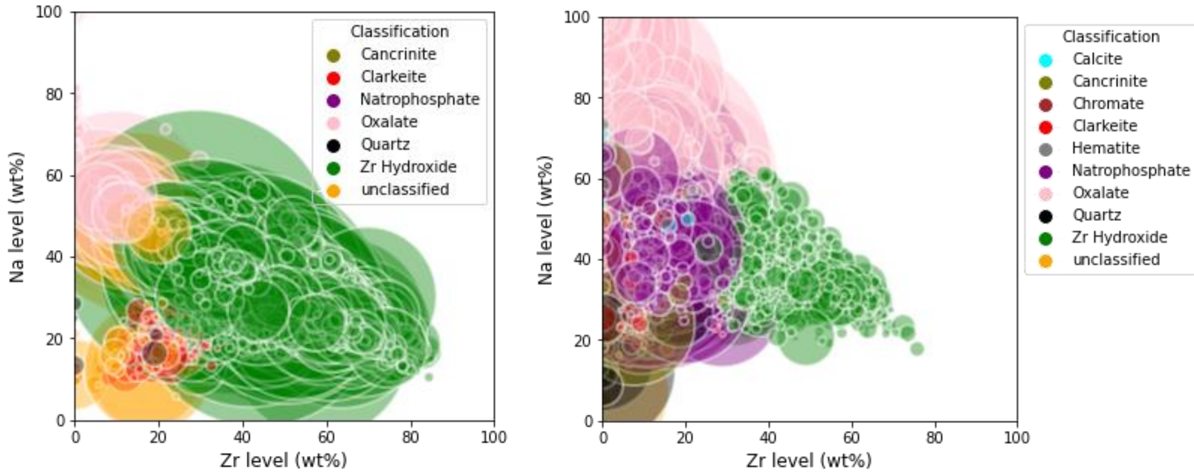

Figure 5.8 Most of the AW-105 sample segments contained Zr-bearing particles. (A) 19262 and (B) 20326.

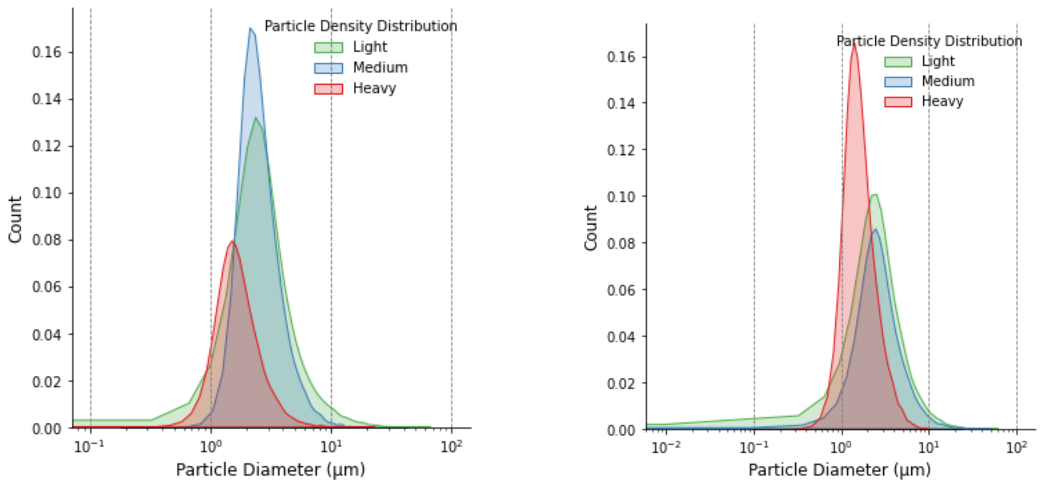

Figure 5.9 The major components based on BSE contrast from the AW-105 sample segments (A) 19262 and (B) 20326, both showing log-normal distributions.

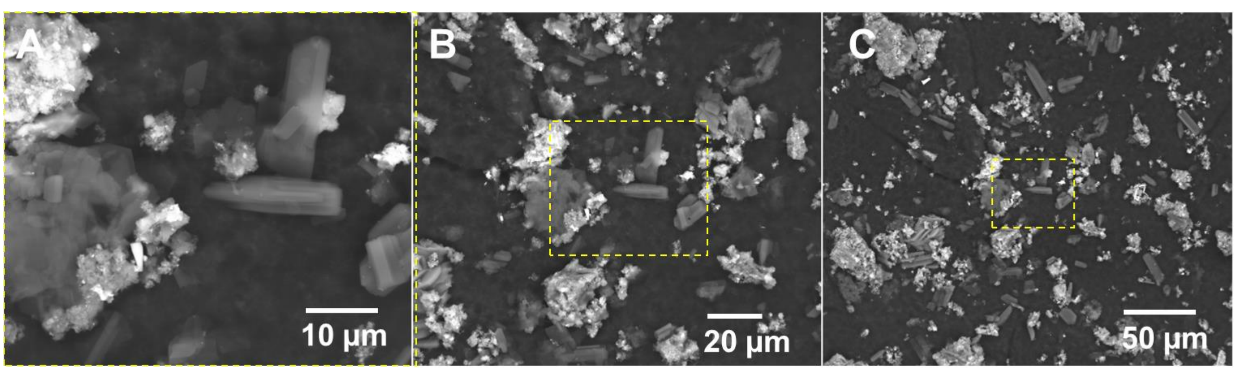

Figure 5.10 SEM images of AW-105-20326 showing elongated phosphate particles

The PLM images were collected with cross-polars and with the ¼ waveplate compensator (see Figure 5.11) The particles were immersed in collodion which has a refractive index of 1.51.

Natrophosphate is known to exhibit low birefringence (i.e., the phase would exhibit almost the same contrast as the background) whereas sodium phosphate has high birefringence. Distinguishing these two phases with SEM-EDS is difficult. There is only a small amount of fluorine in natrophosphate, and the F-K x-ray line is strongly absorbed by oxygen making its visibility above background in this low energy range of the spectrum poor. In this case, most of fluorine was associated with sodium as NaF. NaF presented another problem during SEM-APA imaging because the backscattered contrast varied little between the NaF and the other major phases.

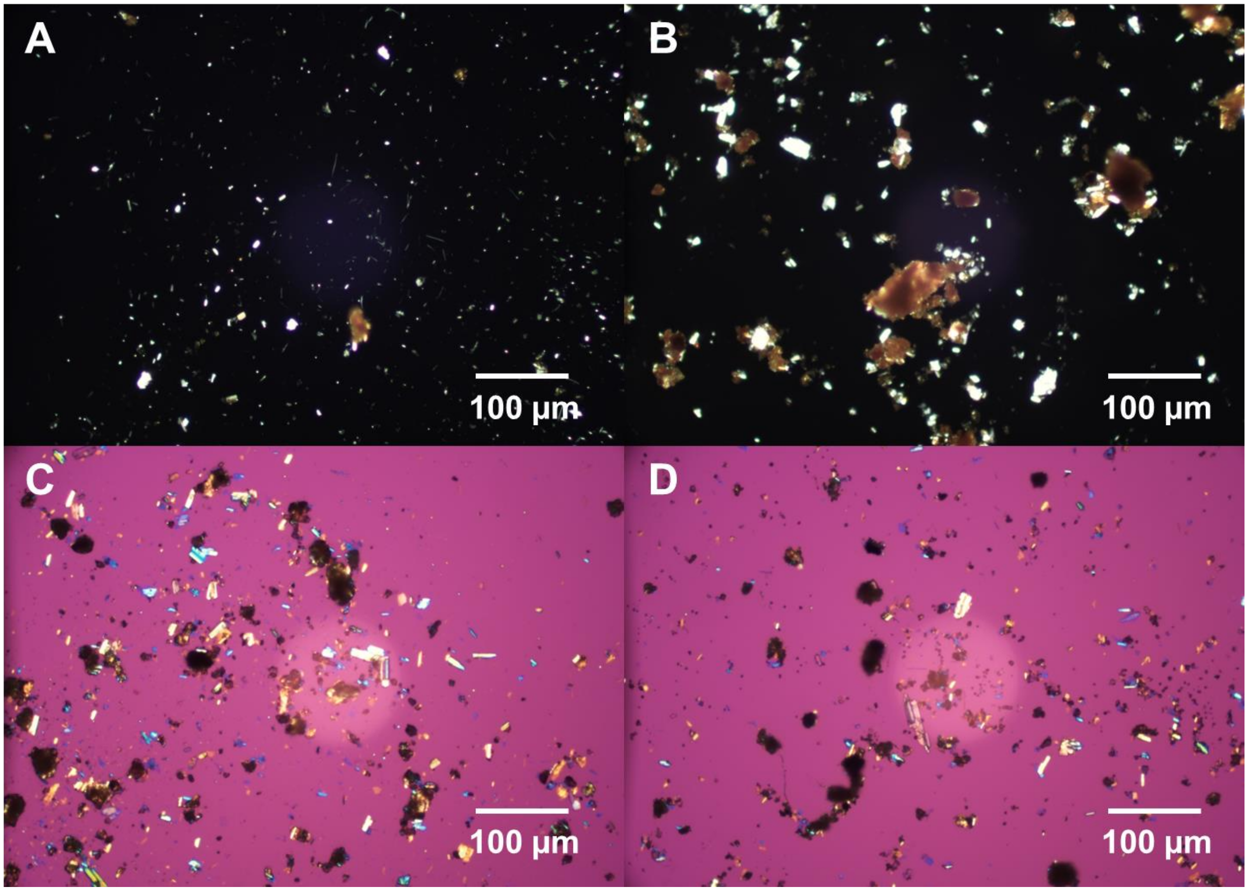

Figure 5.11 PLM images of AW-105-20326 showing elongated crystals consistent with a sodium phosphate (A and B) Cross-Polar images, and (C and D) Cross-polar with ¼ waveplate showing high birefringence in the elongated phosphate particles.

The particle size distributions for the major phases observed with APA are shown in Figure 5.12 and Figure 5.13.

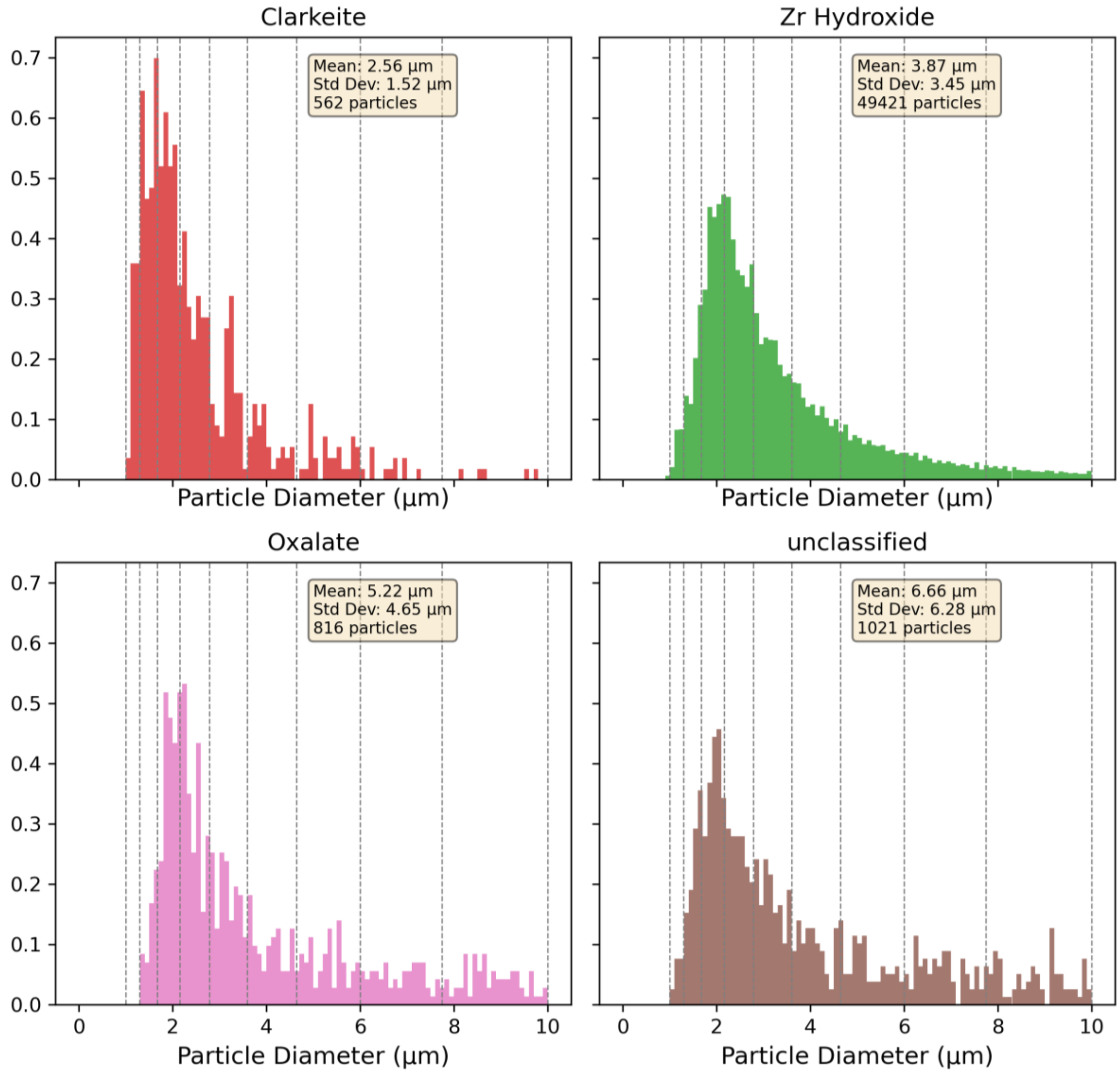

Figure 5.12 Particle size distributions from major phases in AW-105-19262 (8UH)

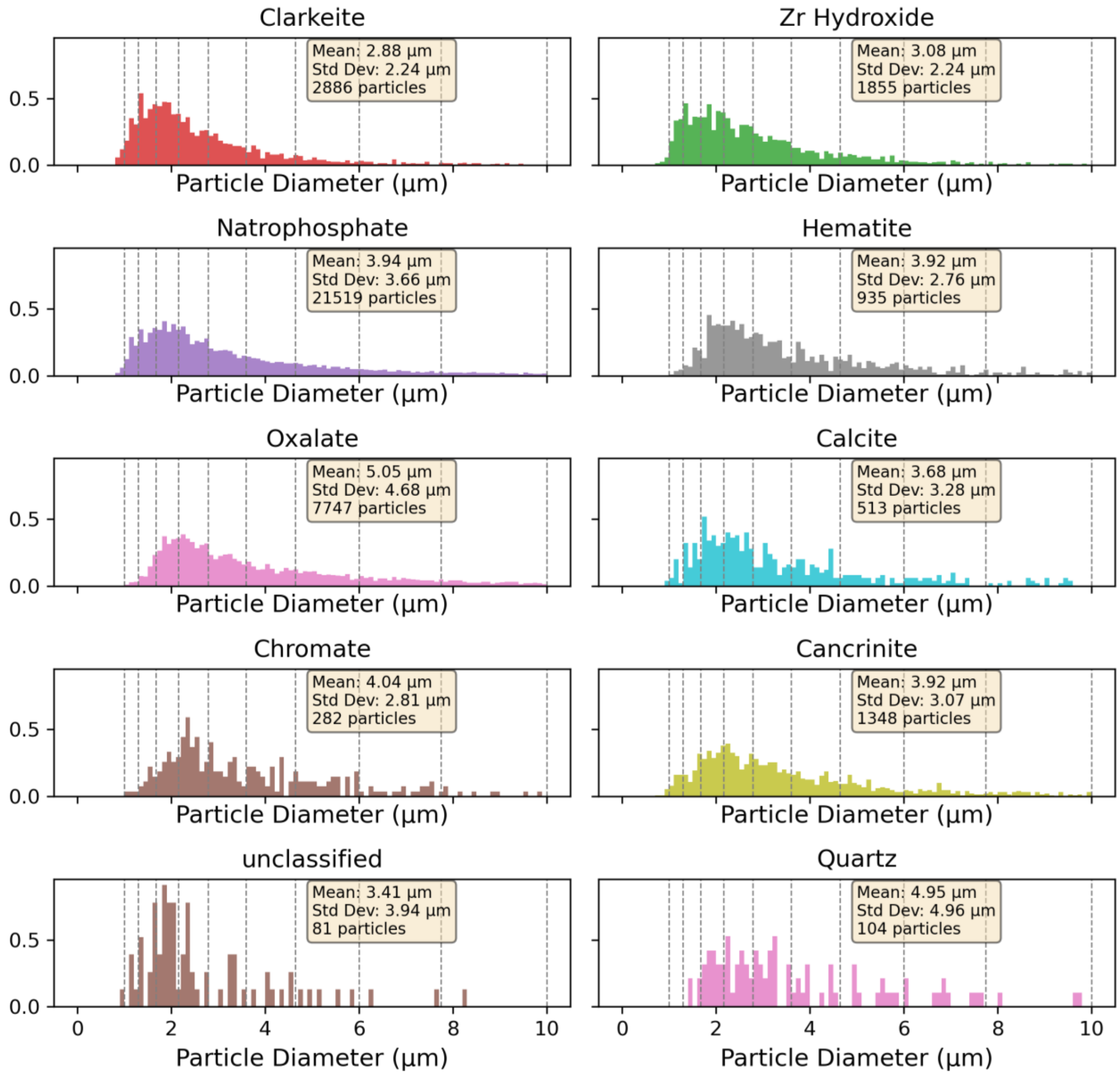

Figure 5.13 Particle Size Distributions from AW-105-20326 (8LH)

5.2 Conclusion to AW-105 APA

Sodium phosphate and Zr-hydroxide were the major phases in the AW-105 series. Through elemental mapping, it was also clear that NaF (possibly villiaumite) was present, but this phase could not be identified with APA. There was no variation in contrast between villiaumite and the larger particles that this phase was attached. The PLM work also suggest the occurrence of a sodium phosphate and not the fluorine containing natrophosphate. The elongated articles exhibited the high birefringence normally associated with sodium phosphate not natrophosphate. The fluorine appeared to be associated with sodium in a villiaumite type phase instead.

Table 5.1 List of AW-105 segments with major particles including average diameter and number of particles analyzed in brackets.

Segment Identification	Gibbsite	Clarkeite	Zr-oxide
		Equivalent circular diameter (µm) and the total number of particles counted	
8LH	--	2.88 ± 2.24 µm (2886)	3.08 ± 2.24 µm (1855)
8UH	--	2.56 ± 1.52 µm (562)	3.87 ± 3.45 µm (49421)

6.0 Conclusions

APA has enabled more particles of Hanford tank wastes than has been done previously. However, sampling remains an issue because large variations in particle sizes. APA enabled direct determination of PSDD. It is notable that the particles are small; however, the particles were most often present as heterogeneous agglomerates, so questions remain on what defines a particle. Unlike light scattering techniques or small angle x-ray scattering for particle size determination, SEM-APA provides both the particle dimensions and the particle composition. This enables the particle density to be determined.

In Phase two, we will look at mixtures of wastes and washed wastes. This should lead to more accurate sampling that in turn will provide improved PSDDs as the soluble phases that were causing problems during this study will be dissolved. Such PSDD information should translate to improvements in mixing and transport. For potential deleterious effects on waste processing, a relatively small number of particles need to have particle dimensions in the 10 µm in diameter size range. The log-normal PSDD will allow determination of the likelihood of a specific particle exceeding this value. A further limitation is the handling of Hanford tank waste samples owing to the radioactivity of the samples and its potential impact on the EDS detector. To date, samples containing close to a maximum activity of 100,000 to 400,000 dpm were analyzed with no issues to the instrumentation. Damage to the detector can be identified through decreasing energy resolution and loss of detector performance at different time constants.

During this study, the analysis methodology improved, with better dispersed samples as well as performing analysis on a larger number of SEM stubs. Improvements were also made to the image segmentation so that more features could be extracted during an analysis. However, there remain issues with rapid deposition of particles leading to regions with high densities of particles that are inappropriate for APA but may contain the larger particles that are possibly more important to measure. By combining PLM analyses, we can cover the larger particles and use transmission electron microscopy to uniquely identify the phases and compositions when needed.

Future efforts will work with washed solids and mixtures of the materials used in this study that will enable a better focus on the solids that will matter during transport of these solids during waste processing. The easily dissolved phases, such as phosphates, should be removed during the washing.

7.0 References

Allred, J. R., Buck, E. C., Daniel, R. C., Geeting, J. G. H., Westesen, A. M., & Peterson, R. A. (2024). Automated SEM analysis of particles in Hanford tank waste. *Journal of Hazardous Materials*, 134412. https://doi.org/https://doi.org/10.1016/j.jhazmat.2024.134412

Alxneit, I. (2020). Particle Size Distributions from Electron Microscopy Images: Avoiding Pitfalls. *The Journal of Physical Chemistry A*, *124*(48), 10075-10081. https://doi.org/10.1021/acs.jpca.0c07840

Bolling, S. D., Reynolds, J. G., Ely, T. M., Lachut, J. S., Lamothe, M. E., & Cooke, G. A. (2019). Natrophosphate and kogarkoite precipitated from alkaline nuclear waste at Hanford. *Journal of Radioanalytical and Nuclear Chemistry*. https://doi.org/10.1007/s10967-019-06924-9

Buck, E. C., & McNamara, B. K. (2004). Precipitation of nitrate-cancrinite in Hanford tank sludge. *Environmental science & technology*, *38*(16), 4432-4438.

Cantrell, K. J., Krupka, K. M., Deutsch, W. J., & Lindberg, M. J. (2006). Residual Waste from Hanford Tanks 241-C-203 and 241-C-204. 2. Contaminant Release Model. *Environmental science & technology*, *40*(12), 3755-3761. https://doi.org/10.1021/es0511568

Colburn, H. A., & Peterson, R. A. (2021). A history of Hanford tank waste, implications for waste treatment, and disposal. *Environmental Progress & Sustainable Energy*, *40*(1), e13567. https://doi.org/https://doi.org/10.1002/ep.13567

Deutsch, W. J., Cantrell, K. J., Krupka, K. M., Lindberg, M. L., & Jeffery Serne, R. (2011). Hanford tank residual waste – Contaminant source terms and release models. *Applied Geochemistry*, *26*(9–10), 1681-1693. https://doi.org/http://dx.doi.org/10.1016/j.apgeochem.2011.04.025

DiCenso, A. T., Amato, L. C., Franklin, J. D., Lambie, R. W., Stephens, R. H., & Simpson, B. C. (1994). *Tank characterization report for double-shell Tank 241-AW-105*. https://www.osti.gov/biblio/10189061
https://www.osti.gov/servlets/purl/10189061

Dodd, R. A. (2008). *TANK FARM RETRIEVAL LESSONS LEARNED AT THE HANFORD SITE* Conference: WM08 CONFERENCE WASTE MANAGEMENT SYMPOSIA INC 02/24/2008 THRU 02/28/2008 PHOENIX AZ, United States. https://www.osti.gov/biblio/922697
https://www.osti.gov/servlets/purl/922697

Douglas, J. G., Westinghouse Hanford. (1996). *Tank characterization report for double-shell tank 241-AN-106*. https://www.osti.gov/biblio/325809
https://www.osti.gov/servlets/purl/325809

Finch, R. J., & Ewing, R. C. (1997). Clarkeite; new chemical and structural data. *American Mineralogist*, *82*(5-6), 607-619. https://doi.org/10.2138/am-1997-5-620

Gephart, R. E. (2003). *Hanford: A Conversation about Nuclear Waste and Cleanup*. Battelle Press. https://books.google.com/books?id=syFSAAAAMAAJ

Gephart, R. E. (2003). *A Short History of Hanford Waste Generation, Storage, and Release*. https://www.osti.gov/biblio/897388
https://www.osti.gov/servlets/purl/897388

Herting, D. L., Cooke, G. A., Page, J. S., & Valerio, J. L. (2015). *Hanford Tank Waste Particle Atlas*. https://www.osti.gov/biblio/1423895
https://www.osti.gov/servlets/purl/1423895

Herting, D. L., & Reynolds, J. G. (2016). The composition of natrophosphate (sodium fluoride phosphate hydrate). *Environmental Chemistry Letters*, *14*(3), 401-405. https://doi.org/10.1007/s10311-016-0574-2

Kraft, D. P., & Meznarich, H. K. (2017). *Investigation of Tank 241-AN-101 Floating Solids*. https://www.osti.gov/biblio/1407697
https://www.osti.gov/servlets/purl/1407697

Krupka, K. M., Schaef, H. T., Arey, B. W., Heald, S. M., Deutsch, W. J., Lindberg, M. J., & Cantrell, K. J. (2006). Residual Waste from Hanford Tanks 241-C-203 and 241-C-204. 1. Solids Characterization. *Environmental science & technology*, *40*(12), 3749-3754. https://doi.org/10.1021/es051155f

Lumetta, G. J. (1994). *Pretreatment of neutralized cladding removal waste sludge: Results of the second design basis experiment*. https://www.osti.gov/biblio/10154658
https://www.osti.gov/servlets/purl/10154658

McDonald, L. W., Sentz, K., Hagen, A., Chung, B. W., Nizinski, C. A., Schwerdt, I. J., Hanson, A., Donald, S., Clark, R., Sjoden, G., Porter, R., Athon, M. T., Tasdizen, T., Noel, V., Webb, S. M., Van Veelen, A., Hickam, S. M., & Ly, C. (2024). Review of multi-faceted morphologic signatures of actinide process materials for nuclear forensic science. *Journal of Nuclear Materials*, *588*, 154779. https://doi.org/https://doi.org/10.1016/j.jnucmat.2023.154779

Olsen, A. M., Richards, B., Schwerdt, I., Heffernan, S., Lusk, R., Smith, B., Jurrus, E., Ruggiero, C., & McDonald, L. W. I. V. (2017). Quantifying Morphological Features of α-U3O8 with Image Analysis for Nuclear Forensics. *Analytical Chemistry*, *89*(5), 3177-3183. https://doi.org/10.1021/acs.analchem.6b05020

Peterson, R. A., Buck, E. C., Chun, J., Daniel, R. C., Herting, D. L., Ilton, E. S., Lumetta, G. J., & Clark, S. B. (2018). Review of the Scientific Understanding of Radioactive Waste at the U.S. DOE Hanford Site. *Environmental science & technology*, *52*(2), 381-396. https://doi.org/10.1021/acs.est.7b04077

Poloski, A. P., Bonebrake, M. L., Casella, A. M., Johnson, M. D., Toth, J. J., Adkins, H. E., Chun, J., Denslow, K. M., Luna, M., & Tingey, J. M. (2009). *Deposition Velocities of Non-Newtonian Slurries in Pipelines: Complex Simulant Testing*. https://www.osti.gov/biblio/992020
https://www.osti.gov/servlets/purl/992020

Reynolds, J. G., Cooke, G. A., & Herting, D. L. (2020). Sodium strontium phosphate nonahydrate (NaSrPO4·9H2O) found in Hanford nuclear waste. *Journal of Radioanalytical and Nuclear Chemistry*, *326*(1), 435-443. https://doi.org/10.1007/s10967-020-07296-1

Reynolds, J. G., Huber, H. J., Cooke, G. A., & Pestovich, J. A. (2014). Solid-phase zirconium and fluoride species in alkaline zircaloy cladding waste at Hanford. *Journal of Hazardous Materials*, *278*, 203-210. https://doi.org/http://dx.doi.org/10.1016/j.jhazmat.2014.05.097

Sasaki, L. M. (1997). *Tank characterization report for double-shell tank 241-AW-105*. https://www.osti.gov/biblio/328504
https://www.osti.gov/servlets/purl/328504

Schwerdt, I. J., Brenkmann, A., Martinson, S., Albrecht, B. D., Heffernan, S., Klosterman, M. R., Kirkham, T., Tasdizen, T., & McDonald Iv, L. W. (2018). Nuclear proliferomics: A new field of study to identify signatures of nuclear materials as demonstrated on alpha-UO3. *Talanta*, *186*, 433-444. https://doi.org/https://doi.org/10.1016/j.talanta.2018.04.092

Wells, B., Knight, M., Buck, E., Daniel, R., Cooley, S., Mahoney, L., Meyer, P., Poloski, A., Tingey, J., & Callaway, W. (2007). Estimate of Hanford Waste Insoluble Solid Particle Size and Density Distribution. *Battelle—Pacific Northwest Division, Paper No. PNWD-3824*.

Wells, B. E., Kurath, D. E., Mahoney, L. A., Onishi, Y., Huckaby, J. L., Cooley, S. K., Burns, C. A., Buck, E. C., Tingey, J. M., Daniel, R. C., & Anderson, K. K. (2011). *Hanford Waste Physical and Rheological Properties: Data and Gaps*. https://www.osti.gov/biblio/1025093
https://www.osti.gov/servlets/purl/1025093

Westesen, A. M., Murray, K. J., Bachman, A. A., Burns, C. A. M., Scott, T. S., Rigby, J. C., & Peterson, R. A. (2023). *Evaluation of High Level Waste Sludge Processing Behavior*. https://www.osti.gov/biblio/2478876
https://www.osti.gov/servlets/purl/2478876

8.0 Appendix

A.1 Instruments used

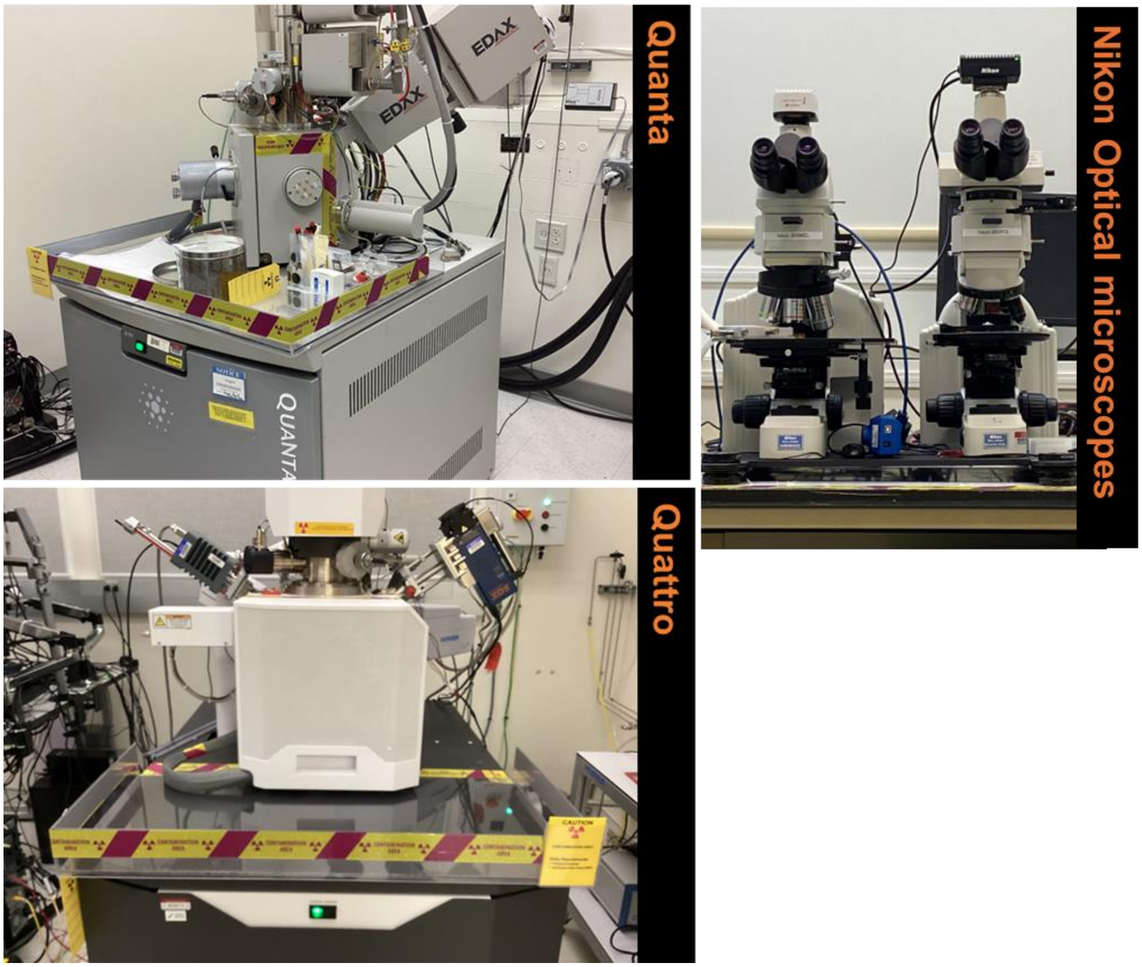

Figure A1.8.1 Photos of the two SEM instruments and the Nikon optical microscopes used in this study that are in the RPL at PNNL

The APA was performed exclusively on the FEI Quanta 250FEG (Thermo-Fisher, Inc., Hillsboro, OR) equipped with EDAX EDS detector (Ametek, Inc., Mahwah, NJ) running Genesis analysis software and APA package. Both SEMs and optical systems were available for work with radioactive materials and operated as contamination areas.

A.2 Magnification calibration

A.2.1 Scanning Electron microscopes

The calibration of the Scanning Electron Microscopes was checked with the MRS-4 standard following procedures described in Lab Assist Activity #4493 v2, Scanning Electron Microscopy of Radioactive Materials, Section 3.0- Quality Assurance.

A.2.1.1 Thermo-Fisher Quattro S

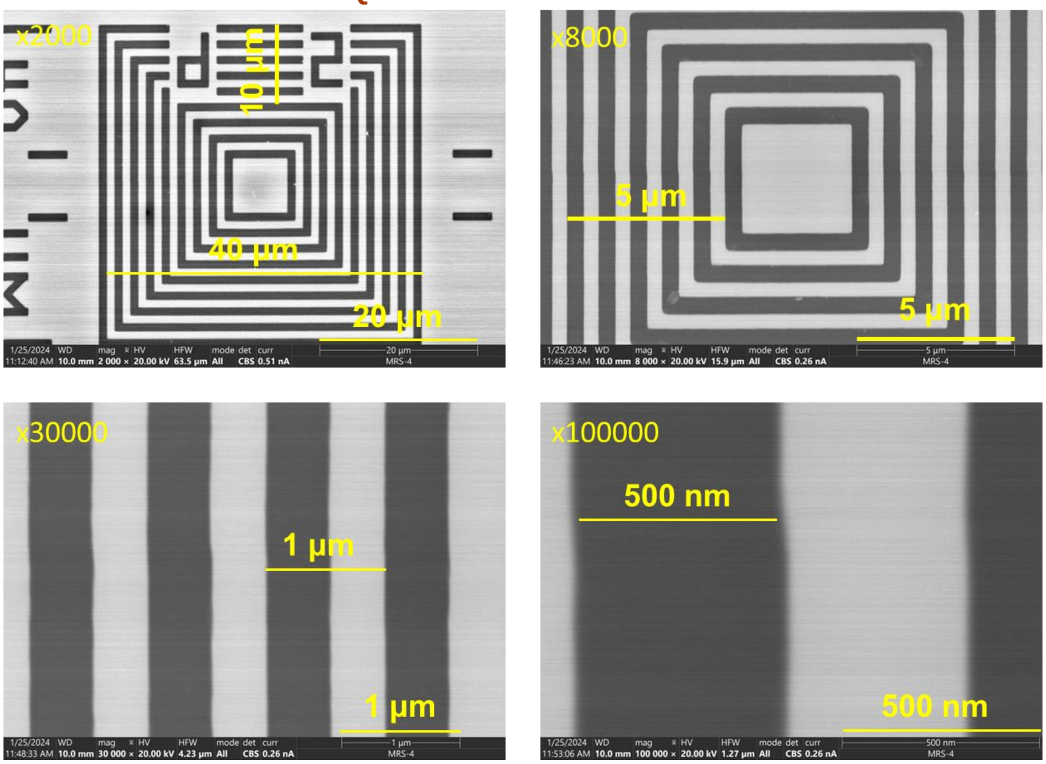

Figure A1.8.2 The magnification bar match to the actual magnification is < 1% error. For objects smaller than 1 µm, the error increases

A.2.1.2 Magnification Calibration – FEI Quanta 250FEG

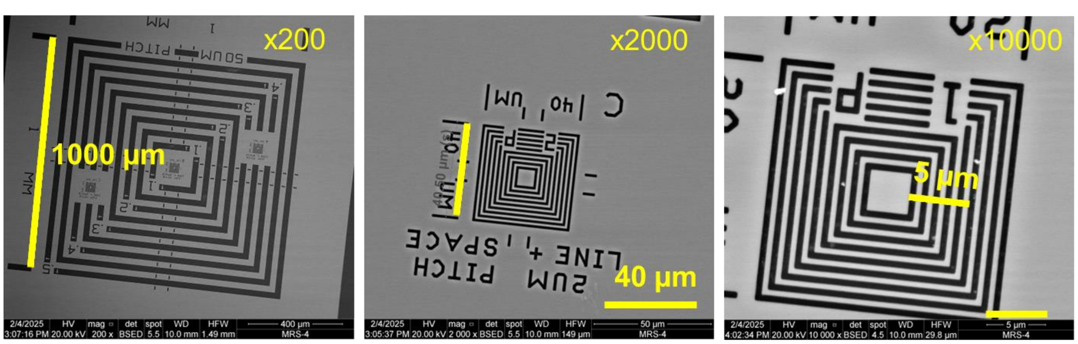

Figure A1.8.3 The magnification bar match to MRS-4 standard. Between 200x and 10000x, the error in the magnification scale were <1%.

A.2.2 Magnification Calibration – Nikon 400POL

The Nikon microscopes were calibrated with a NIST-2800 magnification standard following Lab Assist Activity #4490 v2, Optical Microscopy with Radioactive Materials, Section 8.0-Quality Assurance.

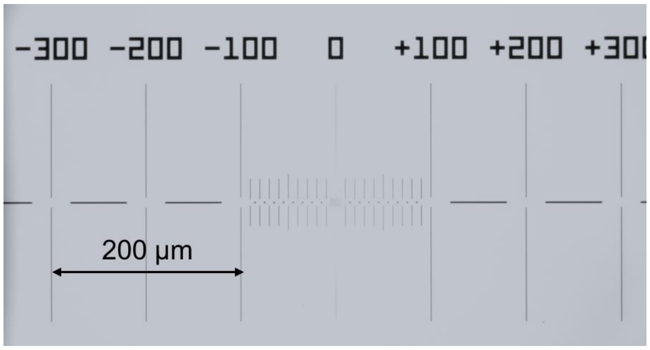

Figure A1.8.4 The magnification scale from NIST-2800 standard. This was used to calibrate the 20x objective used in this study.

A.2.3 EDS Detector optimum conditions

Effect of Probe Current on Count Rate

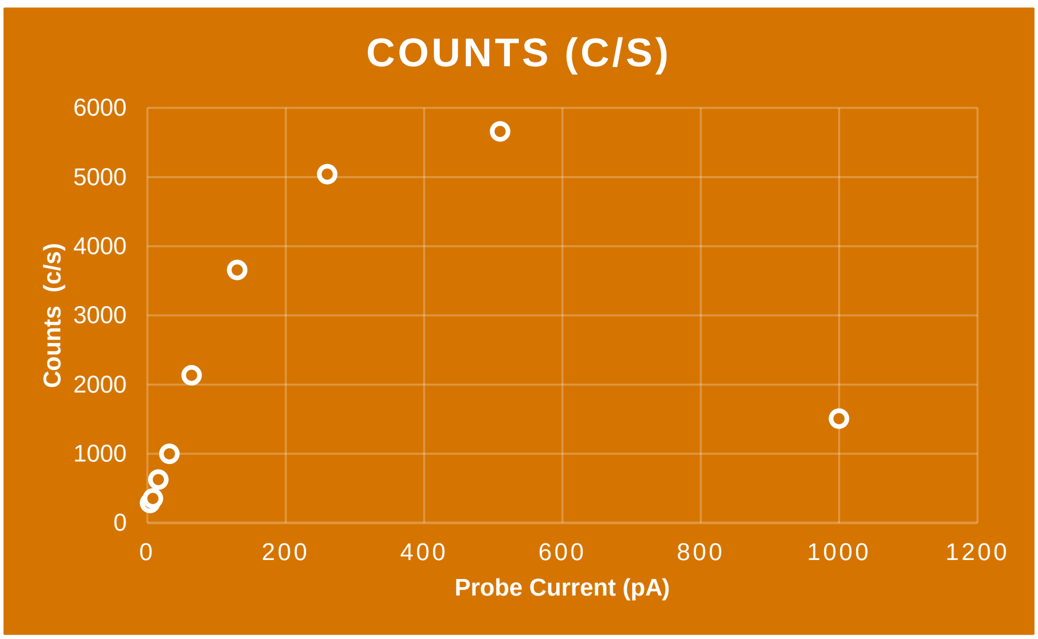

Figure A1.8.5 20 keV Fe-K-alpha (100 sec at 1000x, with TC=4.0)

Effect of Working Distance on EDS Counts

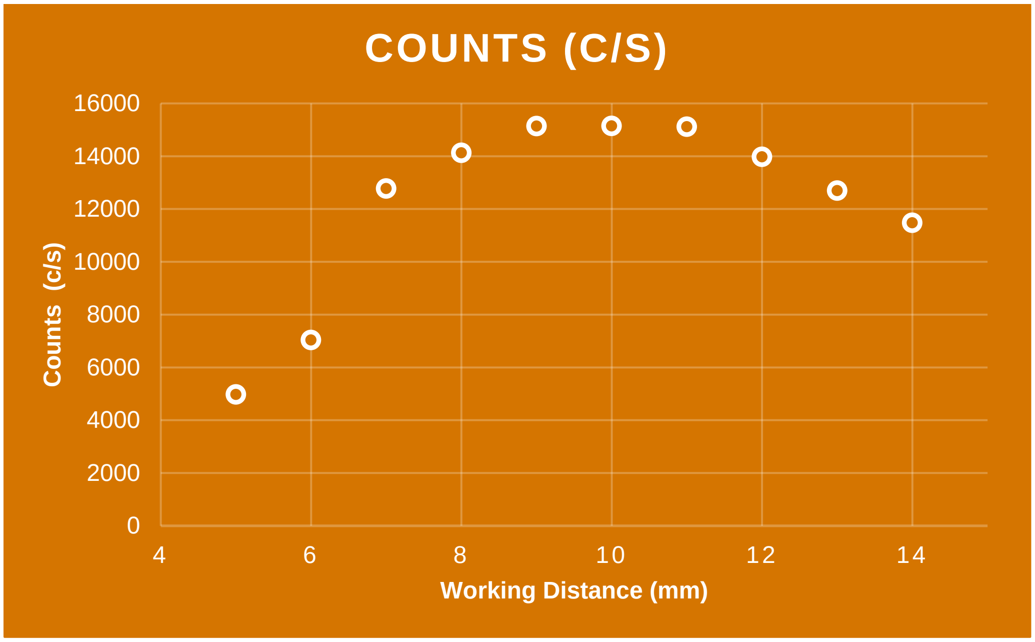

Figure A1.8.6 25 keV 0.28 nA, x1000, DBS Retracted

The counts at the detector are relatively constant between 9 and 11 mm working distance.

Table 8.1 FWHM Measurement using the Cr-K line

iXRF Detector	EDAX Detector
Cr-FWHM Measurement	Cu-K-FWHM Measurement
121.76	131.15
118.26	130.77
118.22	130.58
126.76	130.57
129.2	130.80
121.73	131.11
122.46	130.31
123.35	
123.95	
109.92	
Min:109.9	
Max: 129.2	
Mean: 121.6	
STD: 5.3 eV	
Using Cr K line at 5.419	

Resolution of the detector well within the acceptance of the iXRF detector and EDAX detector

A.3 Python Code used in the analysis of data

A.3.1 Data files

The code reads in multiple common separated values (CSV) files from the microscope- EDS system and combines these into a single dataframe. Some of the names of the phases used initially in the APA analysis were converted into more relevant ones. For instance, when a phase could not connected to a phase, the APA called it 'none.' This was changed to 'unclassified' as shown below.

```
import os
import glob
import pandas as pd
import numpy as np
```

```
extension = 'csv'
all_filenames = [i for i in glob.glob('*.{}'.format(extension))]
```

```
#combine all files in the list
combined_csv = pd.concat([pd.read_csv(f) for f in all_filenames ])
#export to csv
combined_csv.to_csv( "Combined_AN101_21407.csv", index=False, encoding='utf-8-sig')
```

```
df=pd.read_csv('Combined_AN101_21407.csv')
df = df.replace('Zircaloy', 'Zr Hydroxide', regex=True)
df = df.replace('None', 'unclassified', regex=True)
df.head(15)
```

A.3.2 Code for ternary plots.

The code uses geosciences specific python package called pyrolite. This package is designed to produce ternary plots from any of the categories in the dataframe. Three elements were chosen and then plotted on the ternary plot.

```
import pandas as pd
import matplotlib.pyplot as plt
from pyrolite.plot import pyroplot
import seaborn as sns
```

```
fig, ax = plt.subplots(1, 3, sharex=True, sharey=True, figsize=(11, 4))

df.loc[:, ["SiK", "AlK", "ZrL"]].pyroplot.scatter(ax=ax[0], s=10, alpha=0.6, renorm=True)
df.loc[:, ["UM", "FeK", "PK"]].pyroplot.scatter(ax=ax[1], color="green", alpha=0.5)
df.loc[:, ["AvgDiam", "AlK"]].pyroplot.density(ax=ax[2], colorbar=True)


plt.tight_layout()
plt.show()
```

A.3.3 Code used for the particle size distribution plots.

This code produces individual plots for each phase or category and plots these as histograms. Information regarding the average particle size, standard deviation, and the total number of particles in the specific category are also listed.

```
fig, axes = plt.subplots(6, 2, figsize=(8,8), dpi=300, sharex=True, sharey=True)
colors = ['tab:red', 'tab:blue', 'tab:green', 'tab:pink', 'tab:olive','tab:orange', 'tab:cyan', 'tab:brown', 'tab:green', 'tab:pink', 'tab:bl

for i, (ax, Classification) in enumerate(zip(axes.flatten(), df.Classification.unique())):
    x = df.loc[df.Classification==Classification, 'AvgDiam']
    ax.hist(x, alpha=0.8, bins=100, density=True, range=[0,10], stacked=False, label=str(Classification), color=colors[i])
    ax.set_title(Classification)

        # Calculate mean and standard deviation
    mean_x = np.mean(x)
    std_dev_x = np.std(x)
    count = len(x)

    # Adding vertical stripes at regular log intervals
    log_intervals = np.logspace(0, np.log10(10), num=10)
    for xi in log_intervals:
        ax.axvline(x=xi, color='grey', linestyle='--', linewidth=0.7)

    # Display mean and standard deviation on the plot
    props = dict(boxstyle='round', facecolor='wheat', alpha=0.5)
    textstr = '\n'.join((
        f'Mean: {mean_x:.2f} \u03BCm',
        f'Std Dev: {std_dev_x:.2f} \u03BCm',
        f'{count} particles'
    ))
    ax.text(0.5, 0.95, textstr, transform=ax.transAxes, fontsize=8,
            verticalalignment='top', bbox=props)

    ax.set_title(Classification)
    ax.set_xlabel("Particle Diameter (\u03BCm)")

plt.suptitle('Histogram of AN-101 Particle Sizes', y=1, size=11)
#x.set_ylabel("Number of Particles", labelpad=5, weight='bold', size=12)

plt.tight_layout();
```

```
part = df.groupby("Phase")
partVal =part['AvgDiam'].sum()
partVal
```

A.3.4 Code for generating the BSE contrast log-normal plots

The BSE contrast plot divides the APA data up into major density fractions and displays these as a log-normal plot.

```
]:
# Make a separate list for each density or phase contrast
x1 = list(df[df['Phase'] == '1']['AvgDiam'])
x2 = list(df[df['Phase'] == '2']['AvgDiam'])
x3 = list(df[df['Phase'] == '3']['AvgDiam'])

ax=sns.displot(df, x="AvgDiam", hue="Phase", kind="kde", palette="Set1", legend = False, fill=True)
plt.legend(title='Particle Density Distribution', loc='upper right', labels=['Light', 'Medium', 'Heavy'])

# Add vertical marker lines at appropriate intervals (e.g., 0.1, 1, 10, 100 micrometers)
for value in [0.1, 1, 10, 100]:
    plt.axvline(x=value, color='grey', linestyle='--', linewidth=0.8)

plt.ylabel('Count')
plt.xlabel('Particle Diameter (\u03BCm)')
plt.xscale('log')
plt.show(ax)
```

A.3.5 Code for the bubble plots

The bubble plot displays two element concentrations and generates a bubble proportional to the particle size multiplied, in this case, by ten. The color scheme displays each phase or category as a different color.

```
]:
# Libraries
import pandas as pd

# import matplotlib
import matplotlib.pyplot as plt

# And I need to transform my categorical column (continent) in a numerical value group1->1, group2->2...
df['Classification']=pd.Categorical(df['Classification'])
```

```
import matplotlib.pyplot as plt

# Assuming df['Classification'] has categorical values
# Create a mapping from categories to colors
categories = df['Classification'].cat.categories
colors = plt.cm.plasma(df['Classification'].cat.codes / df['Classification'].cat.codes.max())

# Set the figure size
plt.figure(figsize=(5, 5))

# Scatterplot
scatter = plt.scatter(
    x=df['AlK'],
    y=df['NaK'],
    s=df['Area'] * 10,
    c=df['Classification'].cat.codes,
    cmap="plasma",
    alpha=0.4,
    edgecolors="white",
    linewidth=2,
    marker="o"
)

# Add titles (main and on axis)
plt.xlabel("Al level (wt%)")
plt.ylabel("Na level (wt%)")
plt.ylim(0, 100)
plt.xlim(0, 100)

# Create a legend
legend_labels = [plt.Line2D([0], [0], marker='o', color='w', markerfacecolor=plt.cm.plasma(i / len(categories)), markersize=10) for i in rang
plt.legend(legend_labels, categories, title="Classification", loc="best", frameon=True)

# Show plot
plt.show()
```

A.3.6 Code for the pie charts

Provides a pie chart with each category based on the total area of the phase. This chart could be improved by including the likely density of each phase.

```
# Calculate total amount per category
category_totals = df.groupby('Classification')['Area'].sum()

# Create pie chart
plt.pie(category_totals, labels=category_totals.index, radius =1.2, autopct='%1.1f%%')
plt.title('Sludge Composition in AN101 21407 based on SEM')
plt.legend(loc='upper right', bbox_to_anchor=(2, 1))
plt.show()
```

Pacific Northwest National Laboratory

902 Battelle Boulevard
P.O. Box 999
Richland, WA 99354

1-888-375-PNNL (7665)

www.pnnl.gov